The Particle Finite Element Method (PFEM) in thermo-mechanical problems

J.M. Rodriguez [*], J.M. Carbonell [†], J.C. Cante [‡], J. Oliver [§],

Abstract

The aim of this work is to develop a numerical framework for accurately and robustly simulating the different conditions exhibited by thermo-mechanical problems. In particular the work will focus on the analysis of problems involving large strains, rotations, multiple contacts, large boundary surface changes and thermal effects.

The framework of the numerical scheme is based on the Particle Finite Element Method (PFEM) in which the spatial domain is continuously redefined by a distinct nodal reconnection, generated by a *Delaunay* triangulation. In contrast to classical PFEM calculations, in which the free boundary is obtained by a geometrical procedure ($\alpha-shape$ method), in this work the boundary is considered as a material surface, and the boundary nodes are removed or inserted by means of an error function.

The description of the thermo-mechanical constitutive model is based on the concepts of large strains plasticity. The plastic flow condition is assumed nearly incompressible, so a u-p mixed formulation, with a stabilization of the pressure term via the Polynomial Pressure Projection (PPP), is proposed.

One of the novelties of this work is the use of a combination between the isothermal split (Simo and Miehe [79]) and the so-called IMPL-EX hybrid integration technique (proposed by Oliver, Huespe and Cante [53]) to enhance the robustness and reduce the typical iteration number of the fully implicit Newton-Raphson solution algorithm.

[*]Universitat Politècnica de Catalunya (UPC), Campus Terrassa, C/Colom 11, 08222 Terrassa, Spain.

[†]International Center for Numerical Methods in Engineering (CIMNE), Campus Nord UPC, Gran Capitán, s/n., 08034 Barcelona, Spain. E-mail: cpuigbo@cimne.upc.edu.

[‡]Escola Tècnica Superior d'Enginyeries Industrial i Aeronàutica de Terrassa, Rambla de Sant Nebridi 22, 08222 Terrassa, Spain.

[§]International Center for Numerical Methods in Engineering (CIMNE), Campus Nord UPC, Gran Capitán, s/n., 08034 Barcelona, Spain.

The new set of numerical tools implemented in the PFEM algorithm -including new discretization techniques, the use of a projection of the variables between meshes, and the insertion and removal of points- allows us to eliminate the negative Jacobians present during large deformation problems, which is one of the drawbacks in the simulation of coupled thermo-mechanical problems.

Finally, two sets of numerical results in 2D are stated. In the first one, the behavior of the proposed locking free element type and different time integration schemes for thermo-mechanical problems is analyzed. The potential of the method for modeling more complex coupled problems as metal cutting and metal forming processes is explored in the last example.

Keywords: Particle Finite Element Method (PFEM), Thermo-elastoplasticity, IMPL-EX integration, Remeshing and Geometry Update.

1 Introduction

1.1 Motivation

Thermo-mechanical processes, which involve large strains and rotations, multiple contacts and generation of new surfaces, are a major challenge of the numerical simulation, and thus require advanced numerical techniques. Numerical modeling has been applied to simulate complex thermo-mechanical processes, in order to predict incoming difficulties such as defects in formed parts, improper tool profile, and low lifetime.

First, we lay out a summary of the advantages and drawbacks of the different numerical strategies capable to represent the complex phenomena taking place. The principal problem in the use of a conventional FE model with a Langrangian description is the mesh distortion in high deformation processes. Traditional Langrangian approaches such as FEM cannot resolve the large deformations very well. Element distortion has been always matter of concern that turns the modeling into an incipient analysis. Instead, the FEM with a Eulerian formulation require the knowledge of the deformed geometry in advance, which, undoubtedly, restricts the range of problem conditions capable of being analyzed.

A lagrangian formulation was used to simulate complex thermo-mechanical processes in [50, 61, 81, 81] and [25]. The Eulerian formulation is used in [67]. In order to avoid the disadvantages of Finite Element Lagrangian and Eulerian formulations, other computational techniques have been investigated. One of them is the Finite Element Arbitrary Lagrangian Eulerian (ALE) formulation in conjunction with adaptive mesh techniques [35, 36, 54]. The ALE formulation combines the best features of pure Lagrangian analysis (in which the mesh follows the material) and Eulerian analysis (in which the mesh is fixed and the material flows through the mesh). In ALE framework mesh motion is independent of material motion, for that reason high quality finite element meshes are preserved during the numerical simulation. In addition to the numerical strategies based on the finite element, there exist some recently developed meshless methods. Among them, we can mention the smoothed-particle hydrodynamics (SPH) [47], the finite pointset method (FPM)[84], the constrained natural element method (C-NEM) [29, 43], the discrete element method (DEM) [32], a meshless technique based on a reproducing kernel particle method (RKPM) [23, 66, 19], and a meshless method based on maximum entropy meshfree approximants (MEM) [38]. The main advantage of a meshless method is that it does not need a finite element mesh to calculate derivatives. Material properties and state variables are available at a set of points, called particles. This avoids severe problems associated with mesh tangling and distortion that usually occur in Finite Element Lagrangian formulations involving large deformation and strain rates. The main disadvantage of meshless methods in comparison with the FEM is the neighbors search, because updating the data base of neighbor particles takes usually a long time in comparison with other calculations needed during each time step. Another disadvantage of meshless methods is that due to a fix number of particles used in the numerical simulation, the particles usually concentrate in some region and disperse in other areas. Also, imposing essential boundary conditions in

meshless methods is not as straightforward as for the finite element method. Furthermore, nearly incompressible conditions are a big challenge to meshfree methods. The main objective of this work is precisely to contribute to solve some of the problems described above through the extension of the Particle Finite Element Method (PFEM) to thermo-mechanical problems in solid mechanics that involves large strains and rotations, multiple contacts and generation of new surfaces. In this work, we exploit the particle and lagrangian nature of the PFEM and the advantages of finite element discretization. The new ingredients of PFEM are focused on the insertion and removal of particles, the use of constrained *Delaunay* triangulation and a novel transfer operator of the internal variables, which minimizes the numerical diffusion of internal variables, one of the main disadvantages of the standard finite elements. As a consequence of PFEM basic features, the element distortion is minimized during all the numerical simulation.

1.2 Contents

Next we present the mathematical and numerical ingredients necessary to simulate a classical thermo-mechanical problem, including the balance of momentum and its finite element discretization, and the balance of energy and its finite element discretization. The constitutive equation for the treatment of metals and the used time discretization will be detailed. Particular solutions related to the treatment of the incompressibility constraint and for the improvement of the time integration scheme are explained. All developments are build within the *Particle Finite Element Method* (PFEM).

The paper starts with the definition of the PFEM in section 2, the basic general steps and the custom characteristics used in the present formulation are explained. In section 3 the coupled thermo-mechanical problem is described with a summarized form of the balance equations of the initial boundary value problem (IBVP). The equations are stated using a thermo-elastoplastic split of the problem and particularized with the mixed displacement-pressure formulation used for the finite element discretization. A review of the most used techniques for the treatment of the incompressibility constraint is made. The pressure stabilization method used in this work is explained in detail in this section. The main expressions of the finite element numerical integration of the IBVP are developed in section 4. In section 5 we present an overview of the thermo-elastoplastic model at finite strains proposed by *Simo et al.* in [79, 77, 78]. This model will be used in the examples of section 7 that test the capabilities of the present formulation. Also in section 5, the IMPL-EX scheme for the constitutive law integration is presented. The flow rules, the algorithmic constitutive tensor expression and the expression of the linearization of the algorithmic dissipation are developed and given for the current scheme. The expressions for the dissipation will be used in the thermal solution and also as a error estimates for the mesh update within the PFEM. Three possible time integrations of the IBVP are explained in this work, in section 6 the proposed isothermal IMPL-EX scheme for the time integration of the thermo-mechanical problem is described.

The paper finishes analysing three classical benchmark problems found in the lit-

erature. With these examples we validate the formulation in front of the current state of the art. In section 7 we also include an example of analysis of challenging thermo-mechanical problems. First, a classical steel cutting test-type is presented to show the thermo-mechanical modelling capabilities of the PFEM. In second term, we make a comparison with experimental results and the results from commercial codes to prove the competitiveness of the PFEM in the field of the modelling of thermo-mechanical processes. All problems analysed represent qualitative validations of 2D models.

The theory, presented in synthesized way in each one of the sections, is described in more detail in the appendices.

2 The Particle Finite Element Method

The PFEM is founded on the Lagrangian description of particles and motion and it combines a meshless definition of the continuum containing a cloud of particles with standard mesh-based finite element techniques.

The initial developments of the Particle Finite Element Method (PFEM) took place in the field of fluid mechanics [42, 56], because of the PFEM feasible features of tracking and modeling of free surfaces. Later on, the Particle Finite Element (PFEM) was applied in a variety of simulation problems: fluid structure interaction with rigid bodies, erosion processes, mixing processes, coupled thermo-viscous processes and thermal diffusion problems [58, 57, 59, 60].

The continuum, representing a solid or a fluid, is described by a collection of particles in space. The particles contain enough information to generate the correct boundaries of the analysis domain. Meshing techniques like the *Delaunay* tessellation and the $\alpha-shape$ concept [33] are used to discretize the continuum with finite elements starting from the particle distribution. The meshing process creates continuum sub-domains and identifies the geometrical contacts between different sub-domains.

First applications of PFEM to solid mechanics were done in problems involving large strains and rotations, multiple body contacts and creation of new surfaces (riveting, powder filling, ground excavation and machining) [52, 16, 17, 70]. In this work, we extended the Particle Finite Element Method to the numerical simulation of process involving thermo-mechanical problems.

2.1 Basic steps of the PFEM

In the PFEM the continuum is modelled using an *updated Lagrangian formulation*. That is, all variables are assumed to be known in the *current configuration* at time t. The new set of variables is sought for in the *next or updated configuration* at time $t+\Delta t$ (Figure 1). The finite element method (FEM) is used to solve the continuum equations. Hence a mesh discretizing the domain must be generated in order to solve the governing equations in the standard FEM fashion. Recall that the nodes discretizing the analysis domain are treated as *material particles* which motion is tracked during the transient solution. This is useful to model the separation of particles from the main domain, in groups of particles such as a metal chips in metal cutting problems, or as single

particles such as water drops in fluid problems. In the last case, it is possible to follow the motion of the domain as individual particles with a known density, an initial acceleration and velocity and subject to gravity forces. The mass of a given domain is obtained by integrating the density at the different material points over the domain.

The quality of the numerical solution depends on the discretization chosen as in the standard FEM. Adaptive mesh refinement techniques can be used to improve the solution.

For clarity purposes we will define the *collection or cloud of nodes (C)* belonging to the analysis domain, the *volume (V)* defining the analysis domain and the *mesh (M)* discretizing the domain.

A typical solution with the PFEM involves the following steps.

1. The starting point at each time step is the cloud of points in the analysis domains. For instance C_n denotes the cloud at time $t = t_n$ (1).

2. Identify the boundaries defining the analysis domain V_n. This is an essential step as some boundaries may be severely distorted during the solution, including separation and re-entering of nodes. The $\alpha-shape$ method [33] is used for the boundary definition.

3. Discretize the continuum domains with a finite element mesh M_n.

4. Solve the Lagrangian equations of motion in the domain. Compute the state variables at the next (updated) configuration for $t+\Delta t$: displacements, pressure, temperature, stresses and strains, etc.

5. Move the mesh nodes to a new position C_{n+1} where $n + 1$ denotes the time $t_n + \Delta t$, in terms of the time increment size. This step is typically a consequence of the solution process of step 4.

6. Go back to step 1 and repeat the solution process for the next time step to obtain C_{n+2}. The process is shown in Figure 1.

Figure 1 shows a conceptual example of application of the PFEM to model the progressive fragmentation of a solid mass under the action of an external object.

2.2 Meshing procedure and variables transfer in the PFEM

The original idea of the PFEM was to improve the mesh quality by performing a re-triangulation of the domain only when is needed, that allows to capture large changes in the continuum domain and avoid global remeshing and interpolation from mesh to mesh. Usually that is performed according to some criteria associated to element distortion. This re-triangulation consists in re-computing the element connectivity using a *Delaunay* triangulation [24, 44, 68] where the current position of the particles (i.e. of the mesh nodes) is kept fixed. Mesh distortion is corrected and improved in the naturally with the Particle Finite Element Method (PFEM), because the *Delaunay*

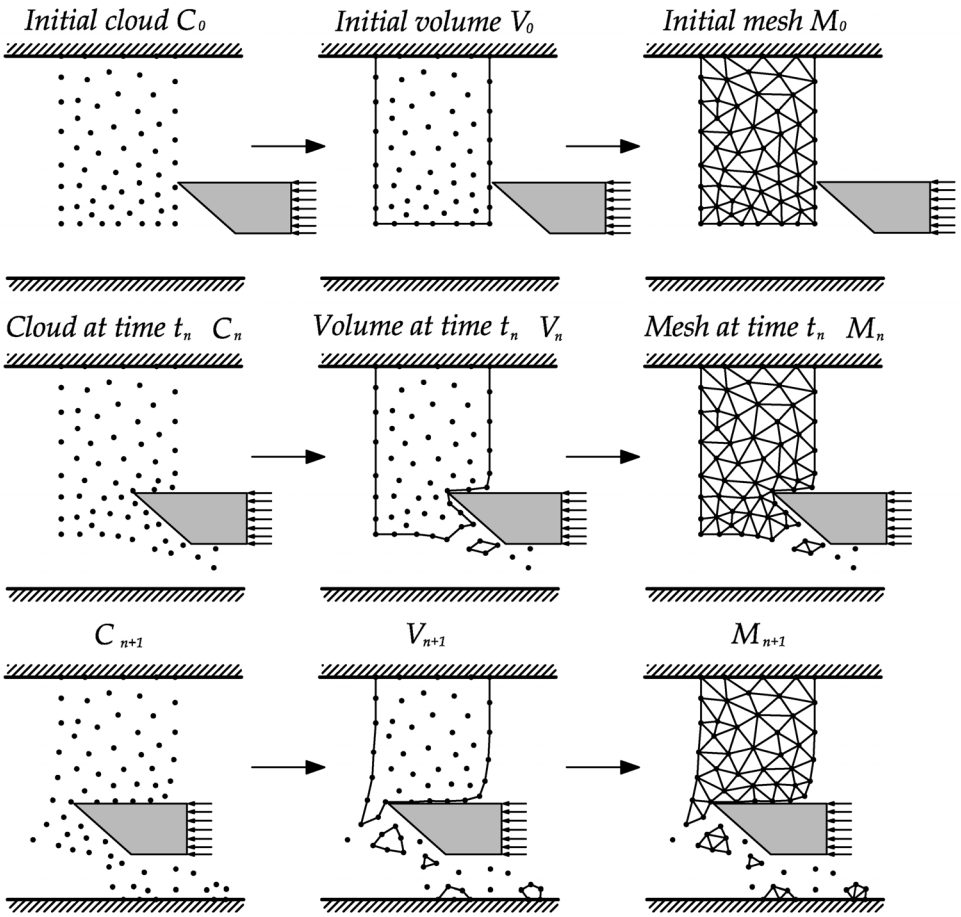

Figure 1: Sequence of steps to update in time a "cloud" of nodes representing a solid mass that is progressively fragmented the action of an external object using the PFEM. In the boundaries the particles are fixed.

triangulations maximize the minimum angle of all the angles of the triangles in the triangulation. Therefore, they tend to avoid skinny triangles.

This strategy has some important implications, the *Delaunay* triangulation generates the convex figure of minimum area which encloses all the points and which may be not conformal with the external boundaries. A possibility to overcome this problem is to couple the *Delaunay* triangulation with the so-called $\alpha-shape$ method. An example of the remeshing scheme using PFEM is shown in Figure (2).

In the Lagrangian approach, the particles move because of the material flow and it may happen that particles concentrate in same regions of the domain and, on the contrary, in other regions the number of particles becomes too low to obtain an accurate solution. To overcome these difficulties PFEM adds and removes particles comparing with a certain characteristic distance h. If the distance between two nodes d_{nodes} is

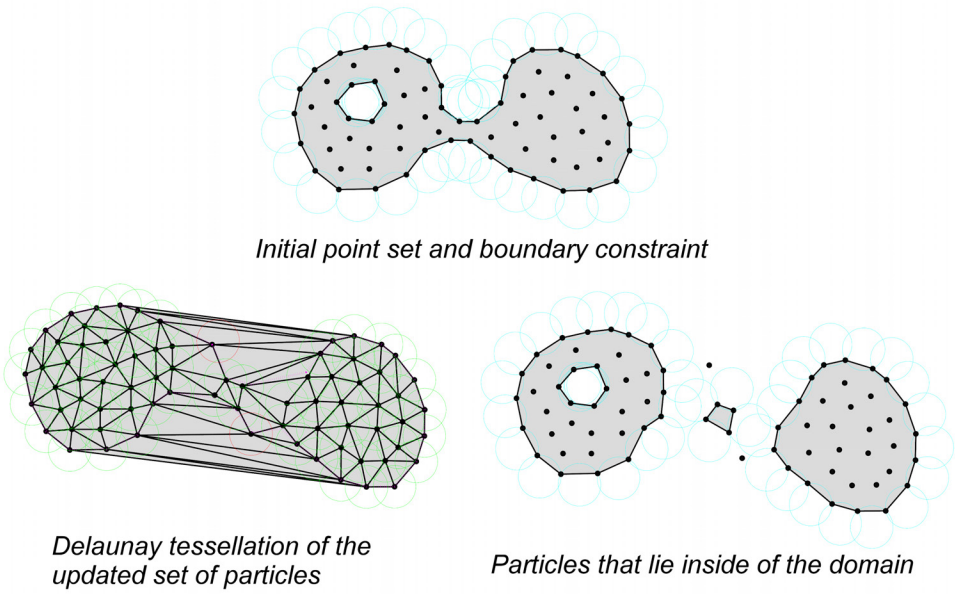

Figure 2: Remeshing steps in an standard PFEM numerical simulation

$d_{nodes} < h$, one of the nodes is removed. If the radius of an element circumsphere r_{ce} is $r_{ec} < h$, a new node is added at the center of the circumsphere. The flow variables in the new node are linearly interpolated from that of the element nodes, and the assigned material properties are the ones of the elements.

The solution scheme described by the PFEM applied to fluid mechanics problems can be summarized by the following steps:

1. The domain is filled with a set of points referred to as "*particles*" which are endowed with initial velocity $\mathbf{v}_0$, pressure p_0 and position $\mathbf{X_0}$. The accuracy of the numerical solution is clearly dependent on the considered number of particles.

2. A starting finite element mesh is generated using the particles as nodes through a *Delaunay* triangulation and external boundaries are identified by means of the $\alpha-shape$ technique.

3. As long as mesh distortion is acceptable, the non-linear Lagrangian form of the governing equations is solved determining the velocity $\mathbf{v}_n$ and the pressure p_n at every node of the mesh.

4. The position of the "*particles*" is updated and if the mesh distortion is no acceptable a new finite element mesh is generated again using the particles as nodes trough a *Delaunay* triangulation.

In the PFEM, the size of each time step is assumed small enough to avoid remeshing during the iterations for the solution of the non-linear equations in the time step itself. Mesh distortion is checked only at convergence.

The usual PFEM presents some weaknesses when applied in Solid Mechanics problems. For example, the external surface generated using $\alpha-shapes$ may affect the mass conservation of the domain analysed. To deal with this problem, in this work we propose the use of a constrained *Delaunay* algorithm [24, 44, 68]. In order to deal with complex material flows where the material can be merged, the use of $\alpha-shapes$ will be essential. In these cases, a non-constrained *Delaunay* tessellation can be employed together with proper techniques to preserve the contour surface and for the mass conservation, see [15]. That also allows the extension to 3D models where, in many cases, the constrained *Delaunay* tessellation is not guaranteed. There are also some other works focussed possible constructions of the constrained *Delaunay* tessellation in 3D, see [73, 75, 69]. For a certain non-convex domains, where the constrained tessellation is not allowed, one possible solution consists in adding some nodes on the border of the domain, see [73, 40]. Furthermore, addition and removal of particles are the principal tools, which we employ for sidestepping the difficulties, associated with deformation-induced element distortion, and for resolving the different scales of the solution. The insertion of particles is based on the equidistribution of plastic power, such that, elements exceeding the prescribed tolerance ε_{tol} are targeted for refinement.

$$\int_{\Omega^e} \mathcal{D}_{mech}\, d\,\Omega^e > \varepsilon_{tol} \tag{1}$$

where $\mathcal{D}_{mech}$ is the mechanical power that will be introduced later on by the equation (168) and Ω^e is the domain of the element. When the condition is fulfilled, a particle is inserted in the gauss point of the finite element.

The removal of particles is based on a Zienkiewicz and Zhu [87, 88] error estimator defined by the expression (2).

$$Error\,(\mathbf{e}) = \left| \frac{\bar{\mathbf{e}}^* - \bar{\mathbf{e}}}{\bar{\mathbf{e}}_{max}} \right| \tag{2}$$

where $\bar{\mathbf{e}}^*$ is the recovered equivalent plastic strain and $\bar{\mathbf{e}}_{max}$ is the maximum equivalent plastic strain. A particle is removed if and only if, the error in all the elements belonging to the particle is less than a given tolerance.

All the information necessary in subsequent time steps has now to be transferred to the new mesh, it includes the nodal information like displacements, temperatures, pressure in the new inserted particles and the Gauss point information like internal variables in the new element. This is achieved using the procedure described in Box 1.

3 The coupled thermo-mechanical problem

We start with the description of the system of partial differential equations governing the evolution of the thermo-mechanical initial boundary value problem (IBVP). This is a solid mechanics problem which uses a Lagrangian description of the continuum medium. Thus the material and spatial Lagrangian descriptions of the governing equations can be used and will be presented in the appendix A. These descriptions are

PROCEDURE FOR MESH REFINEMENT
AND
INFORMATION TRANSFER USED IN THE PFEM

1. Update the particle positions due to motion.
2. Refine elements. Criterion based on plastic dissipation values.
3. Refine boundary that is too distorted. Criterion based on curvature information and plastic dissipation values.
4. Remove particles if error estimators are less or equal than a given value. Error estimators based on plastic strain values or on the norm of the isochoric stresses. A particle is removed if all previous finite elements joined to that particle have an error value less or equal to a given tolerance.
5. Perform a constrained *Delaunay* triangulation in the refined mesh boundary. The triangulation must include remaining and new particles and must delete the triangles outside the boundary
6. Estimate the mesh quality. If mesh quality is less or equal than a given tolerance, develop a Laplacian smoothing [34] of the updated particle positions.
    1. Find smoothed particles in the new mesh
    2. Transfer particle information (displacement, pressure, temperature) to the new particle positions using the shape functions
7. Calculate the global coordinates of the gauss points of the new triangulation.
8. Using the information of the previous mesh, update the internal variables of the new triangulation.
   This step states that the Gauss point information of finite element in the new mesh is the Gauss point information of the closest finite element in the previous mesh.

It is important to remark that step 4 and 6 are optional.
The main advantage of the proposed strategy is that:
It is not necessary to create a complete new mesh; we only adapt the mesh with the addition and removal of particles and the mesh quality is improved using a *Delaunay* triangulation.

Box 1: Flowchart of the refining scheme and information transfer process.

equivalent in continuum mechanics. However, in this work we will focus on the spatial one because is more suitable for the features of the PFEM. The IBVP described by the thermo-mechanical equations can be written in a simpler way using an operator split. This is:

1. Isothermal elastoplastic problem

$$\dot{\mathbf{Z}} = \begin{bmatrix} \dot{\boldsymbol{\varphi}} \\ \rho\dot{\mathbf{v}} \\ \dot{\theta} \end{bmatrix} = \begin{bmatrix} \mathbf{v}(\mathbf{x},t) \\ \mathbf{div}\ (\boldsymbol{\sigma}(\boldsymbol{\varphi},\theta,\lambda(\boldsymbol{\varphi},\theta))) \\ 0 \end{bmatrix} + \begin{bmatrix} 0 \\ \mathbf{b} \\ 0 \end{bmatrix} \tag{3}$$

2. Thermoplastic problem at a fixed configuration

$$\dot{\mathbf{Z}} = \begin{bmatrix} \dot{\boldsymbol{\varphi}} \\ \rho\dot{\mathbf{v}} \\ \dot{\theta} \end{bmatrix} = \begin{bmatrix} 0 \\ 0 \\ -\mathbf{div}\ (\mathbf{q}(\boldsymbol{\varphi},\theta,\lambda(\boldsymbol{\varphi},\theta))) + \mathcal{D}_{int} \end{bmatrix} + \begin{bmatrix} 0 \\ 0 \\ r \end{bmatrix} \tag{4}$$

In equations (3) and (4), ρ is the density, $\mathbf{v}$ is the velocity field and $\dot{\mathbf{v}}$ it the acceleration, where $(\dot{})$ expresses the time derivative. The motion $\dot{\boldsymbol{\varphi}}$ and the absolute temperature θ are regarded as the primary variables in the problem while $\mathbf{b}$ the body force per unit of spatial volume and r the heat source per unit of spatial volume are prescribed data. In equation (4), $\mathcal{D}_{int}$ is the internal dissipation per unit of spatial volume. In addition, the heat flux $\mathbf{q}$ as well as the Cauchy stress tensor $\boldsymbol{\sigma}$ are defined via constitutive equations, where $\lambda(\boldsymbol{\varphi},\theta)$ expresses the set of internal constitutive variables.

Further details of the coupled thermo-mechanical IBVP are presented in the appendix A.

3.1 Mixed displacement-pressure formulation for the IBVP

It is well known that pure displacement formulations are not suitable for problems in which the constitutive behavior exhibit incompressibility since they tend to experience locking. Locking means, in this context, that the constraint conditions due to incompressibility cannot be satisfied. These constraint conditions are related to the pure volumetric mode (in the elastic case the condition is $\det(\mathbf{F}^e) = 1$, see equation (93) and for the plastic flow the condition is $\det(\mathbf{F}^p) = \det(\mathbf{C}^p) = 1$, see equation (94)). Thus, this behavior is also called volume locking. As locking is present in the modelling of metal plasticity, we adopt a mixed formulation in the momentum balance equation of the workpiece [18]. Introducing a pressure/deviatoric decomposition of the Cauchy stress tensor, the standard expression of the weak form of the equilibrium equation becomes

$$\left.\begin{aligned} \mathbf{G}_{\mathbf{u},dyn} &= \langle dev(\boldsymbol{\sigma}) + p\mathbb{1}, \nabla^s\boldsymbol{\eta}\rangle - \langle\boldsymbol{\eta},\mathbf{b}\rangle - \langle\mathbf{t},\boldsymbol{\eta}\rangle_{\gamma_\sigma} + \langle\boldsymbol{\eta},\rho\dot{\mathbf{v}}\rangle = 0 \\ \mathbf{G}_{\theta,dyn} &= -\langle\nabla\zeta,\mathbf{q}\rangle - \langle\zeta,\mathcal{D}_{int}\rangle - \langle\zeta,\mathbf{q}\cdot\mathbf{n}\rangle_{\gamma_\mathbf{q}} + \langle\zeta,\dot{e}\rangle = 0 \\ \mathbf{G}_{\boldsymbol{\tau}} &= \left\langle \kappa\ \ln(J) - 3\,\alpha\,\kappa\,\frac{(1-\ln(J))}{J}(\theta-\theta_0), q \right\rangle + \langle p,q\rangle = 0 \end{aligned}\right\} \begin{array}{l} \forall\boldsymbol{\eta}\in \mathrm{V}, \\ \forall\zeta\in \mathrm{T}, \\ \forall q\in Q \end{array} \tag{5}$$

where $\kappa > 0$ and α can be interpreted as the bulk modulus and the thermal expansion coefficient, respectively. J is the determinant of the deformation gradient, see equation (93). The pressure is denoted by p, $\mathbf{t}$ is the surface traction, e is the internal energy per unit of spatial volume and $\mathbf{n}$ is the surface normal. The initial temperature is set as θ_0. Being $\boldsymbol{\eta} \in \mathrm{V}$, $\zeta \in \mathrm{T}$ and $q \in \mathrm{Q}$ valued functions in the space of virtual displacements V, virtual temperatures T and virtual pressures Q respectively. The L_2 inner product is represented as $\langle \cdot, \cdot \rangle$, and with a slight abuse in notation $\langle \cdot, \cdot \rangle_{\gamma_\sigma}$ and $\langle \cdot, \cdot \rangle_{\gamma_\mathbf{q}}$ is denoting the L_2 inner product on the boundaries γ_σ and $\gamma_\mathbf{q}$, respectively.

The weak form of the IBVP and the details of the mixed displacement-pressure formulation are developed in appendix A.4.

3.2 Numerical treatment of the incompressibility constraint

The most common finite elements used in the numerical simulations involving plasticity at finite strains are, in 2D: the plane strain isoparametric quadrilateral element used in [74, 81, 86], the 6 noded isoparametric triangle element used in [74] and [50], and the enhanced four node quadrilateral with 1-point quadrature used in [61]. When finite elements have linear order of interpolation, the performance for the treatment of the incompressibility is very poor. Usually the problems appear with the use of linear triangles and linear tetrahedra under incompressible and nearly incompressible conditions. This is exactly the case we encounter when the PFEM is employed. In order to surpass this inconvenience different type of finite elements have been developed. They can be classified in four groups mainly:

1. Mixed enhanced element. The enhanced strain technique, essentially consists in augmenting the space of discrete strains with local functions [3].

2. Composite pressure fields. The most representative finite elements with composite pressure fields are F-Bar [63, 51] and Composite Triangles [13, 39].

3. Average Nodal Pressure. The *Average Nodal Pressure* (ANP) was presented in [9] and [10] in the framework of explicit dynamics and by [64] in the framework of implicit dynamics. Another references for the ANP are [65][27]and [27]. There are alternative formulations based in node average of the variables. The Node Based Uniform Strain Elements (NBUSE) [30, 37], the Average Nodal Deformation Gradient (ANDG) [11] and the Mixed Discretization Technique (MD) [49], improved in [28] creating their formulation called Nodal Mixed discretization (NMD).

4. Pressure stabilized finite elements

In this work we have chosen the pressure stabilized option for the treatment of the incompressibility constraint. The details set out below.

3.2.1 Pressure stabilization

This element technology is applied to linear finite elements formulated in a mixed displacement-pressure or velocity-pressure field. When the order of interpolation of the pressure field of the finite element is the same as the order of interpolation of the displacement field, the solution presents nonphysical oscillations. Mathematically, it means that equal order interpolation for displacement and pressure does not satisfy Babuska-Brezzy condition. In order to remove these undesirable oscillations, a literature overview shows different strategies. Among them: The Characteristic Based Split (CBS)[22], the finite calculus (FIC) [55], the Orthogonal Subgrid Scales (OSS) [72, 20, 21] and the Polynomial Pressure Projection (PPP) [31, 6].

After looking at the advantages and disadvantages of the cited pressure stabilization techniques, we have chosen the use of the PPP for the development of our finite element. The theoretical explanation for this technique is summarized next.

3.2.2 Polynomial Pressure Projection(PPP)

Mixed formulations have to fulfill additional mathematical conditions, which guarantee its stability. Linear displacement-pressure triangles and tetrahedra finite elements do not satisfy Babuska-Brezzy condition; consequently, a stabilization of the pressure field is needed.

In our approach the stabilization method utilized is the so-called Polynomial Pressure Projection(PPP) presented and applied to stabilize Stokes equations in [6, 31]. The PPP is based on two ingredients:

1. The use a mixed equal order interpolation of the pressure and displacement/velocity fields

2. The use of a L_2 pressure projection

The method is obtained by modification of the mixed variational equation by using local L_2 polynomial pressure projections. The application of the pressure projections in conjunction with minimization of the pressure-displacement mismatch, eliminates the inconsistency of equal-order approximations and leads to a stable variational formulation. Unlike other stabilization methods, the Polynomial pressure projection (PPP) does not require specification of a mesh dependent stabilization parameter or calculation of higher-order derivatives. The PPP uses a projection on a discontinuous space and as a consequence can be implemented in an elementary level surpassing the need of mesh dependent and problem dependent parameters. The implementation of the PPP reduces to a simple modification of the weak continuity equation (incompressibility constraint). In this work, we extend the PPP to solid mechanics problems involving large strains.

Given a function $p \in L_2$, the L_2 projection operator $\breve{p} : L_2 \to Q^0$ is defined by

$$\mathbf{G}_{\boldsymbol{\tau},p} = \int_{V_t} \breve{q}\,(p - \breve{p}) dV_t = 0 \quad \forall \breve{q} \in Q^0 \tag{6}$$

where $\breve{p}$ is the best approximation of the pressure p in the space of polynomials of order $\mathcal{O}(Q^0)$. V_t is the volume of the domain at the current configuration.

To stabilize the mixed form given by equations (5), we add the projection operator to the third equation in (5)

$$\mathbf{G}_{stab,p} = \int_{V_t} (q - \breve{q}) \frac{\alpha_s}{\mu} (p - \breve{p}) dV_t = 0 \tag{7}$$

where α_s is the stabilization parameter and μ is the material shear modulus.

The use of the projection operator to the pressure test and trial functions removes the approximation inconsistency present for equal-order displacement and pressure spaces.

The role of the form $\mathbf{G}_{stab,p}$ is to further penalize pressure variation away from the range of the divergence operator. Taking into account the mixed formulation and the polynomial pressure stabilization terms to deal with the incompressibility phenomena, the momentum and energy balance equations take the form:

$$\left.\begin{array}{l} \mathbf{G}_{\mathbf{u},dyn} = 0 \\ \mathbf{G}_{\theta,dyn} = 0 \\ \mathbf{G}_{\boldsymbol{\tau}} + \mathbf{G}_{stab,p} = 0 \end{array}\right\} \forall \boldsymbol{\eta} \in \mathrm{V}, \forall \zeta \in \mathrm{T}, \forall q \in Q \tag{8}$$

where

$$\mathbf{G}_{\boldsymbol{\tau}} = \mathbf{G}_{\boldsymbol{\tau},p} + \langle p, q \rangle \tag{9}$$

$$\mathbf{G}_{\boldsymbol{\tau},p} = \left\langle \kappa \, \ln(J) - 3 \, \alpha \, \kappa \, \frac{(1 - \ln(J))}{J} (\theta - \theta_0), q \right\rangle \forall q \in Q \tag{10}$$

and

$$\mathbf{G}_{stab,p} = \left\langle \frac{\alpha_s}{\mu} (p - \breve{p}), q - \breve{q} \right\rangle \forall \breve{p}, \breve{q} \in Q^0 \tag{11}$$

The set of governing equations for the displacement, pressure and temperature variables is completed by adding the proper initial conditions and constraint equations related to the problem variables.

4 Finite element numerical integration of the IBVP

Consider a spatial discretization $\Omega = \bigcup_{e=1}^{n_e} \Omega^{(e)}$ into a disjoint collection of non-overlapping elements $\Omega^{(e)}$ with characteristic size $h^{(e)}$, being n_e the total number of elements. The finite element method for numerical solution of problem (8) consists on replacing the functional sets $\{\mathbf{u}, V\}$, $\{\theta, T\}$ and $\{p, P\}$ with discrete subsets $\{\mathbf{u}^h, V^h\}$, $\{\theta^h, T^h\}$ and $\{p^h, P^h\}$ generated by a finite element discretization h of the domain Ω. Let $\omega(\mathbf{X}, t)$ be a generic scalar or vector field defined over the domain Ω_e of the element. The finite element interpolation of the field ω within element (e) is obtained as

$$\omega^{h\,(e)}(\mathbf{X},t) = \sum_{j=1}^{n_n} \omega_j {N_j}^{(e)}(\mathbf{X},t) \tag{12}$$

where n_n is the number of nodes of an element, ω_j is the value of ω at node j, and ${N_j}^{(e)}$ is the shape function such that its value is 1 at the node j and zero at any other node of the element.

The interpolated function, now defined over the approximated domain is given by

$$\omega^h(\mathbf{X},t) = \sum_{j=1}^{n_p} \omega_j N_j(\mathbf{X},t) \tag{13}$$

where N_j is a piecewise polynomial function (the global shape function) associated with the global node j and n_p is the total number of nodal points in the finite element mesh.

With the introduction of the above interpolation procedure, we generate the finite dimensional sets. The discrete counterpart of (8) is given then by the equations:

$$\int_{V_t} {\mathbf{B}_u}^T \boldsymbol{\sigma}\, dV_t - \int_{V_t} \mathbf{N}^T \mathbf{b}\, dV_t - \int_{V_t} \mathbf{N}^T \rho \dot{\mathbf{v}}\, dV_t - \int_{\gamma_\sigma} \mathbf{N}\mathbf{t}\, d\gamma_\sigma = 0 \tag{14}$$

$$\int_{V_t} c\,\mathbf{N}\mathbf{N}^T \dot{\theta}\, dV_t - \int_{V_t} {\mathbf{B}_\theta}^T \mathbf{q}\, dV_t - \int_{V_t} \mathbf{N}^T \mathcal{D}_{int}\, dV_t + \int_{\gamma_\mathbf{q}} \mathbf{N}^T (\mathbf{q}\cdot\mathbf{n})\, d\gamma_\mathbf{q} = 0 \tag{15}$$

$$\int_{V_t} \frac{1}{\kappa} \mathbf{N}\mathbf{N}^T p\, dV_t - \int_{V_t} \mathbf{N}^T \left(\ln(J) - 3\,\alpha\, \frac{(1-\ln(J))}{J} (\theta - \theta_0) \right) dV_t + \mathbf{F}^{(e)}_{p,stab} = 0 \tag{16}$$

where c is the specific heat of the material, $\mathbf{B}_u$ and $\mathbf{B}_\theta$ are the strain-displacement matrix and the global gradient-temperature matrix respectively. That matrices contain the derivatives of the shape functions used in the interpolation of the problem variables.

$\mathbf{F}^{(e)}_{p,stab}$ expresses the discrete counterpart of the projection operator, accounting that the pressure projection is constant and discontinuous among finite elements.

$$\mathbf{F}^{(e)}_{p,stab} = \int_{{V_t}^{(e)}} \frac{\alpha_s}{\mu}\, p^{(e)} \left(\mathbf{N}^{(e)} \mathbf{N}^{T\,(e)} - \tilde{\mathbf{N}}^{(e)} \tilde{\mathbf{N}}^{T\,(e)} \right) {dV_t}^{(e)} \tag{17}$$

If $\mathbf{N}^{(e)}$ contain the set of polynomials of order k, $\tilde{\mathbf{N}}^{(e)}$ contain the set of polynomials of order $k-1$.

The equilibrium incompressible equations (8) can be expressed alternatively as follows. Starting with the balance of the linear momentum (14):

$$\mathbf{F}_{\mathbf{u},dyn}(\ddot{\mathbf{u}}) - \mathbf{F}_{\mathbf{u},int}(\mathbf{u},\mathbf{p}) + \mathbf{F}_{\mathbf{u},ext} = 0 \tag{18}$$

where

$$\mathbf{F}_{\mathbf{u},int}(\mathbf{u},\mathbf{p}) = \int_{V_t} \mathbf{B}_u{}^T \boldsymbol{\sigma}\, dV_t \tag{19}$$

$$\mathbf{F}_{\mathbf{u},ext} = \int_{V_t} \mathbf{N}^T \mathbf{b}\, dV_t - \int_{\gamma_\sigma} \mathbf{N}\mathbf{t}\, d\gamma_\sigma \tag{20}$$

$$\mathbf{F}_{\mathbf{u},dyn}(\ddot{\mathbf{u}}) = \int_{V_t} \mathbf{N}^T \rho \ddot{\mathbf{u}}\, dV_t \tag{21}$$

The equation for the energy balance (15) are written as

$$\mathbf{F}_{\theta,dyn}(\ddot{\theta}) - \mathbf{F}_{\theta,int}(\theta) + \mathbf{F}_{\theta,ext} = 0 \tag{22}$$

where

$$\mathbf{F}_{\theta,int}(\theta) = \int_{V_t} \mathbf{B}_\theta{}^T \mathbf{q}\, dV_t - \int_{V_t} \mathbf{N}^T \mathcal{D}_{int}\, dV_t \tag{23}$$

$$\mathbf{F}_{\theta,int} = \int_{\gamma_\mathbf{q}} \mathbf{N}^T (\mathbf{q}\cdot\mathbf{n})\, d\gamma_\mathbf{q} \tag{24}$$

$$\mathbf{F}_{\theta,dyn}(\ddot{\theta}) = \int_{V_t} c\, \mathbf{N}\mathbf{N}^T \dot{\theta}\, dV_t \tag{25}$$

and the incompressibility balance equations (16) are written as

$$\mathbf{F}_{\mathbf{p},pres}(\mathbf{p}) - \mathbf{F}_{\mathbf{p},vol}(\mathbf{u}) + \mathbf{F}_{\mathbf{p},stab}(\mathbf{p}) = 0 \tag{26}$$

where

$$\mathbf{F}_{\mathbf{p},pres}(\mathbf{p}) = \int_{V_t} \frac{1}{\kappa} \mathbf{N}\mathbf{N}^T p\, dV_t \tag{27}$$

$$\mathbf{F}_{\mathbf{p},vol}(\mathbf{u}) = \int_{V_t} \mathbf{N}^T \left(\ln(J) - 3\,\alpha\, \frac{(1-\ln(J))}{J}(\theta-\theta_0) \right) dV_t \tag{28}$$

$$\mathbf{F}_{p,stab}(\mathbf{p}) = \int_{V_t{}^{(e)}} \frac{\alpha_s}{\mu}\, \mathbf{p}^{(e)} \left(\mathbf{N}^{(e)}\mathbf{N}^{T\,(e)} - \tilde{\mathbf{N}}^{(e)}\tilde{\mathbf{N}}^{T\,(e)} \right) dV_t{}^{(e)} \tag{29}$$

In finite element computations, the above force vectors are obtained as the assemblies of element vectors. Given a nodal point, each component of the global force associated with a particular global node is obtained as the sum of the corresponding contributions from the element force vectors of all elements that share the node. In this work, the element force vectors are evaluated using Gaussian quadratures.

5 Thermo-elastoplasticity model at finite strains

In this section, the formulation of the constitutive thermo-plasticity model at finite strains will be summarized. Some models are proposed in the literature to deal with thermo-plasticity accounting for the characteristics of the material behavior. If the plastic behavior experiences isotropic hardening, the approach proposed by *Simo et al.* [79, 77, 78] is usually followed. When the strain and strain rate hardening and the thermal softening is considered, other models can be used: (i) *Voce* [85] and *Simo et al.* [80] (ii) *Johnson and Cook* [45] and (iii) *Bäker* [4]. In Box 2 we present the main equations of the thermo-mechanical J_2 flow model for rate independent plasticity that will be used in this work. Details of the theory of thermo-plasticity as well the definition of the variables that appear in Box 2 are explained in appendix B.

The purpose of presenting here the main equations for the constitutive model is to introduce later a new integration scheme for thermo-hyperelastoplasticity called IMPL-EX scheme, see [53].

5.1 Time integration of the constitutive law

The problem of integrating numerically the initial-value ODE equations configured by the Evolution equations and the *Kuhn-Tucker* conditions (see Box 2) is the main objective of this section.

In Box 3 the integration flowchard for the Backward-Euler method is presented. The implicit Backward-Euler method is the most commonly used integration scheme for plasticity. The details of the constitutive law integration are given in the appendix C. The equation $g(\Delta\lambda_{n+1})$ related to the obtention of the consistency parameter $\Delta\lambda_{n+1}$ (see Box 2) is effectively solved by a local Newton iterative procedure. The convergence of the Newton-Raphson is guaranteed if $g(\Delta\lambda_{n+1})$ is a convex function. In this work we use isotropic hardening functions that makes $g(\Delta\lambda_{n+1})$ convex. Although the convergence of the integration is guaranteed, the fully implicit integration of the constitutive law requires some relevant computational effort and can experience some numerical problems of robustness when the material failure appears.

To improve the performance in the integration of the constitutive law, we introduce the integration of the constitutive law by means of the IMPL-EX scheme. Next, we develop the IMPL-EX integration for the thermo-hyperelastoplastic constitutive model used in this work.

5.2 IMPL-EX integration scheme

The IMPL-EX (IMPLicit-EXplicit) adopted herein is the one pioneered by *Oliver et. al.*[53], originally conceived for addressing the problem of robustness and stability arising in the numerical simulation of material failure. The essence of the method is to solve explicitly for some variables, in the sense that the values at the beginning of the increment are presumed known, and implicitly for other variables, with the primary motivation to enhance the spectral properties of the algorithmic tangent moduli.

COUPLED THERMO-MECHANICAL J_2 FLOW THEORY
RATE INDEPENDENT PLASTICITY

1. Free energy function.

$$\hat{\psi} = \hat{T}(\theta) + \hat{M}(\theta, J^e) + \hat{U}(J^e) + \hat{W}(\bar{\mathbf{b}}^e) + \hat{K}(\bar{e}^{\,p}, \theta)$$

2. kirchhoff stress.

$$\begin{aligned} \boldsymbol{\tau} &= J^e\, p\, \mathbb{1} + \mathbf{s} \\ p &:= \left[-3\,\alpha\,\kappa\, \frac{(1-\ln(J^e))}{J^e}(\theta-\theta_0) + \kappa\, \ln(J^e) \right] \\ \mathbf{s} &:= \mu\, dev(\bar{\mathbf{b}}^e) \end{aligned}$$

and the entropy

$$\begin{aligned} \eta &= \eta^p - \eta^e + \eta^t \\ \eta^e &:= -\partial_\theta \hat{T}(\theta) \\ \eta^t &:= -\partial_\theta \hat{M}(\theta, J^e) - \partial_\theta \hat{K}(\bar{e}^{\,p}, \theta) \end{aligned}$$

3. *Von Mises* yield criterion.

$$\Phi(\tau, \bar{e}^{\,p}, \theta) = \| dev(\tau) \| - \sqrt{\frac{2}{3}}\,(\sigma_y + \beta) \leq 0$$

4. Evolution equations $\lambda > 0, \;\; \Phi \leq 0, \;\; \lambda\,\Phi = 0$

$$\begin{aligned} \mathcal{L}_v \mathbf{b}^e &= -2\,\lambda\, J^{-\frac{2}{3}} \frac{1}{3} tr(\bar{\mathbf{b}}^e)\mathbf{n} \\ \dot{\bar{e}}^{\,p} &= -\lambda\, \partial_\beta \Phi(\tau, \bar{e}^{\,p}, \theta) \\ \dot{\eta}^p &= \lambda\, \partial_\theta \Phi(\tau, \bar{e}^{\,p}, \theta) \end{aligned}$$

The definition of the variables that appear in this box are explained in appendix B.

Box 2: Coupled thermo-mechanical J_2 flow theory. Rate independent plasticity.

BACKWARD-EULER INTEGRATION FLOWCHART

1. Thermoelastic trial state:

   Initial data: $\bar{\mathbf{b}}^e_n,\ \bar{e}^{\,p}_n,\ \eta^p_n$

   Current values of $\mathbf{F}_{n,n+1},\ \theta_{n+1},$ where $\bar{\mathbf{F}}_{n,n+1} = J^{-\frac{1}{3}}\mathbf{F}_{n,n+1}$

   Let $f^{trial}_{n+1} = \left\|\mathbf{s}^{trial}_{n+1}\right\| - \sqrt{\frac{2}{3}}\left(\sigma_{y,n+1} + \beta_{n+1}(\bar{e}^p_n)\right)$

   IF $f^{trial}_{n+1} \leq 0$: Set $(\bar{\mathbf{b}}^e_{n+1},\ \bar{e}^{\,p}_{n+1},\ \eta^p_{n+1}) = (\bar{\mathbf{b}}^{e,trial}_n,\ \bar{e}^{\,p}_n,\ \eta^p_n\ )$ and EXIT

   ELSE:

2. Consistency parameter:

   Set $\bar{\mu} = \frac{\mu}{3} tr(\bar{\mathbf{b}}^{e,trial}_{n+1})$

   Compute $\Delta\lambda_{n+1}$ by solving:

$$\begin{aligned} g(\Delta\lambda_{n+1}) &= f^{trial}_{n+1} - 2\,\Delta\lambda_{n+1}\,\mu\,\frac{1}{3}tr(\bar{\mathbf{b}}^{e,trial}_{n+1}) \\ &+ \sqrt{\frac{2}{3}}\left(\sigma_{y,n} + \beta_n(\bar{e}^p_n)\right) - \sqrt{\frac{2}{3}}\left(\sigma_{y,n+1} + \beta_{n+1}(\bar{e}^p_{n+1})\right) = 0 \end{aligned}$$

   Return mapping:

   Set $\mathbf{n}_{n+1} = \dfrac{\mathbf{s}^{trial}_{n+1}}{\|\mathbf{s}^{trial}_{n+1}\|}$ and update

$$\begin{aligned} \mathbf{s}_{n+1} &= \mathbf{s}^{trial}_{n+1} - 2\,\Delta\lambda_{n+1}\,\mu\,\frac{1}{3}tr(\bar{\mathbf{b}}^{e,trial}_{n+1})\mathbf{n}_{n+1} \\ \bar{e}^{\,p}_{n+1} &= \bar{e}^{\,p}_n - \lambda_{n+1}\Delta t\sqrt{\frac{2}{3}} \\ \eta^p_{n+1} &= \eta^p_n - \sqrt{\frac{2}{3}}\Delta\lambda_{n+1}\partial_\theta\left(\sigma_{y,n+1} + \beta_{n+1}(\bar{e}^p_{n+1})\right) \end{aligned}$$

3. Update the intermediate configuration by the closed form formula:

$$\bar{\mathbf{b}}^e_{n+1} = \bar{\mathbf{b}}^{e,trial}_{n+1} - 2\,\Delta\lambda_{n+1}\,\frac{1}{3}tr(\bar{\mathbf{b}}^{e,trial}_{n+1})\mathbf{n}_{n+1}$$

   END

The definition of the variables that appear in this box are explained in appendices B and C.

Box 3: Implicit Backward-Euler integration flowchart for thermo-elastoplastic models.

However, our primary motivation of using IMPL-EX is to reduce the equation solving effort associated to the solution of the fully implicit scheme. The explicit integration of some variables in the coupled thermo-mechanical J_2 flow theory and therefore, the use of extrapolated values in the balance of momentum and energy, allow us to solve a coupled thermo-mechanical problem as a sequence of three uncoupled problems. First, an elastic problem with shear modulus changing from element to element; second, a thermal problems with a temperature dependent plastic heat source and finally, a relaxation process affecting the stress and the internal variables at the integration points. It is important, to remark, that the mechanical and thermal problem are solved using the IMPL-EX integration scheme for the J_2 plasticity model, while in the relaxation steps, stresses and internal variables are calculated using the implicit Back-Euler time integration presented in Box 3 and explained in detail in appendix C.1. The arguments in support of the IMPL-EX integration scheme for the numerical simulation of metal thermo-mechanical processes were already put forward above. Here we simply choose the variable to be treated explicitly and derive the stress update algorithm arising from this choice.

By definition, the equivalent plastic strain is a monotonically increasing function of time, $\dot{\bar{e}}^p \geq 0$. For this reason, it is a logical candidate to be treated explicitly, since its evolution can be predicted more accurately than other variables exhibiting non-monotonic behavior. The following analysis pursues, to develop an expression for explicitly updating the equivalent plastic strain at t_{n+1} using values obtained in previous time steps by an implicit Backward-Euler integration procedure.

Let us consider, the Taylor expansion of the equivalent plastic strain at t_{n-1} around t_n:

$$\bar{e}^p_{n-1} = \bar{e}^p_n - \left.\frac{\partial \bar{e}^p}{\partial t}\right|_{t_n} (t_n - t_{n-1}) + \mathcal{O}(\Delta^2 t_n) \tag{30}$$

Next, the Taylor expansion is carried out at t_{n+1} around t_n, yielding

$$\bar{e}^p_{n+1} = \bar{e}^p_n + \left.\frac{\partial \bar{e}^p}{\partial t}\right|_{t_n} (t_{n+1} - t_n) + \mathcal{O}(\Delta^2 t_{n+1}) \tag{31}$$

The standard explicit difference scheme is obtained truncating the remainder terms $\mathcal{O}(\Delta^2 t_{n+1})$.

The earlier explicit difference equation presents an inconvenience that ensure that the yield condition is not enforced at t_{n+1} and as a result, it is possible for the solution, over many time steps, to drift away from the yield surface. In order to avoid that this drift from the yield surface grows unboundedly, *Oliver et al.* [53] propose to approximate the derivative in (31) using the derivative appearing in (30).

Hence, truncating the terms $\mathcal{O}(\Delta^2 t_{n+1})$ in equation (30), one gets

$$\bar{e}^p_n = \bar{e}^p_{n-1} + \left.\frac{\partial \bar{e}^p}{\partial t}\right|_{t_n} (\Delta t_n) \tag{32}$$

The earlier equation is a Backward-Euler integration of the equivalent plastic strain, in the sense that the equivalent plastic strain at t_n, $\bar{e}^p_n$, is obtained by an expression that uses a derivative evaluated at t_n. As a result, $\bar{e}^p_n$ and $\bar{e}^p_{n-1}$ are obtained at times t_n and t_{n-1} using the implicit scheme presented in the previous section. From (32), we can deduce that

$$\left.\frac{\partial \bar{e}^{\,p}}{\partial t}\right|_{t_n} = \frac{\bar{e}^p_n - \bar{e}^p_{n-1}}{\Delta t_n} \tag{33}$$

Finally, inserting the expression (33) into (31), and truncating the remainder terms, yields

$$\tilde{\bar{e}}^{\,p}_{n+1} = \bar{e}^p_n + (\bar{e}^p_n - \bar{e}^p_{n-1})\,\frac{\Delta t_{n-1}}{\Delta t_n} \tag{34}$$

Expression (34) constitutes an explicit extrapolation of the equivalent plastic strain at t_{n+1} in terms of the implicit values computed at t_n and t_{n-1}. Note that the IMPL-EX algorithm is a multistep method, since two points are used to advance the solution in time to point t_{n+1}.

The algorithmic plastic multiplier resulting from this extrapolation reads:

$$\begin{aligned} \Delta\tilde{\lambda}_{n+1} &= \sqrt{\frac{3}{2}}(\tilde{\bar{e}}^{\,p}_{n+1} - \bar{e}^p_n) \\ &= \sqrt{\frac{3}{2}}(\bar{e}^p_n - \bar{e}^p_{n-1})\frac{\Delta t_{n+1}}{\Delta t_n} \\ &= \sqrt{\frac{3}{2}}\Delta\lambda_n\frac{\Delta t_{n+1}}{\Delta t_n} \end{aligned} \tag{35}$$

Expression (35) reveals that the elastic or plastic nature of the response predicted by the IMPL-EX integration scheme at t_{n+1} is dictated by the response computed implicitly at t_n. This may give rise to overshoots and oscillations in the transitions from elastic to inelastic and vice versa. Now, steps 3 and 4 in Box 3 can be pursued in terms of extrapolated plastic multiplier yielding the IMPL-EX integrated values of the remaining variables $\tilde{\mathbf{S}}_{n+1}$, $\tilde{\bar{e}}^{\,p}_{n+1}$ and $\tilde{\eta}^{\,p}_{n+1}$. Those IMPL-EX results will be replaced later in Box 6 to fulfill the momentum and energy equations. The IMPL-EX explicit stage for both cases is summarized in Box 4.

5.3 Algorithmic constitutive tensor and algorithmic dissipation

The ultimate goal in the numerical simulation of thermo-mechanical processes is to solve an initial boundary value problem (IBVP) for the displacement and temperature fields. The numerical solution of this problem relies on the spatial discretization, via a Galerkin finite element, of the momentum and energy equations and a time discretization of the displacement, velocity and temperature fields. In case of an implicit

IMPL-EX INTEGRATION FLOWCHART

1. Explicit extrapolation stage:

   Initial data: $\bar{\mathbf{b}}^e_n$, $\bar{e}^{\,p}_n$, η^p_n

   Current values of $\mathbf{F}_{n,n+1}$, θ_{n+1}

$$\begin{aligned} \Delta\tilde{\lambda}_{n+1} &= \sqrt{\frac{3}{2}}\Delta\lambda_n \frac{\Delta t_{n+1}}{\Delta t_n} \\ \tilde{\bar{e}}^{\,p}_{n+1} &= \tilde{\bar{e}}^{\,p}_n + \sqrt{\frac{2}{3}}\Delta\tilde{\lambda}_{n+1} \end{aligned}$$

2. Let $\bar{\mathbf{F}}_{n,n+1} = J^{-\frac{1}{3}}\mathbf{F}_{n,n+1}$ and set:

$$\begin{aligned} \bar{\mathbf{b}}^{e,trial}_{n+1} &= \bar{\mathbf{F}}_{n+1}\,\bar{\mathbf{b}}^e_n\,\bar{\mathbf{F}}^T_{n+1} \\ \mathbf{s}^{trial}_{n+1} &= \mu\, dev(\bar{\mathbf{b}}^{e,trial}_{n+1}) \end{aligned}$$

3. Compute stresses and plastic entropy:

   Set $\bar{\mu} = \dfrac{\mu}{3}\, tr(\bar{\mathbf{b}}^{e,trial}_{n+1})$

   Set $\mathbf{n}_{n+1} = \dfrac{\mathbf{s}^{trial}_{n+1}}{\|\mathbf{s}^{trial}_{n+1}\|}$ and update:

$$\begin{aligned} \tilde{\mathbf{s}}_{n+1} &= \mathbf{s}^{trial}_{n+1} - 2\,\Delta\tilde{\lambda}_{n+1}\,\bar{\mu}\,\mathbf{n}_{n+1} \\ \tilde{\eta}^{\,p}_{n+1} &= \eta^p_n - \sqrt{\frac{2}{3}}\Delta\tilde{\lambda}_{n+1}\partial_\theta\left(\tilde{\sigma}_{y,n+1} + \beta_{n+1}(\tilde{\bar{e}}^{\,p}_{n+1})\right) \end{aligned}$$

4. Compute plastic power:

$$\tilde{\mathcal{D}}^{n+1}_{mech} = \chi\sqrt{\frac{2}{3}}\left(\tilde{\sigma}_y + \tilde{\beta}\right)_{n+1}\frac{\Delta\tilde{\lambda}_{n+1}}{\Delta t}$$

The definition of the variables that appear in this box are explained in appendices B and C.

Box 4: IMPL-EX explicit integration flowchart for thermo-elastoplastic models.

discretization the response in obtained by solving a sequence of linearized problems. The theories underlying the spatial and temporal discretization are presented in the section 4 and in section 6. The linearization of the weak form of the momentum and energy equation are not addressed in this work. We refer the reader to [8, 7] for further details.

In the appendix C.2 the expressions for the algorithmic tangent moduli for the implicit integration scheme as well as the IMPL-EX scheme are provided. The algorithmic constitutive tensor is a a key aspect in the linearization of the weak form of the momentum equation. In addition, in appendix C.3 we provide a linearization of the plastic power relevant in the linearization of the weak form of the energy equation.

6 Time integration of the IBVP

The Finite Element Method allows different time discretization schemes. The most common are the implicit and explicit time integration schemes. Each of them has its advantages or disadvantages, see appendix D.

The implicit time integration scheme using isothermal split will be used in this work. Based on the global operator split for finite deformation plasticity presented in equations (3) and (4), a formal split of the problem into a mechanical phase with the temperature held constant, followed by a thermal phase at a fixed configuration is presented in the following lines.

The implicit coupled algorithm for a simultaneous solution of the thermo-mechanical equations is presented in appendix D.1.

6.1 Isothermal split

The following lines present a summary of the isothermal split, developed in [79]. Let $t_n \to t_{n+1}$ be the initial and final time step. Let $\Delta t = t_{n+1} - t_n$ be the time increment.

The algorithm in Box (5) is based on the application of an implicit backward-Euler difference scheme to the momentum equation, for fixed initial temperature (temperature at previous time step) and the application of an implicit backward-Euler difference scheme to the energy equation at a fixed configuration (configuration obtained as a solution of the mechanical problem).

The solution of the balance of momentum equation for fixed initial temperature gives an update of the primary variables $\mathbf{u}^*_{n+1}$, $\mathbf{p}^*_{n+1}$ and a first update of the internal variables (left Cauchy-Green tensor, internal energy and entropy) of the form

$$\mathbf{b}^e_n, \bar{\mathbf{e}}^{\,p}_n, \eta^p_n \quad \to \quad \text{(Box 3)} \quad \to \quad \tilde{\mathbf{b}}^e_n, \tilde{\bar{e}}_{n+1}, \tilde{\eta}^{\,p}_n \tag{36}$$

Along with an incremental value of the consistency parameter satisfying the *Kuhn-Tucker* conditions and denoted by $\Delta\tilde{\lambda}_{n+1}$

The solution of the balance of energy with initial conditions $\mathbf{u}^*_{n+1}, \mathbf{p}^*_{n+1}, \theta^*_n$ and initial internal variables $\mathbf{b}^e_n, \bar{\mathbf{e}}^{\,p}_n, \eta^p_n$ gives an update of the primary variable θ^*_{n+1} and a second update of the internal plastic variables (at fixed configuration) of the form

COUPLED SYSTEM OF EQUATIONS
ISOTHERMAL SPLIT

1. Momentum equation for fixed initial temperature (3)

$$\mathbf{F}_{\mathbf{u},dyn}(\ddot{\mathbf{u}}^*_{n+1}) = \mathbf{F}_{\mathbf{u},int}\left(\boldsymbol{\sigma}_{n+1}(\mathbf{u}^*_{n+1}, \mathbf{p}^*_{n+1}, \theta^*_n; \lambda_{n+1}(\mathbf{u}^*_{n+1}, \theta^*_n))\right) - \mathbf{F}_{\mathbf{u},ext}(\mathbf{u}^*_{n+1})$$

2. Incompressibility

$$\left(\mathbf{M}^{\mathbf{p}} + \mathbf{M}^{stab}\right)\mathbf{p}^*_{n+1} = \mathbf{F}_{p,vol}(J^*_{n+1}(\mathbf{u}^*_{n+1}, \theta^*_n))$$

where $\mathbf{M}^{\mathbf{p}}$ and $\mathbf{M}^{stab}$ are the mass-type matrices of the linearized pressure and stabilization forces respectively

3. Update nodal variables

$$\begin{aligned} \mathbf{v}_{n+1} &= \mathbf{v}_n + \dot{\mathbf{v}}_{n+1}\Delta t \\ \mathbf{u}^*_{n+1} &= \mathbf{u}^*_n + \mathbf{v}_{n+1}\Delta t \\ \mathbf{p}^*_{n+1} &= \mathbf{p}^*_n + \Delta\mathbf{p}^*_{n+1} \end{aligned}$$

---

4. Energy equation at updated fixed configuration (4)

$$\mathbf{F}_{\theta,dyn}(\dot{\theta}^*_{n+1}) = \mathbf{F}_{\theta,int}(q(\theta^*_{n+1}); \mathcal{D}^*_{int}(\mathbf{u}^*_{n+1}, \theta^*_{n+1}); \lambda_{n+1}(\mathbf{u}^*_{n+1}, \theta^*_{n+1})) - \mathbf{F}_{\theta,ext}$$

5. Update nodal variables

$$\theta^*_{n+1} = \theta^*_n + \dot{\theta}^*_{n+1}\Delta t$$

The definition of the variables that appear in this box are explained in sections 4 and 6.

Box 5: Implicit isothermal split scheme.

$$\mathbf{b}^e_n, \bar{\mathbf{e}}^{\,p}_n, \eta^p_n \;\rightarrow\; \text{(Box 3)} \;\rightarrow\; \tilde{\tilde{\mathbf{b}}}^e_{n+1}, \tilde{\tilde{e}}^p_{n+1}, \tilde{\tilde{\eta}}^p_{n+1} \tag{37}$$

Along with an incremental value of the consistency parameter satisfying the *Kuhn-Tucker* conditions and denoted by $\Delta\tilde{\tilde{\lambda}}_{n+1}$. In general, $\Delta\tilde{\lambda}_{n+1} \neq \Delta\tilde{\tilde{\lambda}}_{n+1}$ as a consequence $\tilde{\mathbf{b}}^e_n, \tilde{\bar{e}}^p_n, \tilde{\eta^{\prime}}^p_n \neq \tilde{\tilde{\mathbf{b}}}^e_{n+1}, \tilde{\tilde{e}}^p_{n+1}, \tilde{\tilde{\eta}}^p_{n+1}$

In summary, the isothermal split solves the mechanical problem with a predicted value of temperature equal to the temperature of the last converged time step and, then, solves the thermal problem using the configuration obtained as a solution of the mechanical problem. A full Newton-Raphson scheme is used for the solution of the non-linear system; the necessary linearization of the constitutive law has been presented in appendix C.2. The details of the linearization of the weak form of the momentum and energy equation can be seen in [8, 7].

The well-known restriction to conditional stability is the crucial limitation of the isothermal approach, which often becomes critical for strongly coupled problems. However, this restriction is not significant for metal plasticity [79]. *Armero and Simo* [1] provide the sufficient conditions for stability of the isothermal split as:

$$\frac{\Delta t}{h} \leq K^2 \frac{\sqrt{\rho c}}{\alpha} \Leftrightarrow \frac{\Delta t}{h} \leq K^2 \frac{\sqrt{2\,\mu c}}{\alpha} \sqrt{\frac{\rho}{(\lambda + 2\mu)}} \tag{38}$$

where $\lambda, \mu > 0$ are the Lamé constants, α the thermal expansion coefficient, ρ, c the density and the specific heat, and $h, \Delta t, K$ are the minimum element size of the mesh, the maximum allowed time step, and a given constant. In the cases where the mechanical inertia can be considered negligible, *Armero and Simo* [1] provide the sufficient conditions for stability of the isothermal split as:

$$\frac{\Delta t}{h^2} \geq \frac{\alpha^2 - 2\,E\,c}{2\,E\,k} \leftrightarrow \frac{\Delta t}{h^2} \geq \frac{c}{2\,k}\left(\frac{\alpha^2}{E\,c} - 2\right) \tag{39}$$

Previous restrictions show that algorithms based on the isothermal split are not suitable for strongly coupled problems, since the stability restriction phrased in terms of the Courant number becomes increasingly restrictive the higher the coupling (increase in the thermal expansion coefficient). The numerical simulation of metal cutting and metal forming processes can be considered a weakly coupled problem (the thermal expansion coefficient of metals is usually small), as a result, the isothermal split will perform well in most of the numerical simulations of cutting and forming processes for metal presented in this work. The stability restriction of the isothermal split is circumvented using an isentropic split, in which one must solve first a mechanical problem at constant entropy (estimates the temperature change in the mechanical problem), followed by a thermal heat conduction problem at constant (fixed) configuration [1].

6.2 Isothermal IMPL-EX split

The isothermal scheme presented in [79] decouples the thermo-mechanical problem in two more simple problems, but, yet, the mechanical problem is coupled with the

COUPLED SYSTEM OF EQUATIONS
IMPL-EX SPLIT

1. Momentum equation for fixed initial temperature (3)
(elastic problem with shear modulus changing from element to element)

$$\mathbf{F}_{\mathbf{u},dyn}(\ddot{\mathbf{u}}^{**}_{n+1}) = \mathbf{F}_{\mathbf{u},int}\left(\boldsymbol{\sigma}_{n+1}(\mathbf{u}^{**}_{n+1}, \mathbf{p}^{**}_{n+1}, \theta^{**}_{n}; \lambda_{n+1}(\mathbf{u}^{**}_{n+1}, \theta^{**}_{n}))\right) - \mathbf{F}_{\mathbf{u},ext}(\mathbf{u}^{**}_{n+1})$$

2. Incompressibility

$$\left(\mathbf{M}^{\mathbf{p}} + \mathbf{M}^{stab}\right)\mathbf{p}^{**}_{n+1} = \mathbf{F}_{p,vol}(J^{**}_{n+1}(\mathbf{u}^{**}_{n+1}, \theta^{**}_{n}))$$

where $\mathbf{M}^{\mathbf{p}}$ and $\mathbf{M}^{stab}$ are the mass-type matrices of the linearized pressure and stabilization forces respectively

3. Update nodal variables

$$\begin{aligned}
\mathbf{v}_{n+1} &= \mathbf{v}_n + \dot{\mathbf{v}}_{n+1}\Delta t \\
\mathbf{u}^{**}_{n+1} &= \mathbf{u}^{**}_n + \mathbf{v}_{n+1}\Delta t \\
\mathbf{p}^{**}_{n+1} &= \mathbf{p}^{**}_n + \Delta\mathbf{p}^{**}_{n+1}
\end{aligned}$$

---

4. Energy equation at updated fixed configuration (4)
(thermal problem with temperature dependent external heat source)

$$\mathbf{F}_{\theta,dyn}(\dot{\theta}^{**}) = \mathbf{F}_{\theta,int}(q(\theta^{**}_{n+1}); \mathcal{D}^{**}_{int}(\mathbf{u}^{**}_{n+1}, \theta^{**}_{n+1}); \lambda_{n+1}(\mathbf{u}^{**}_{n+1}, \theta^{**}_{n+1})) - \mathbf{F}_{\theta,ext}$$

5. Update nodal variables

$$\theta^{**}_{n+1} = \theta^{**}_n + \dot{\theta}^{**}_{n+1}\Delta t$$

6. Constitutive equation and update internal variables (Plastic algorithm)

$$\tilde{\tilde{\mathbf{b}}}^{e}_{n+1}, \tilde{\tilde{\bar{e}}}_{n+1}, \tilde{\tilde{\eta}}^{p}_{n+1} = f\left((\mathbf{u}^{**}_{n+1}, \theta^{**}_{n}), (\mathbf{b}^{e}_{n+1}, \bar{\mathbf{e}}_{n+1}, \eta_{n+1})\right)$$

The definition of the variables that appear in this box
are explained in sections 4 and 6.

Box 6: Isothermal IMPL-EX split.

evolution equations of the internal variables and the thermal problem is also coupled with the evolution equations of the internal variables, both of them are coupled through the plastic multiplier. The above reason, suggests decoupling the problem in the following three simple problems: (i) an elastic problem with shear modulus changing from element to element, (ii) a thermal problem with a temperature dependent plastic heat source and (iii) a relaxation process affecting the stress and the internal variables at the integration points.

In this work, we present a new staggered algorithm, which is based on the isothermal split presented in [79] and the IMPL-EX integration scheme of the constitutive equations presented in [53]. Using the ingredients presented above, the solution of the coupled system of ODE (16), (14) and (15) could be decoupled in the three simple problems mentioned previously. In addition, the elastic and the thermal problems update the internal variables according to a predicted plastic multiplier (explicit), while the constitutive equations keep the displacements, velocities and temperatures unchanged (implicit).

For simplicity, a partition of the time domain $I := [0, T]$ into N time steps, of the same length Δt is considered. Let us focus on the time step $t_n \to t_{n+1}$, where $\Delta t = t_{n+1} - t_n$. An implicit backward-Euler difference scheme is applied to the momentum equation and to the energy equation. In the first step the extrapolation of the plastic multiplier $\Delta\lambda_{n+1} = \Delta\lambda_n$ is done. Consequently, the stresses $\boldsymbol{\sigma}_{n+1}$ are computed via in IMPL-EX integration scheme of the constitutive equation. After that, the balance of momentum (43) is solved implicitly providing the nodal displacement and pressure for fixed initial temperature. The balance of momentum equations, providing a fixed initial temperature and an extrapolated value of the internal variables, constitutes a non-linear system to solve. In this case, the non-linearity of the system appears due to the geometrical part of the linearized equations. Therefore they have to be iteratively solved until convergence is achieved.

The solution of the balance of momentum equation for a fixed initial temperature gives an update of the primary variables $\mathbf{u}^{**}_{n+1}, \mathbf{p}^{**}_{n+1}$ and a first update of the internal variables of the form

$$\mathbf{b}^e_n, \bar{\mathbf{e}}^{\,p}_n, \eta^p_n \;\; \to \;\; \text{(Box 4)} \;\; \to \;\; \tilde{\mathbf{b}}^e_n, \tilde{\bar{e}}^p_{n+1}, \tilde{\eta}^{\,p}_n \tag{40}$$

Then, in the second step, the solution of the balance of energy with initial conditions $\mathbf{u}^{**}_{n+1}, \mathbf{p}^{**}_{n+1}, \theta^{**}_n$, initial internal variables $\mathbf{b}^e_n, \bar{\mathbf{e}}^{\,p}_n, \eta^p_n$ and the extrapolation of the plastic multiplier $\Delta\lambda_{n+1} = \Delta\lambda_n$ gives an update of the primary variable θ^{**}_{n+1} and a second update of the internal plastic variables (at fixed configuration) of the form

$$\mathbf{b}^e_n, \bar{\mathbf{e}}^{\,p}_n, \eta^p_n \;\; \to \;\; \text{(Box 4)} \;\; \to \;\; \tilde{\tilde{\mathbf{b}}}^e_{n+1}, \tilde{\tilde{\bar{e}}}^p_{n+1}, \tilde{\tilde{\eta}}^p_{n+1} \tag{41}$$

Finally, in the third step, the values of $\mathbf{u}^{**}_{n+1}, \mathbf{p}^{**}_{n+1}, \theta^{**}_n$ remain fixed, and an implicit backward-Euler integration of the constitutive model (132) is done using as initial internal variables $\mathbf{b}^e_n, \bar{\mathbf{e}}^{\,p}_n, \eta^p_n$. Given, as a consequence a finally update of the internal variables of the form

$$\mathbf{b}^e_n, \bar{\mathbf{e}}^{\,p}_n, \eta^p_n \;\rightarrow\; \text{(Box 3)} \;\rightarrow\; \tilde{\tilde{\mathbf{b}}}^e_{n+1}, \tilde{\tilde{\bar{e}}}^p_{n+1}, \tilde{\tilde{\eta}}^p_{n+1} \tag{42}$$

The set of internal variables obtained at the end of this time step, will be the set of internal variables used as the starting point in the next step of the fractional step method proposed in this work. As summary about the isothermal IMPL-EX split is shown in Box 6.

It is interesting to note that the boundary values of the momentum equation are included in the elastic equations with shear modulus changing from element to element and the boundary values of the balance of energy are imposed on the thermal problem with temperature dependent plastic heat source. In addition, the plastic algorithm consists on a collection of systems of ordinary differential equations, each one of which belongs to a different integration point. A full Newton-Raphson scheme is used for the solution of the non-linear system.

7 Examples

This section we present some 2D examples using the proposed formulation. First of all, two benchmarks, the Cook's Membrane and the Taylor impact test. With the solutions reported in the literature we validate qualitatively and quantitatively the pressure stabilization in quasi-incompressible elastic problems and in mechanical problems involving plasticity. Furthermore, a plane strain traction test is presented to validate the locking free element type proposed for thermo-mechanical problems. In the traction test example, we also report the comparison of different time integration schemes, showing the advantages and disadvantages of the IMPL-EX solution scheme. Finally, the proposed formulation is used in the numerical simulation of a continuous steel cutting test in order to show the possibilities of the PFEM in the modelling of metal cutting and metal forming processes.

7.1 Plane strain Cook's Membrane problem

The Cook Membrane problem is a bending dominated example that has been used by many authors as a reference test to check their element formulation. Here it will be used to validate the proposed formulation in incompressible elasticity and plasticity. The results of our formulation will be compared against Q1P0 finite element and a mixed finite element using Orthogonal Subgrid Scale as a stabilization strategy. The problem consists in a tapered panel, clamped on one side and subjected to a shearing load at the free end, see figure (3). In order to test the convergence behavior of different formulations, the problem has been discretized into 16×16, 24×24 and 40×40 elements per side. The following materials properties are assumed: Young's Modulus $E = 70\,\frac{UF}{UL^2}$, Poisson's ratio $\nu = 0.4999$ and applied force $F = 1\,UF$. Where UF means Units of Force and UL means Units of Length.

Figure (4) shows the behavior of both quadrilateral and triangular finite elements in case of nearly incompressible elasticity. The figure shows the poor performance of the

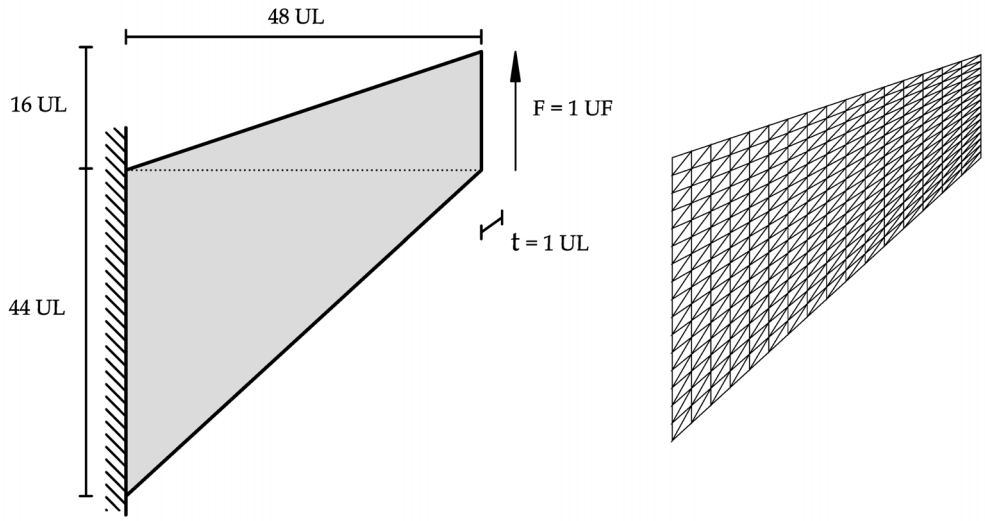

Figure 3: Cook's Membrane benchmark. Problem dimensions and the initial structured triangular mesh of 16x16 elements.

Q1 and T1 standard elements within the context of nearly incompressible elasticity, due to an extreme locking. Furthermore, the figure shows that the proposed formulation converges similarly to OSS but a low computational cost. It is important to remark that in Polynomial pressure projection (PPP) strategy the stabilization parameter is mesh size independent and that the stabilization terms added to the mixed formulation are elementary depend. It shows that our proposal allows getting similar results to the OSS strategy but a low computational cost. The stabilization parameter used in PPP and OSS was $\alpha = \tau = 1$.

Next examples involves Cook‘s Membrane but J2-plasticity and the following assumed materials properties: Young‘s Modulus $E = 70\,\frac{UF}{UL^2}$, Poisson‘s ratio $\nu = 0.4999$, yield stress $\sigma_y = 0.243\,\frac{UF}{UL^2}$, hardening modulus $H = 0.135\,\frac{UF}{UL^2}$ and kinematic hardening modulus $K = 0.015\,\frac{UF}{UL^2}$ and an applied force of $F = 1.8\,UF$ in 50 increments.

Figure(5) shows a comparison of the top corner displacement for the mixed finite element using OSS and PPP as stabilization strategies. It also shows that the convergence behavior of two formulations is really similar. As we say in case of elastic behavior, PPP is simple to implement and do not need an extra calculation like the projected pressure gradient in OSS.

Figure (6) presents pressure contour field at the end of the deformation process. A smooth contour field can be identified in both mixed formulations. At the same time, the predicted results are very similar quantitatively.

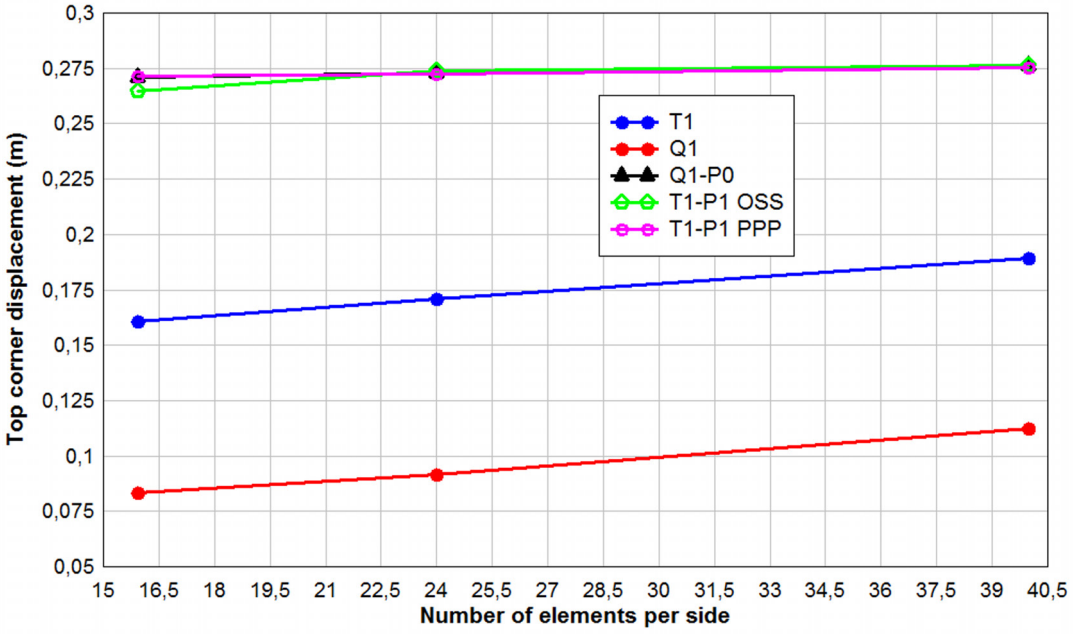

Figure 4: Plane strain Cook's Problem: convergence of different formulations for incompressible elasticity. T1 standard displacement for triangular elements, Q1 standard displacement for quadrilaterals elements, Q1P0 mixed mean dilatation/pressure approach for quadrilateral elements, T1P1 OSS mixed formulation for linear triangles using orthogonal sub grid scale as a stabilization strategy, T1P1 PPP mixed formulation for linear triangles using Polynomial pressure projection.

7.2 Taylor impact test

The problem consists of the impact of a cylindrical bar with initial velocity of 227 m/s into a rigid wall. The bar has an initial length of 32.4mm and an initial radius of 3.2 mm, see figure (7). Material properties of the bar are typical of copper: density $\rho = 8930\, kg/m^3$, Young's modulus $E = 1.17 \cdot 10^5 MPa$, Poisson's ratio $\nu = 0.35$, initial yield stress $\sigma_y = 400\, MPa$ and hardening modulus $H = 100\, MPa$. A period of 80 μs has been analyzed.

The problem is treated as a 2D axisymmetric model of the cylindrical bar shown in figure (7). We will compare qualitatively and quantitatively the results obtained using the proposed formulation with the results of the formulations based in the Characteristic Base Split(CBS) [71], the Average Nodal Pressure (ANP) [9], and the *De Micheli* formulation [26]. In this problem the effect of the temperature is not considered. The bar constitutive behaviour experience plasticity but not thermo-plasticity.

First we consider a Finite Element solution of the problem with the displacement-pressure stabilized element proposed in this work. The mesh is considered the same in the whole analysis and the PFEM features are not used. The final geometry of the

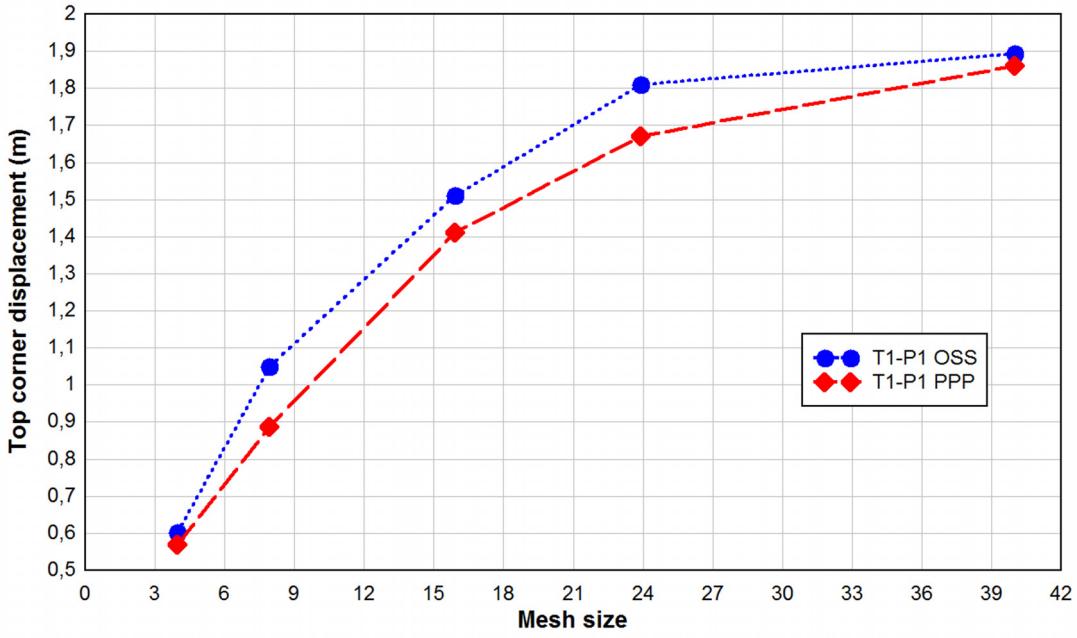

Figure 5: Plane strain Cook's Problem: convergence of different formulations for J2-Plasticity. T1P1 OSS mixed formulation for linear triangles using orthogonal sub grid scale as a stabilization strategy, T1P1 PPP mixed formulation for linear triangles using Polynomial pressure projection.

bar is in good agreement with the results obtained in the literature and any locking is not present in the solution. However some parts of the mesh gets very deformed, the elements that received first the impact experience large plastic deformations. That causes a pressure distribution somehow conditioned by the mesh shape. The final radius in the base of the bar obtained using the proposed formulation (PPP with FEM) is of $7.24\,mm$. Table 1 shows the comparison of the final radius obtained with present formulation with the results presented in the literature.

Table 1: Final radius of the rod after the Taylor Impact Test obtained with *De Micheli* formulation, CBS formulation, ANP formulation and the proposed formulation of this work.

Formulation	De Micheli[26]	CBS[71]	APN[9]	PPP (FEM)	PPP (PFEM)
Final Radius	7.07 mm	7.07 mm	6.99 mm	7.24 mm	7.02 mm

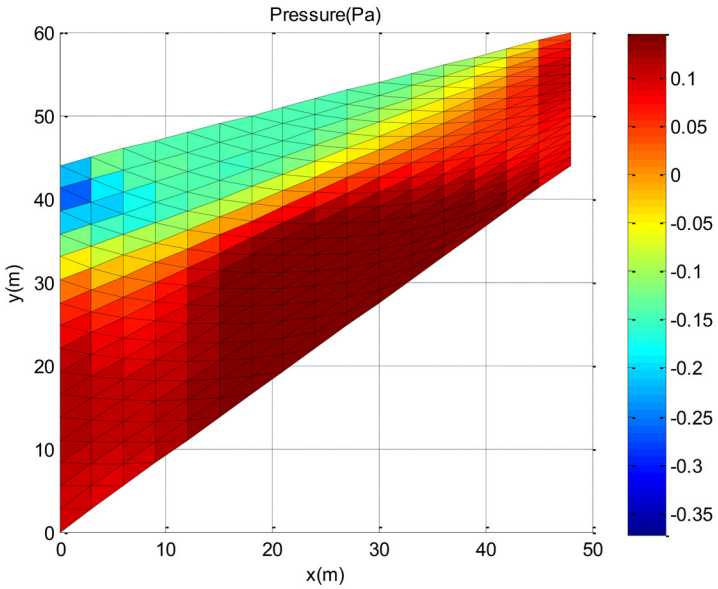

(a) Orthogonal Sub grid Scale c=1

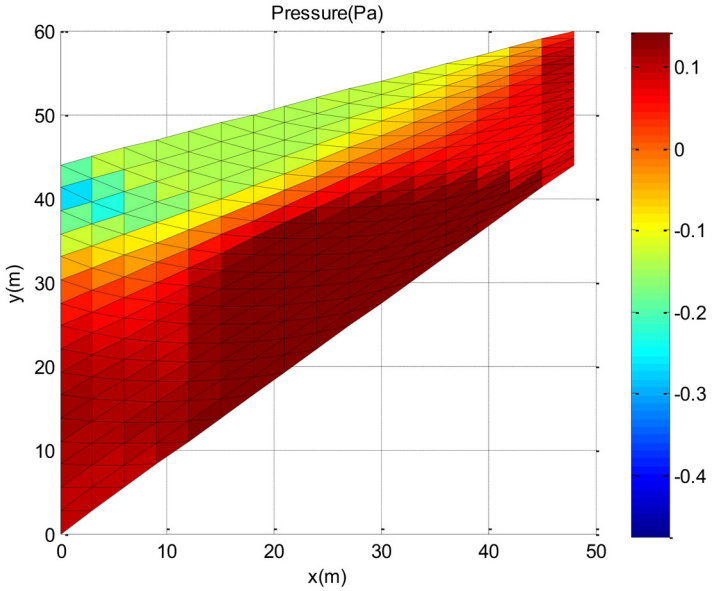

(b) Polynomial Pressure Projection c=1

Figure 6: Pressure field for mixed formulation using Orthogonal Sub Grid Scale and Polynomial Pressure Projection as stabilization strategies and J2-Plasticity.

Figure (8) shows the final mesh and the numerical results of the pressure and effective plastic strain distribution using the formulation proposed in this work.

In order to improve the solution the PFEM simulation with the intrinsic geometry

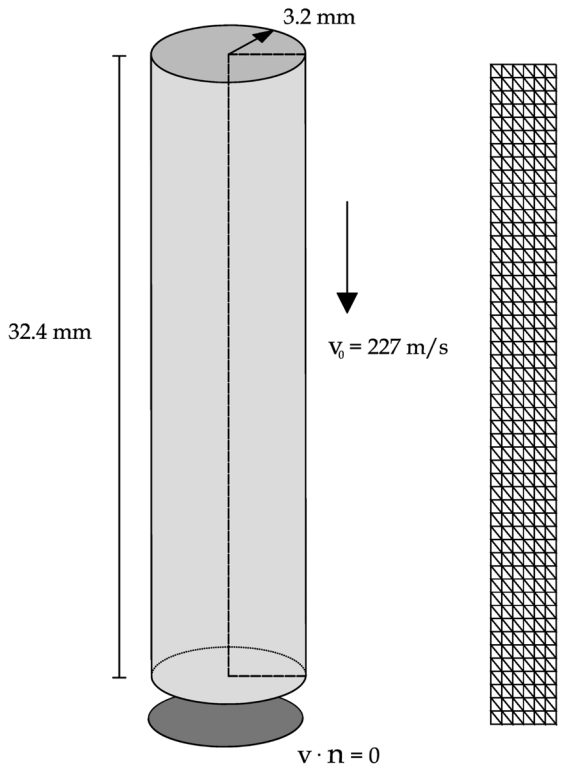

Figure 7: Taylor impact test. Problem dimensions and the initial structured triangular mesh of 6x50 elements.

update is used. In this case the finite elements of the mesh have always a good shape. It avoids the artificial numerical peaks that appear in the solution of the bad shaped linear triangles. The final geometry of the bar is in good agreement with the results obtained in the literature, without locking in the solution and with a final radius in the base of the bar of $7.02\,mm$ (PPP with PFEM). Figure (9) shows the final mesh and the numerical results of the pressure and effective plastic strain distribution using the PFEM formulation proposed in this work. The values for the equivalent plastic strain and pressure fields obtained with the PFEM coincide well with those given by FIC and by the CBS formulation.

7.3 Thermo-mechanical traction test

We consider a rectangular specimen in plane strain submitted to uniform traction forces. The specimen considered in the simulation has a width of $12.866\,mm$ and a length of $53.334\,mm$, see figure (10). Figure (10) shows also the mesh in the initial configuration. The bar is assumed insulated along its lateral face, while the temperature is held constant and equal to $293.15\,K$ on the upper and lower faces.

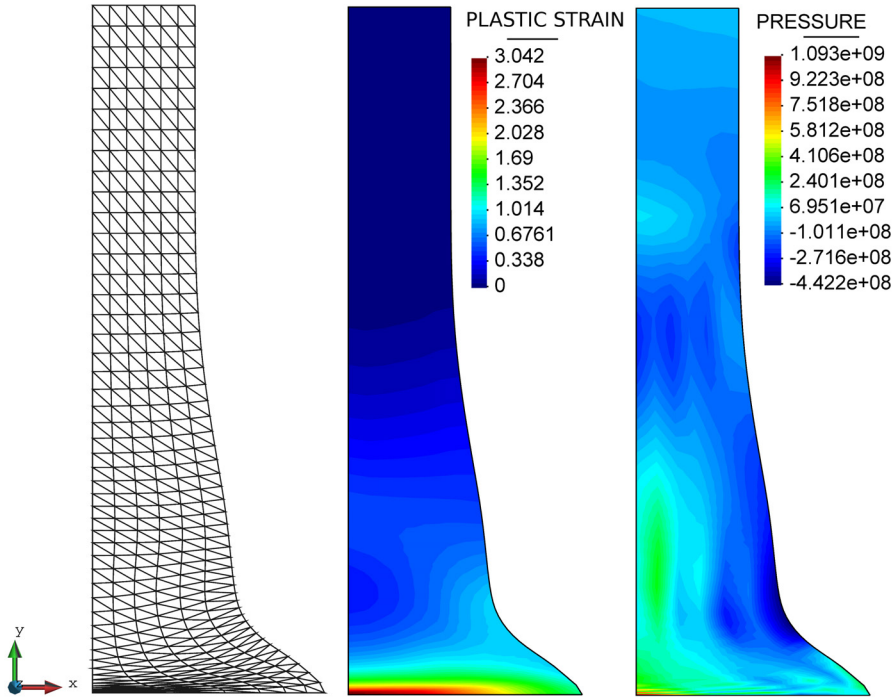

Figure 8: Final mesh, equivalent Plastic Strain distribution and Pressure field $80\mu s$ after the impact for the proposed formulation without geometry update.

The total value of imposed displacement is increased to $5\,mm$ applied in 100 equal time steps, with a rate of increase of $1\,mm/s$. The chosen values of thermo-mechanical properties of the specimen are given in Table 4 and Table 2, they correspond to steel. We consider the source term in the energy equation defined as a fraction of the plastic work, in this example we use a factor of 0.9. Due to the symmetry of the solution, only one quarter of the specimen is discretized, imposing the corresponding symmetry boundary conditions. To solve the problem we use the mixed linear displacement-linear pressure finite element presented in this work with the Polynomial Pressure Projection as a stabilization technique.

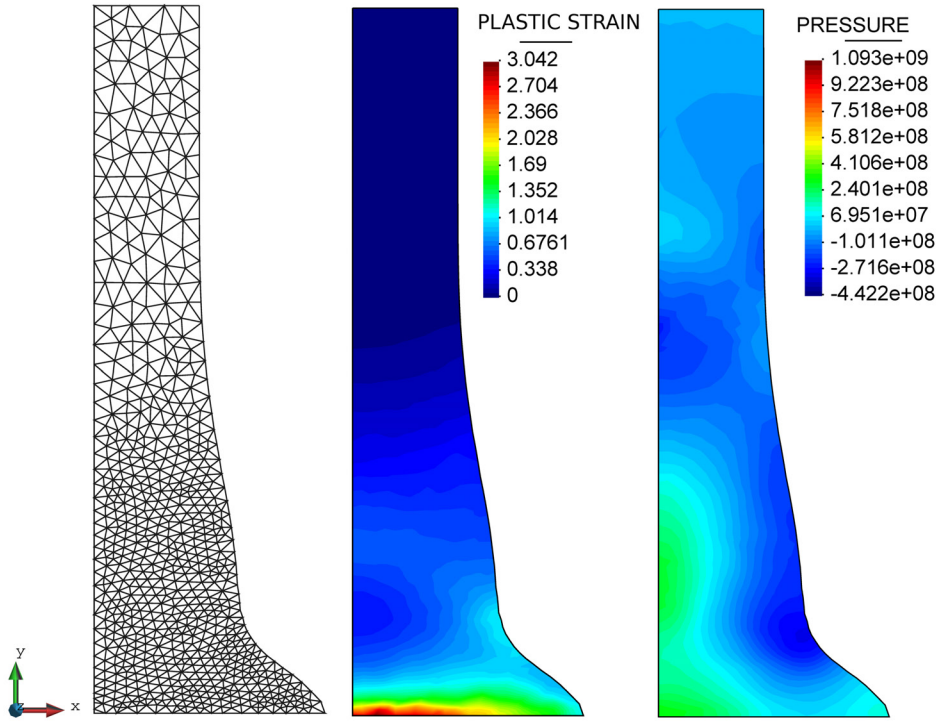

Figure 9: Final mesh, equivalent Plastic Strain distribution and Pressure field $80\mu s$ after the impact for the PFEM formulation.

Table 2: Material properties

Young Modulus	E	$206.9 \cdot 10^3$	MPa
Dissipation Factor	χ	0.9	
Thermal Capacity	c	$0.46 \cdot 10^9$	mm^2/s^2K
Density	ρ	$7.8 \cdot 10^{-9}$	Ns^2/mm^4
Expansion Coefficient	α	$1 \cdot 10^{-5}$	K^{-1}

The simulations are performed under quasi-static conditions with the isothermal implicit split proposed by *Simo* [4], presented in the section 6 and the isothermal IMPL-EX split proposed in this work. No specific features of the PFEM are used in this example. The purpose is to evaluate the thermo-hyperelastoplastic model and the stabilized element developed within the IMPL-EX integration scheme. Next some results are presented.

Figure(11) shows the temperature and von Mises field at the final configuration.

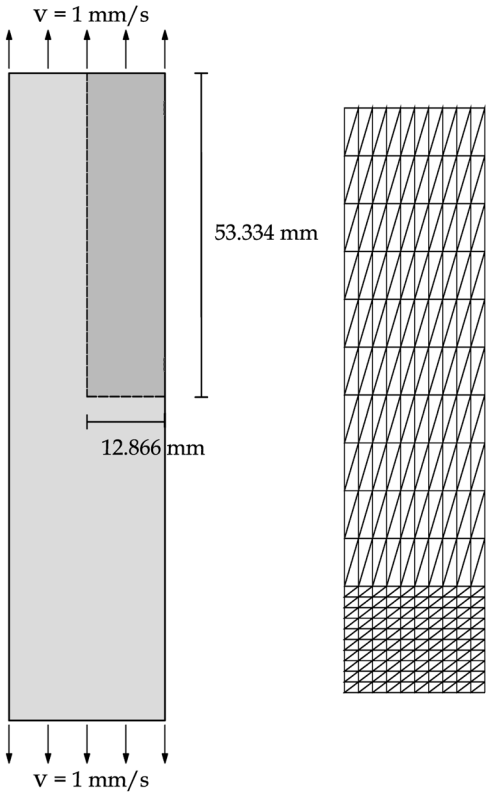

Figure 10: Plain strain nearly adiabatic shear banding traction test benchmark. Problem dimensions and initial mesh.

Figure (12) shows the load/displacement curve obtained with the proposed formulation. The same figure shows also the results presented by *Ibrahimbehovic and Chorfi* [41] using a four node element with incompatible modes and *Beni and Movahhedy* [82] using an Arbitrary Lagrangian Eulerian formulation. The predicted forces are similar during the strain hardening part of the force displacement curve, but in the softening branch of the force displacement curve the predicted forces are different in the three formulations. Our formulation predicts the force in the softening branch in a similar way as the results presented by *Ibrahimbehovic and Chorfi* do. It means that the formulation does not lock in softening.

The load displacement curve obtained using the isothermal IMPL-EX split proposed in this work is presented in Figure (13). The total value of imposed displacement is increased to $5\,mm$ and applied in 100-500-2000 equal time steps to analyze the overshoots and oscillations in the transitions from elastic to inelastic state. The results presented in Figure (13) show that the overshoot decreases by increasing the number of time steps used. Using 2000 time steps, the nonphysical overshot predict by the isothermal IMPL-EX split is negligible, although, the results predicted with 500

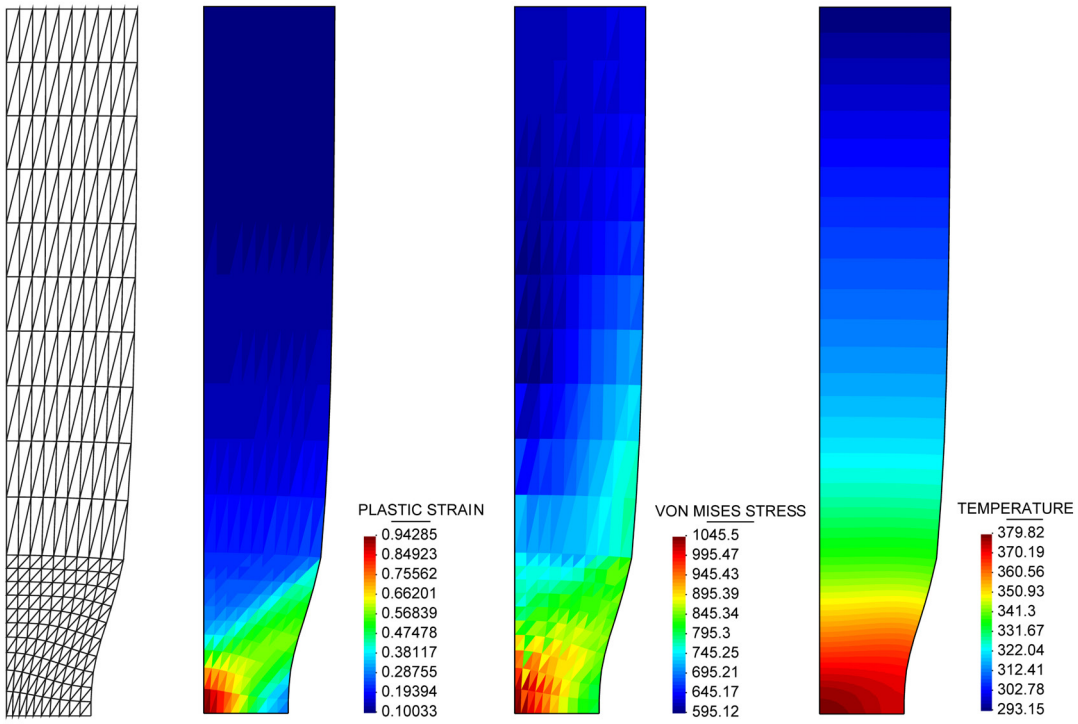

Figure 11: Plane strain nearly adiabatic shear banding. Temperature and von Mises stress field at 5 mm.

time steps can be considerable satisfactory, taking into account that we identify the overshoot as an nonphysical prediction that comes from the integration scheme. On practice the error on the norm of the stress can be used to predict the suitable time step for the IMPL-EX integration scheme.

The computing time need to solve the thermo-mechanical traction test using the isothermal IMPL-EX split is slightly smaller compared with the computing time needed by the isothermal implicit split. Considering that in both cases we are getting the same accuracy, the isothermal IMP-LEX split will be used in the numerical modeling of larger problems. In that problems the IMPL-EX is a substantially better choice, because it needs less computing time per time step in comparison with the implicit split and because it introduces robustness in the integration of the constitutive law.

7.4 Challenging thermo-mechanical problems

7.4.1 Steel cutting test

Here we introduce our first industrial application, it consists in the cutting of a rectangular block of a common steel. The block (workpiece) has a length $3.7\,mm$ and a of width $1.8\,mm$. The cutting has an imposed velocity of $3333.3\,mm/s$, a cutting depth

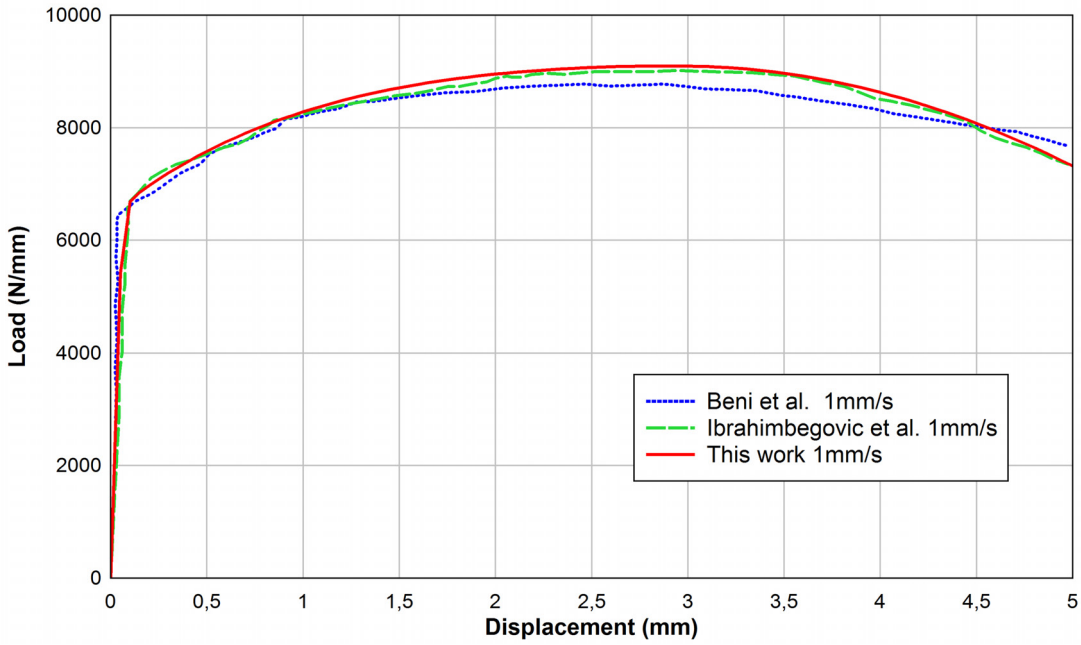

Figure 12: Plane strain nearly adiabatic shear banding. Load/Displacement curve, from different authors.

of $0.10\,mm$, a rake angle of $0\,^\circ$, a clearance angle of $5\,^\circ$ and a tool radius of $0.025\,mm$. The rigid tool is composed by to straight lines connected by a circular arch on the tool tip with the characteristics of the cutting parameters described, see (14). The workpiece material behavior is given by a *Simo* law that takes into account thermal softening (Table 4 and Table 2).

Conductivity and specific heat does not depend on temperature, we consider them constant. The following assumptions are made: First, the tool is supposed to be rigid and friction is neglected. Furthermore, the thermal exchange between the workpiece and the tool are also neglected. The inertia of the workpiece is neglected. A classical penalty method is considered for the contact constraint generated by the action of the rigid tool.

An implicit quasi-static step with the isothermal IMP-LEX split is used. Time steps were of $1.2 \cdot 10^{-8}$ which takes $2.5 \cdot 10^4$ steps for a tool to travel $1.0mm$. The assumption that the tool is rigid is reasonable, since the deformation of the tool is negligible compared with the deformation of the workpiece.

Temperature, pressure, effective plastic strain rate and von Mises contours are presented in Figures (16) and (17). Depicted pressure distribution shows the tension and compression zones. It is completed with the von Mises stress shown, which demonstrates that relatively high stresses arise in the primary shear zone and at the tool chip interface. The localization of this zone agrees with simplified models. It is also important to note the presence of residual stresses at and below the produced new

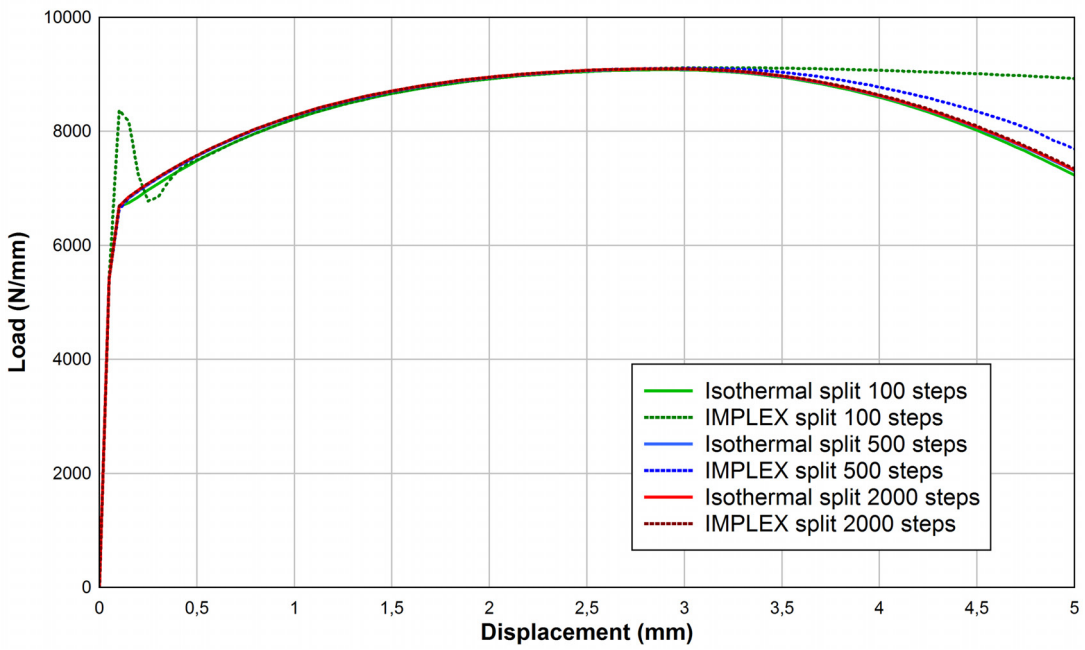

Figure 13: Plane strain nearly adiabatic shear banding. Load/Displacement curve.

surface and in the upper part of the chip, especially near the tool-chip interface where unloading due to curling of the chip occurred. The effective strain rate in the primary and the secondary shear zone is of the order of 10^5 and it has its highest value close to the tool tip. Finally, temperature distribution is also shown in the workpiece. Temperature reaches its peak on the tool tip zone located on the machined surface.

Figure (15) depicts the cutting and thrust forces applied on the tool, that are obtained from the simulation. Although the predicted chip is continuous, the cutting and thrust force does not reach a steady state due to the strong dependency of the yield hardening function on the linear hardening modulus. Figure (18) depicts the chip formation in different time step sequences and the contour fill of the temperature on the continuous chip.

The contact length between the tool and the workpiece, the deformed chip thickness and the shear angle are $0.16\,mm$, $0.25\,mm$ and $22\,^\circ$ respectively.

7.4.2 Analysis of the competitiveness of the PFEM

In order to validate PFEM as an effective strategy to deal with thermo-mechanical problems we present here a small comparison with other codes based in the FEM and with experimental results. The comparison is performed with a steel cutting test example similar to the one presented in this article. In this case the test is a model of the orthogonal cutting process proposed in [2].

The objective of this test is to predict the chip formation in the cutting process

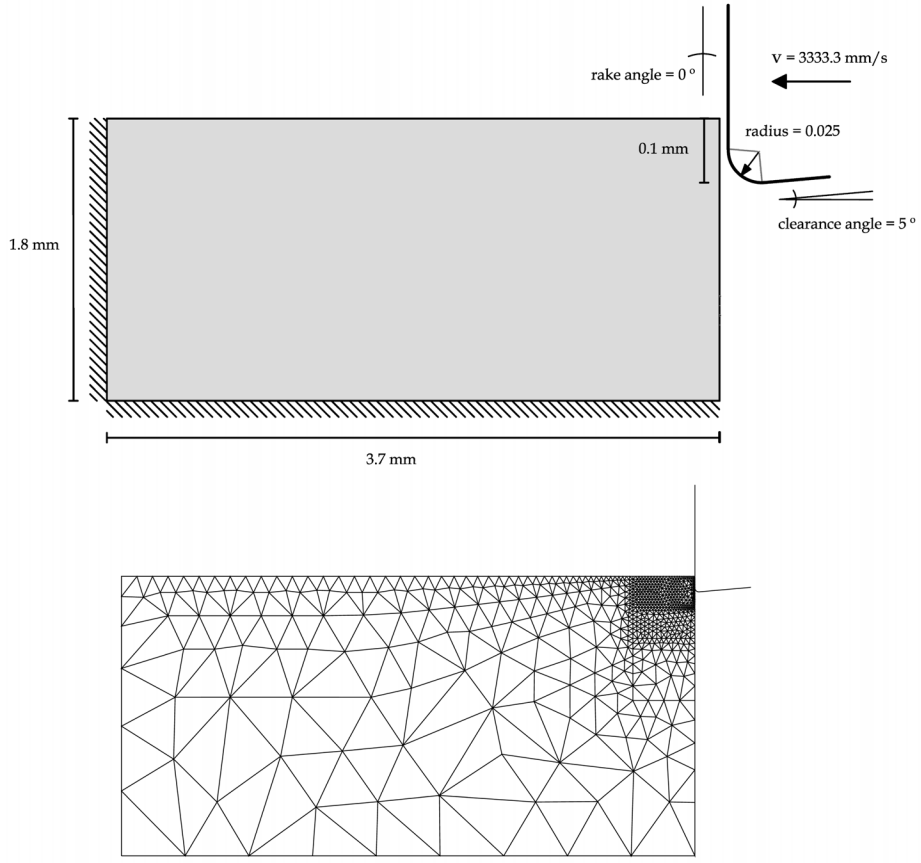

Figure 14: Steel cutting test. Workpiece, tool dimensions and initial unstructured triangular mesh.

of 42CD4 steel at 300 m/min, with a tool radius of 0.04 mm, rake angle of 6 and cutting depth 0.2 mm. Data about experimental results have been obtained from data reported in the literature, see [2].

The validation was carried out comparing numerical results with experimental ones and numerical results obtained from the commercial software Abaqus, Deform and AdvantEdge. It is important to mention that there are some differences and similarities between the formulations used in those softwares. They use distinct time integration schemes, boundary conditions, material models and contact laws. Main differences between the numerical models are listed next:

1. PFEM, Deform and Abaqus use a Johnson's Cook yield function to model the material behaviour. However in AdvantEdge the material behavior is governed by Marusich law.

2. Abaqus, AdvantEdge and Deform use a Coulomb friction law at the tool chip

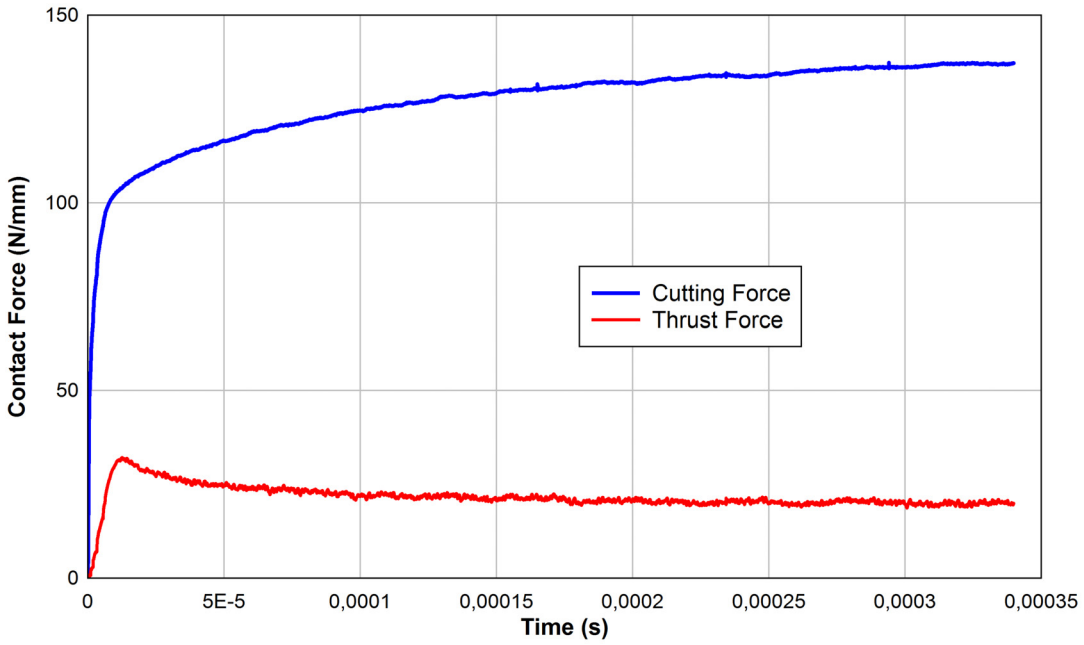

Figure 15: Cutting and thrust force vs. simulation time applied on the tool for a rate independent yield function.

interface, with a friction coefficient of 0.23. However PFEM and Deform use a Norton-Hoff friction law with a Norton Hoff constant value of 6e-5.

3. PFEM, Deform and AdvantEdge consider the tool as a deformable while Abaqus consider the tool as a rigid body.

Furthermore, PFEM, AdvantEdge and Deform use a Lagrangian description of motion while Abaqus uses an Arbitrary Lagrangian Eulerian description of motion. Also, PFEM and Deform use implicit time integration while AdvantEdge and Abaqus use explicit time integration. More information about the constitutive model, boundary conditions used in the numerical models developed in Abaqus and AdvantEdge are explained in detail in [2].

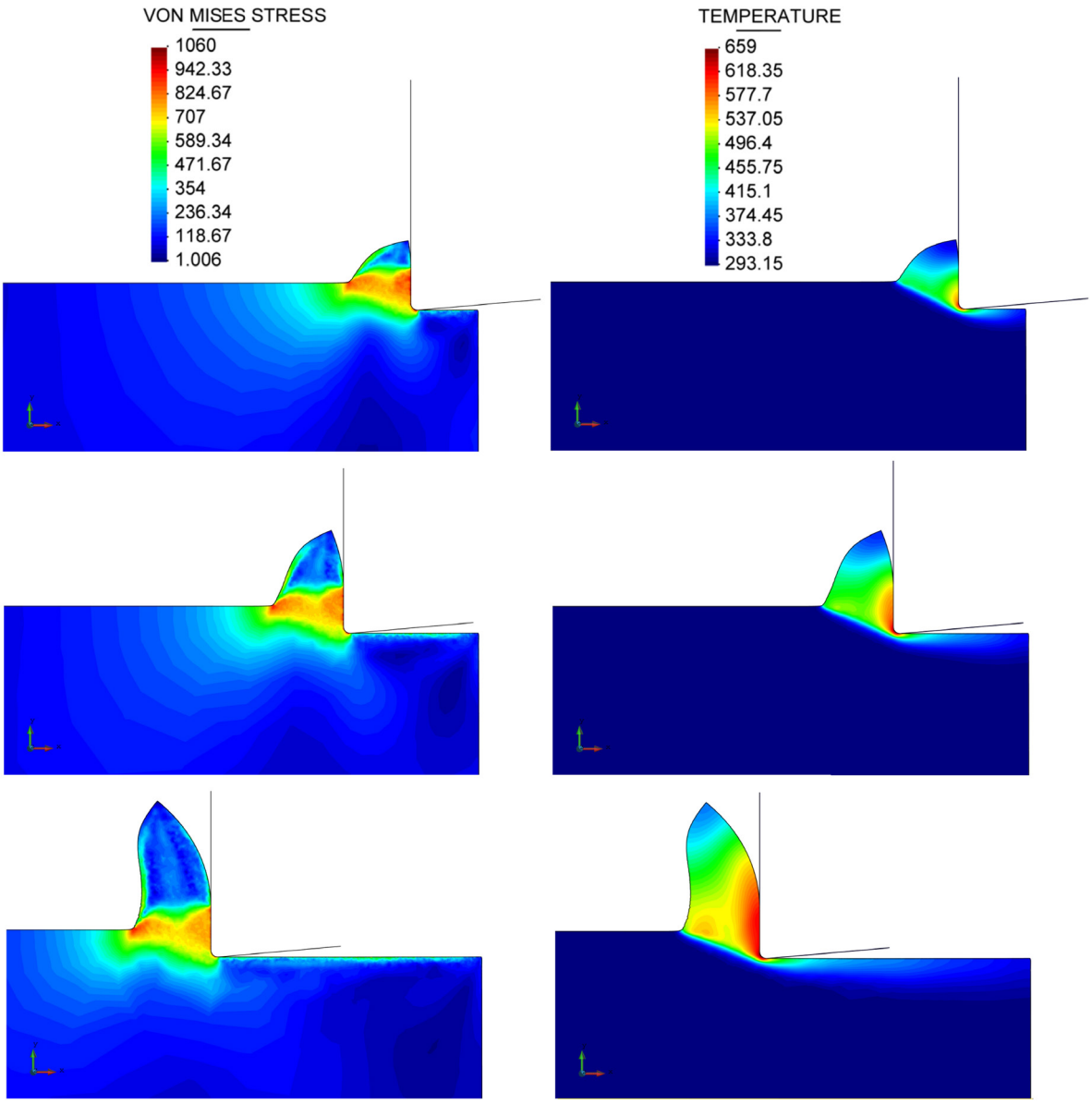

Figure 16: Continuous chip formation using a rate independent yield function: von Mises (MPa) and Temperature (K).

Table 3: Experimental and numerical results (PFEM, Abaqus, AdvantEdge, Deform)

	Temperature (K)	Chip thickness (mm)	Von Mises (MPa)	Contact force (N)	Contact length (mm)
Experimental	-	0.32	-	395	0.49
PFEM	1173	0.35	1400	383	0.26
Abaqus	1240	0.35	1348	412	0.32
AdvantEdge	1442	0.27	2343	647	0.29
Deform	1107	0.30	1210	365	0.24

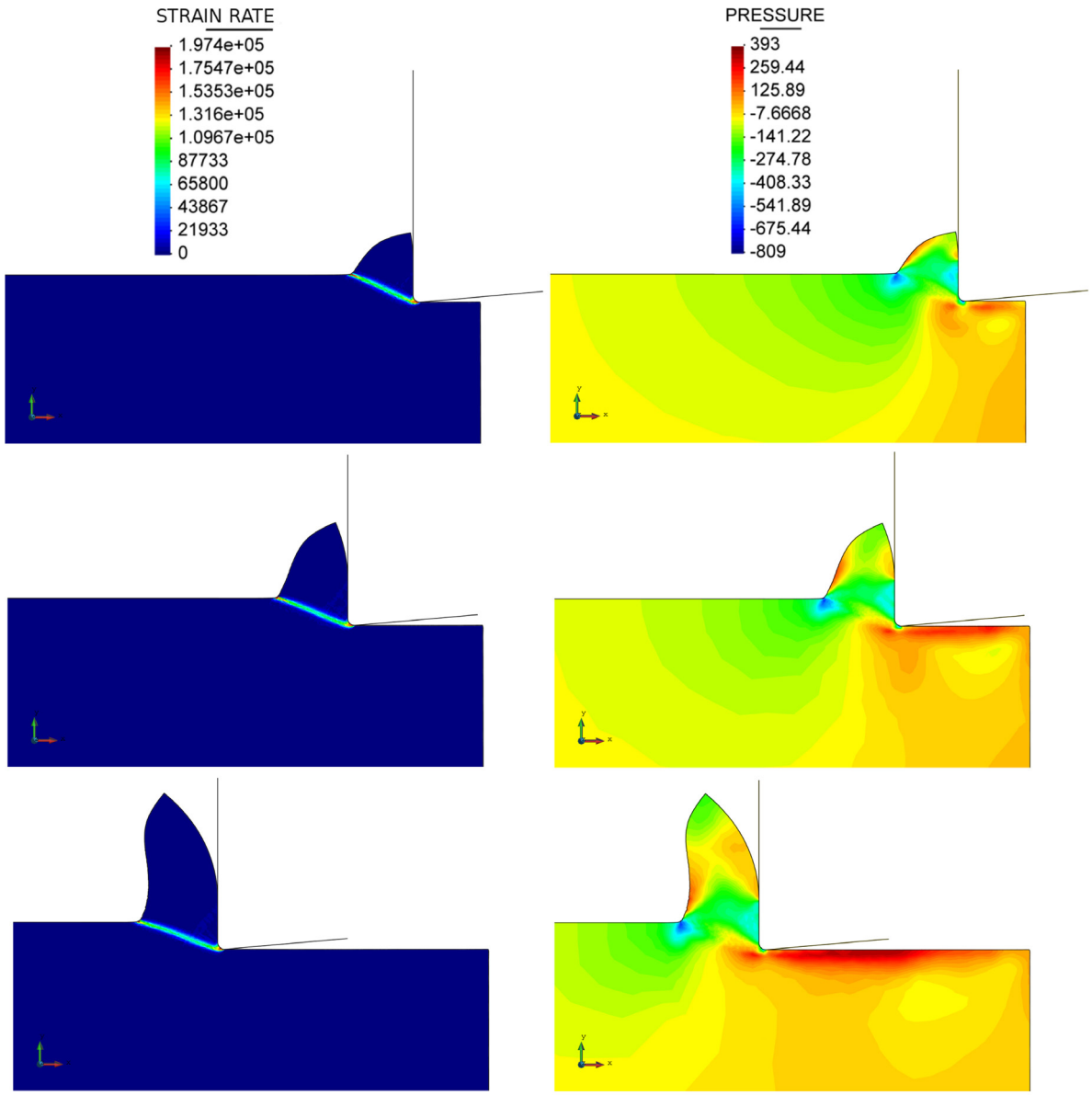

Figure 17: Continuous chip formation using a rate independent yield function: Strain rate (1/s) and Pressure(MPa).

Taking in account mentioned differences the results of the numerical simulation are presented in Table 3. The obtained process variables of temperature, chip thickness, contact length, von Mises stress and contact force are compared.

It is observed a good agreement between the experimental and numerical cutting forces predicted by the PFEM, Deform and Abaqus. Instead, comparing experimental

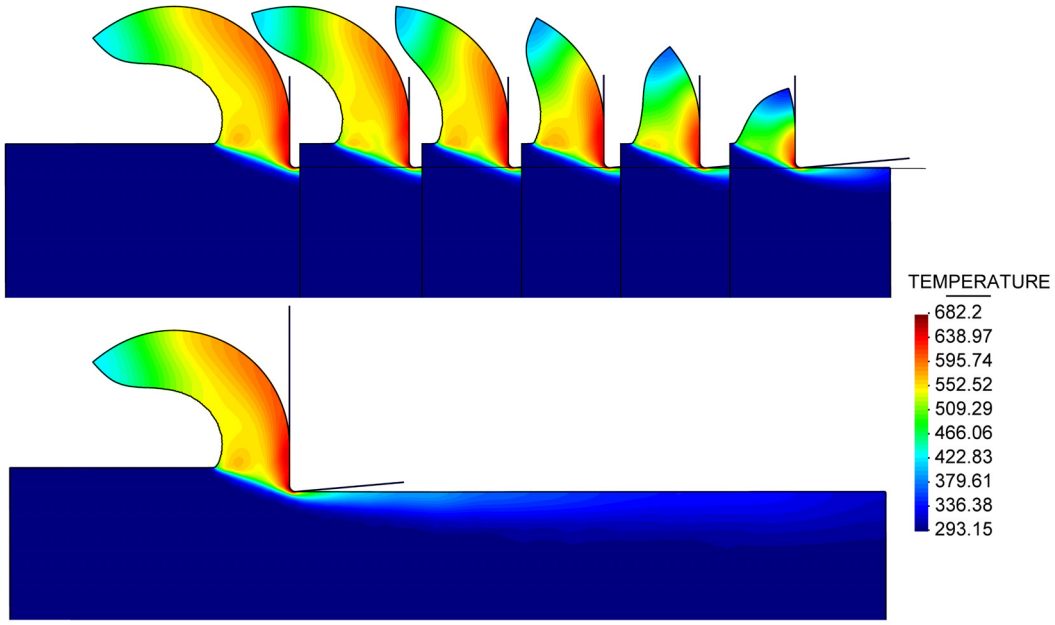

Figure 18: Continuous chip formation sequence: Temperature (K).

cutting forces with AdvantEdge results, higher differences were found. Regarding to the chip thickness a relatively quite good agreement was found for all the results. However, the tool-chip contact length measured in the experiments is about two times greater than the length predicted by the numerical simulations.

Comparing results for the maximum tool temperature it is observed that the larger difference occurs between Deform-AdvantEdge, while the smaller takes place between the PFEM and Deform. The differences are due to material model and friction law used in each one of the software (stated before).

In the case of the von Mises stress the results predicted by the PFEM, Deform and Abaqus are really similar, however the maximum von Mises stress predicted by Advantedge is 1000 MPa greater than the average stress predicted by the other software. The differences and similarities among the predicted results are because of those existing ones between the PFEM, Abaqus, Deform and AdvantEdge (stated before).

The numerical model set up with PFEM is considered to be accurate enough to compete with current comercial softwares based in the FEM method. Concerning with the computational cost, a MATLAB code with the PFEM implementation was used for this comparison. The calculation time in a serial execution was similar to the commercial ones. We guess that, with an implementation in a more optimized programming language, the PFEM would be clearly faster.

8 Conclusions

A numerical framework, based on the extension of the PFEM, for accurately and robustly simulating the different conditions exhibited by thermo-mechanical problems has been presented.

We show in examples 7.1 and 7.2 that the elastic and plastic incompressibility problem can be solved accurately with the proposed u-p formulation. This mixed nodal implementation adapts naturally to the core of PFEM since no additional transfer variables are required. It was observed that the stabilization parameter is mesh independent and that the convergence rate is similar to OSS technique but with lower computational cost.

In example 7.3 thermo-mechanical coupling, stabilization and IMPL-EX integration scheme were analyzed. The main conclusion is that IMPL-EX scheme increases the robustness compared with a typical implicit integration scheme and the continuous particle discretization of the domain allows us to control the mesh homogeneity.

The potential of numerical methods for the modelling of cutting problems is widely accepted by the industries of this field, the challenge being to promote effectively their industrial practice. In section 7.4 we have attempted to make an exploratory step in this regard by extending the model to simulate the main aspects of a typical continuous chip formation in 2D. The most relevant advantage of the formulation presented is the automatic update of the geometry and the natural generation of new boundary surfaces. It reduces the numerical diffusion due to re-meshing because transient mesh additivity is used instead of remeshing, and usually needs less degrees of freedom and less computing time than other methods to achieve the same accuracy. The results also show the good agreement between our method and the results obtained with other commercial codes.

This paper is an exploratory work, intending to evaluate the capabilities and possibilities of the PFEM in modelling thermo-mechanical problems, rather than being an attempt of comparison with other well established methods on the subject. In this sense, and for the sake of simplicity, all simulations in the paper are in 2D.

The extension of the method to 3D cases is a future research field not in the scope of this paper. It will possibly bring some new challenges, e.g.: a) facing the geometrical aspects to ensure mass conservation, b) construction of a constrained *Delaunay* tessellations and advanced $\alpha-$*shape* techniques in 3D, and c) evaluation of competitiveness aspects of the PFEM based methods with respect to alternative techniques in 3D cases.

Acknowledgement

The research leading to these results has received funding from the European Research Council under the European Union's Seventh Framework Programme (FP/2007-2013)/ERC Grant Agreement n. 320815, Advanced Grant Project COMP-DES-MAT.

A Coupled thermo-mechanical IBVP

A.1 Balance equations

The coupled thermo-mechanical initial boundary value problem (IBVP) is governed by the momentum and energy balance equations, restricted by the second law of thermodynamics. The material form of the local governing equations for the body $\boldsymbol{\varphi}(\mathbf{X}, t)$ can be written as

$$\begin{aligned} \dot{\boldsymbol{\varphi}}(\mathbf{X}, t) &= \mathbf{V}(\mathbf{X}, t) && (43)\\ \mathbf{DIV}\,(\mathbf{P}) + \mathbf{B} &= \rho_0 \dot{\mathbf{V}} && (44)\\ \dot{E} + \mathbf{DIV}\,(\mathbf{Q}) &= \bar{\mathcal{D}}_{int} + \mathcal{R} && (45) \end{aligned}$$

In the above equations ρ_0 is the reference density, $\mathbf{V}$ is the velocity field, $\mathbf{B}$ are the prescribed forces per unit of reference volume, $\mathbf{DIV}\,(\cdot)$ is the reference divergence operator, and $\mathbf{P}$ is the first Piola-Kirchhoff stress tensor. E is the internal energy per unit of material volume, $\mathbf{Q}$ the nominal heat flux, $\mathcal{R}$ is the prescribed reference heat source per unit of material volume and $\bar{\mathcal{D}}_{int}$ is the internal dissipation per unit of reference volume.

The entropy $\mathcal{N}$ and first Piola-Kirchhoff stress tensor $\mathbf{P}$ are formulated in terms of the free energy Ψ and subjected to the dissipation inequality often referred to as the Clausius Plank form of the second law of thermodynamics.

$$\begin{aligned} \bar{\mathcal{D}}_{int} &= \mathbf{P} : \dot{\mathbf{F}} + \theta\dot{\mathcal{N}} - \dot{E} \geq 0 && (46)\\ &= \mathbf{P} : \dot{\mathbf{F}} - \dot{\theta}\mathcal{N} - \dot{\Psi} \geq 0 && (47) \end{aligned}$$

where the free energy function per unit of material volume Ψ is obtained from the internal energy via the Legendre transformation

$$\Psi = E - \mathcal{N}\theta \tag{48}$$

The nominal heat flux $\mathbf{Q}$ is defined by Fourier's Law, subjected to the restriction on the dissipation by conduction $\bar{\mathcal{D}}_{con}$

$$\bar{\mathcal{D}}_{con} = -\frac{1}{\theta}\,\mathbf{GRAD}(\theta) \cdot \mathbf{Q} \geq 0 \tag{49}$$

The spatial form of the local governing equations for the body $\boldsymbol{\varphi}(\mathbf{x}, t)$ can be written analogously as

$$\begin{aligned} \dot{\boldsymbol{\varphi}}(\mathbf{X}, t) &= \mathbf{v}(\mathbf{x}, t) && (50)\\ \mathbf{div}\,(\boldsymbol{\sigma}) + \mathbf{b} &= \rho\dot{\mathbf{v}} && (51)\\ \dot{e} + \mathbf{div}\,(\mathbf{q}) &= \mathcal{D}_{int} + r && (52) \end{aligned}$$

In these equations, the motion $\dot{\boldsymbol{\varphi}}$ and the absolute temperature θ are regarded as the primary variables in the problem while $\mathbf{b}$ the body force per unit of spatial volume, e the internal energy per unit of spatial volume, and r the heat source per

unit of spatial volume are prescribed data. In addition, the heat flux $\mathbf{q}$, the entropy η as well as the Cauchy stress tensor $\boldsymbol{\sigma}$ are defined via constitutive equations.

These constitutive equations are subjected to the following restrictions on the internal dissipation and the dissipation arising from heat conduction per unite spatial volume

$$\mathcal{D}_{int} = J\boldsymbol{\sigma} : \mathbf{d} + \theta\,\dot{\boldsymbol{\eta}} - \dot{e} \geq 0 \tag{53}$$

$$\mathcal{D}_{con} = -\frac{1}{\theta}\,\mathbf{grad}(\theta) \cdot \mathbf{q} \geq 0 \tag{54}$$

where the free energy function per unit of spatial volume ψ is obtained from the internal energy via the Legendre transformation

$$\psi = e - \eta\,\theta \tag{55}$$

A.2 Boundary conditions and initial conditions

The basic governing equations (43) and (50) and the constitutive constraints (46) and (53) are completed by the standard boundary conditions for the mechanical field

$$\boldsymbol{\varphi} = \bar{\boldsymbol{\varphi}} \quad \text{on } \boldsymbol{\Gamma}_{\varphi} \tag{56}$$

$$\mathbf{t} = \mathbf{P} \cdot \mathbf{N} = \bar{\mathbf{t}} \quad \text{on } \boldsymbol{\Gamma}_{\sigma} \tag{57}$$

where $\bar{\boldsymbol{\varphi}}$ and $\bar{\mathbf{t}}$ are the prescribed deformation and nominal traction.

Together with the analogous essential and natural boundary conditions for the thermal field, namely,

$$\theta = \bar{\theta} \quad \text{on } \boldsymbol{\Gamma}_{\theta} \tag{58}$$

$$\mathbf{Q} \cdot \mathbf{N} = \bar{\mathbf{Q}} \quad \text{on } \boldsymbol{\Gamma}_{Q} \tag{59}$$

where $\bar{\theta}$ and $\bar{\mathbf{Q}}$ are the prescribed temperature and the normal heat flux maps.

Additionally, we assume that the following initial data is specified for the mechanical and thermal fields

$$\left.\begin{array}{l} \boldsymbol{\varphi}(\mathbf{X},t)\,|_{t=0} = \bar{\boldsymbol{\varphi}}_0(\mathbf{X}) \\ \mathbf{V}(\mathbf{X},t)\,|_{t=0} = \bar{\mathbf{V}}_0(\mathbf{X}) \\ \theta(\mathbf{X},t)\,|_{t=0} = \bar{\theta}_0(\mathbf{X}) \end{array}\right\} \text{in } \boldsymbol{\Omega} \tag{60}$$

A.3 Global operator split thermo-elastoplasticity

The IBVP described in equation (50) can be written in a simpler way. Suppose that

$$\dot{\mathbf{Z}} = \begin{bmatrix} \dot{\boldsymbol{\varphi}} \\ \rho\dot{\mathbf{v}} \\ \dot{\theta} \end{bmatrix} \quad \text{and} \quad \mathbf{Z} = \begin{bmatrix} \boldsymbol{\varphi} \\ \mathbf{v} \\ \theta \end{bmatrix} \tag{61}$$

Then equations can be written in a generalized form as

$$\dot{\mathbf{Z}} = \mathbf{A}(\mathbf{Z}) + \mathbf{f} \tag{62}$$

Where $\mathbf{A}$ is a nonlinear elliptic operator and $\mathbf{f}$ a prescribed function. The Cauchy stress tensor $\boldsymbol{\sigma}$, the heat flux vector $\mathbf{q}$, the total η and the plastic η^p entropies, and the mechanical dissipation $\mathcal{D}_{mech} := \mathcal{D}_{int}$ will be regarded as dependent variables in the problem, defined in terms of the primary variables $\mathbf{Z}$ and a set of internal strain-like variables $\boldsymbol{\Gamma}$. The set of internal variables are defined in terms of a constrained problem of evolution driven by the primary variables, with the functional form

$$\dot{\boldsymbol{\Gamma}} = \lambda\, \Pi(\boldsymbol{\Gamma}, \mathbf{Z}) \tag{63}$$

where λ is an additional variable determined by means of the *Kuhn-Tucker* conditions, as follows

$$\lambda \geq 0 \quad \Phi(\boldsymbol{\Gamma}, \mathbf{Z}) \leq 0 \quad \lambda\, \Phi(\boldsymbol{\Gamma}, \mathbf{Z}) = 0 \tag{64}$$

and $\Phi(\boldsymbol{\Gamma}, \mathbf{Z})$ is the *Mises* yield function. The *Kuhn-Tucker* conditions are applied only for rate independent plasticity models.

Generally, the nonlinear operator $\mathbf{A}$ can be decomposed in two simpler operators $\mathbf{A}_1$ and $\mathbf{A}_2$, where $\mathbf{A} = \mathbf{A}_1 + \mathbf{A}_2$ [79]. The use of the additive operator split applied to the coupled system of nonlinear ordinary differential equations leads to the following two simple problems:

1. Isothermal elastoplastic problem

$$\dot{\mathbf{Z}} = \begin{bmatrix} \dot{\boldsymbol{\varphi}} \\ \rho\dot{\mathbf{v}} \\ \dot{\theta} \end{bmatrix} = \begin{bmatrix} \mathbf{v}(\mathbf{x}, t) \\ \mathbf{div}\ (\boldsymbol{\sigma}(\boldsymbol{\varphi}, \theta, \lambda(\boldsymbol{\varphi}, \theta))) \\ 0 \end{bmatrix} + \begin{bmatrix} 0 \\ \mathbf{b} \\ 0 \end{bmatrix} \tag{65}$$

2. Thermoplastic problem at a fixed configuration

$$\dot{\mathbf{Z}} = \begin{bmatrix} \dot{\boldsymbol{\varphi}} \\ \rho\dot{\mathbf{v}} \\ \dot{\theta} \end{bmatrix} = \begin{bmatrix} 0 \\ 0 \\ -\mathbf{div}\ (\mathbf{q}(\boldsymbol{\varphi}, \theta, \lambda(\boldsymbol{\varphi}, \theta))) + \mathcal{D}_{int} \end{bmatrix} + \begin{bmatrix} 0 \\ 0 \\ r \end{bmatrix} \tag{66}$$

A.4 Weak form of the IBVP

We define the set of admissible displacements and admissible temperatures of the body domain Ω as the set of all sufficiently regular displacement and temperature functions that satisfy the essential boundary condition, denoted here respectively as

$$\mathbf{U} := \boldsymbol{\varphi}(\Omega) \to \mathbb{R}^3 \,:\, \det(\mathbf{F}) > 0 \quad \boldsymbol{\varphi}\,|_{\gamma_\varphi} = \bar{\boldsymbol{\varphi}} \tag{67}$$

$$\Theta := \theta(\Omega) \to \mathbb{R} \,:\, \theta > 0 \quad \theta\,|_{\gamma_\theta} = \bar{\theta} \tag{68}$$

The spatial version of the virtual work principle states that the body Ω is in equilibrium if, and only if, its Cauchy stress satisfies the equation. The weak form of the momentum balance equation

$$\mathbf{div}\,(\boldsymbol{\sigma}) + \mathbf{b} = \rho\dot{\mathbf{v}} \tag{69}$$

can be justified by taking the L_2 inner product of with any valued function $\boldsymbol{\eta} \in \mathrm{V}$, being V the space of virtual displacements

$$\mathrm{V} := \left\{\boldsymbol{\eta} \in \boldsymbol{\varphi}(\Omega) \to \mathbb{R}^3 \mid \boldsymbol{\eta}\,\big|_{\gamma_\varphi} = 0\right\} \tag{70}$$

and making use of the divergence theorem will lead to the following expression:

$$\int_{V_t} \left[\boldsymbol{\sigma} : \nabla^s\boldsymbol{\eta} - \boldsymbol{\eta}\,(\mathbf{b} - \rho\dot{\mathbf{v}})\right]\, dV_t - \int_{\gamma_\sigma} \mathbf{t}\cdot\boldsymbol{\eta}\, d\gamma_\sigma = 0 \quad \forall\boldsymbol{\eta} \in \mathrm{V} \tag{71}$$

The dynamic weak form of the energy balance equations on the body Ω (50) in absence of a heat source ($r = 0$)

$$\dot{e} + \mathbf{div}\,(\mathbf{q}) = \mathcal{D}_{int} \tag{72}$$

can be obtained by taking the L_2 inner product of with any valued function $\zeta \in \mathrm{T}$, being T the space of virtual temperatures

$$\mathrm{T} := \{\zeta \in \theta(\Omega) \to \mathbb{R} \mid \zeta\,|_{\gamma_\theta} = 0\} \tag{73}$$

making use of the divergence theorem, leading to the following expression:

$$\int_{V_t} \zeta(\dot{e})\, dV_t - \int_{V_t} \nabla\zeta\cdot\mathbf{q}\, dV_t - \int_{V_t} \zeta\mathcal{D}_{int}\, dV_t + \int_{\gamma_\mathbf{q}} \zeta(\mathbf{q}\cdot\mathbf{n})\, d\gamma_\mathbf{q} = 0 \quad \forall\zeta \in \mathrm{T} \tag{74}$$

For simplicity the L_2 inner product will be represented as $\langle\cdot,\cdot\rangle$, and with a slight abuse in notation $\langle\cdot,\cdot\rangle_{\gamma_\sigma}$ and $\langle\cdot,\cdot\rangle_{\gamma_\mathbf{q}}$ will denote the L_2 inner product on the boundaries γ_σ and $\gamma_\mathbf{q}$, respectively.

As a consequence, equations (70) and (74) can be written as

$$\langle\boldsymbol{\sigma}, \nabla^s\boldsymbol{\eta}\rangle - \langle\boldsymbol{\eta}, \mathbf{b} - \rho\dot{\mathbf{v}}\rangle - \langle\mathbf{t},\boldsymbol{\eta}\rangle_{\gamma_\sigma} = 0 \tag{75}$$

$$\langle\zeta, \dot{e}\rangle - \langle\nabla\zeta, \mathbf{q}\rangle - \langle\zeta, \mathcal{D}_{int}\rangle - \langle\zeta, \mathbf{q}\cdot\mathbf{n}\rangle_{\gamma_\mathbf{q}} = 0 \tag{76}$$

Denoting by $\mathbf{G}_{\mathbf{u},dyn}$ and $\mathbf{G}_{\mathbf{u},stat}$ the dynamic and quasi-static weak forms of the momentum balance equations lead to

$$\mathbf{G}_{\mathbf{u},dyn} = \mathbf{G}_{\mathbf{u},stat} + \langle\boldsymbol{\eta}, \rho\dot{\mathbf{v}}\rangle \tag{77}$$

$$\mathbf{G}_{\mathbf{u},stat} = \langle\boldsymbol{\sigma}, \nabla^s\boldsymbol{\eta}\rangle - \langle\boldsymbol{\eta}, \mathbf{b}\rangle - \langle\mathbf{t},\boldsymbol{\eta}\rangle_{\gamma_\sigma} \tag{78}$$

And denoting by $\mathbf{G}_{\theta,dyn}$ and $\mathbf{G}_{\theta,stat}$ the dynamic and quasi-static weak forms of the energy balance equations lead to

$$\mathbf{G}_{\theta,dyn} = \mathbf{G}_{\theta,stat} + \langle \zeta, \dot{e} \rangle \tag{79}$$
$$\mathbf{G}_{\theta,stat} = -\langle \nabla\zeta, \mathbf{q} \rangle - \langle \zeta, \mathcal{D}_{int} \rangle - \langle \zeta, \mathbf{q}\cdot\mathbf{n} \rangle_{\gamma_\mathbf{q}} \tag{80}$$

The weak form of the momentum balance and energy equations for body Ω can be expressed in short notation as

$$\left.\begin{array}{l} \mathbf{G}_{\mathbf{u},dyn} = 0 \\ \mathbf{G}_{\theta,dyn} = 0 \end{array}\right\} \forall \boldsymbol{\eta} \in \mathrm{V}, \forall \zeta \in \mathrm{T} \tag{81}$$

A.5 Mixed displacement-pressure formulation for the IBVP

It is well known that pure displacement formulations are not suitable for problems in which the constitutive behavior exhibit incompressibility since they tend to experience locking. Locking means, in this context, that the constraint conditions due to incompressibility cannot be satisfied. These constraint conditions are related to the pure volumetric mode (in the elastic case the condition is $\det(\mathbf{F}^e) = 1$ see equation (93) and for plastic flow the condition is $\det(\mathbf{F}^p) = \det(\mathbf{C}^p) = 1$, see equation (94)). Thus, this behavior is also called volumetric locking. As locking is present in the modelling of metal plasticity, we adopt a mixed formulation in the momentum balance equation of the workpiece. Introducing a pressure/deviatoric decomposition of the Cauchy stress tensor, the standard expression of the equilibrium equations becomes.

$$\mathbf{G}_{\mathbf{u},dyn} = \mathbf{G}_{\mathbf{u},stat} + \langle \boldsymbol{\eta}, \rho\dot{\mathbf{v}} \rangle \tag{82}$$
$$\mathbf{G}_{\mathbf{u},stat} = \langle dev(\boldsymbol{\sigma}) + p\mathbb{1}, \nabla^s\boldsymbol{\eta} \rangle - \langle \boldsymbol{\eta}, \mathbf{b} \rangle - \langle \mathbf{t}, \boldsymbol{\eta} \rangle_{\gamma_\sigma} \tag{83}$$

The pressure field p in the variational equation (82) is an additional variable determined by the volumetric part of the material model. In our case a Neo-Hookean material [8, 77] is used. It will be introduced in section (B). The resultant continuity equation is given by

$$p - \kappa\ \ln(J) + 3\,\alpha\,\kappa\,\frac{(1-\ln(J))}{J}(\theta - \theta_0) = 0 \tag{84}$$

where $\kappa > 0$ and α can be interpreted as the bulk modulus and the thermal expansion coefficient, respectively. J is the determinant of the deformation gradient, see equation (93).

The weak form of the pressure constitutive equation can be obtained by taking the L_2 inner product of with any valued function $q \in \mathrm{Q}$, being Q the space of virtual pressures

$$\mathrm{Q} := \left\{ q \in p(\Omega) \to \mathbb{R} \ \mid q\,\big|_{\gamma_p} = 0 \right\} \tag{85}$$

The variational equation that represents the weak form of the pressure constitutive equation can be expressed as

$$\int_{V_t} q \left[p - \kappa \, \ln(J) - 3 \, \alpha \, \kappa \, \frac{(1 - \ln(J))}{J} (\theta - \theta_0) \right] dV_t = 0 \quad \forall q \in Q \tag{86}$$

or in an alternative form

$$\mathbf{G}_{\boldsymbol{\tau}} = \mathbf{G}_{\boldsymbol{\tau},p} + \langle p, q \rangle \tag{87}$$

$$\mathbf{G}_{\boldsymbol{\tau},p} = \left\langle \kappa \, \ln(J) - 3 \, \alpha \, \kappa \, \frac{(1 - \ln(J))}{J} (\theta - \theta_0), q \right\rangle \forall q \in Q \tag{88}$$

Taking into account the mixed formulation for the momentum and energy balance equations take the form

$$\left.\begin{array}{l} \mathbf{G}_{\mathbf{u},dyn} = 0 \\ \mathbf{G}_{\theta,dyn} = 0 \\ \mathbf{G}_{\boldsymbol{\tau}} = 0 \end{array}\right\} \forall \boldsymbol{\eta} \in \mathrm{V}, \forall \zeta \in \mathrm{T}, \forall q \in Q \tag{89}$$

B Thermo-elastoplasticity model at finite strains

In the treatment of the themo-mechanical coupling, the constitutive equations must account material and geometrical non-linearities. In the mechanical part, a material model with the finite strain elasto-plasticity and the multiplicative decomposition of the deformation gradient will be used.

The decomposition of the deformation gradient into elastic and plastic parts is defined by

$$\mathbf{F}(\mathbf{X}, t) = \mathbf{F}^e(\mathbf{X}, t) \mathbf{F}^p(\mathbf{X}, t) \tag{90}$$

If we are taking in account finite strains, the deformation measures used are the Green Lagrange and the Almansi strain tensors which describe the strain in the material and in the spatial configuration respectively.

$$\mathbf{E} := \frac{1}{2}(\mathbf{C} - \bar{\mathbb{1}}) \quad \textit{and} \quad \mathbf{e} := \frac{1}{2}(\mathbb{1} - \mathbf{c}) \tag{91}$$

where

$$\mathbf{C} := \mathbf{F}^T \mathbf{F} \quad \textit{and} \quad \mathbf{b} := \mathbf{F} \mathbf{F}^T, \quad \textit{then} \quad \mathbf{c} := \mathbf{b}^{-1} = (\mathbf{F} \mathbf{F}^T)^{-1} = \mathbf{F}^{-T} \mathbf{F}^{-1} \tag{92}$$

and $\bar{\mathbb{1}}$ and $\mathbb{1}$ denotes the symmetric unit tensor in the reference and the current configurations respectively.

A Neo-Hookean model will be taken as a reference for the finite strains elastic behaviour. Once the material reaches plasticity, the thermal behaviour must be taken into account. In most materials the stress-strain relationship is affected by the strain rate and temperature during plastic deformation. For a given value of strain we can encounter: (i) the stress is higher for a higher strain rate and (ii) the stress is lower for higher temperatures.

The materials to be treated will be metals-type. In this case the formulation of the constitutive equations is based on two basic assumptions:

1. The stress response is isotropic. Therefore, the free energy is independent of the orientation of the reference configuration
2. The plastic flow is isochoric (standard assumption in metal plasticity)

$$\begin{aligned} \det(\mathbf{F}^p) &= \det(\mathbf{C}^p) = 1 \\ \det(\mathbf{F}) &= \det(\mathbf{F}^e) = J^e = J \end{aligned} \tag{93}$$

where $\mathbf{C}^p$ is the plastic part of the Cauchy-Green tensor is defined as

$$\mathbf{C}^p := \mathbf{F}^{pT}\mathbf{F}^p \tag{94}$$

With these two assumptions, we proceed to outline the governing equations of the model beginning with the thermo-hyperelastic model and continuing with the thermo-hyperelastoplastic one.

B.1 Constitutive thermo-hyperelastic model

The first model considered will be an hyperelastic model under temperature effects. The first assumption is the material isotropy and the second one the thermal response. Volumetric changes in the constitutive response must be accounted due to the variation of the temperature in the material.

The Neo-Hookean material used to represent the phenomenology mentioned above is represented with the following free energy function, see [8, 77].

$$\hat{\psi}(\mathbf{b}) = \hat{U}(J) + \hat{W}(\mathbf{b}) + \hat{M}(\theta, J) \tag{95}$$

The elastic part of the free energy is uncoupled into volumetric/deviatoric response described by the functions $\hat{U}(J)$ and $\hat{W}(\mathbf{C})$, respectively. The function $\hat{M}(\theta, J)$ describes the thermo-mechanical coupling due to thermal expansion and provides the potential for the associated elastic structural entropy.

$$\begin{aligned} \hat{U}(J) &= \frac{1}{2}\kappa \ln^2(J) \\ \hat{W}(\mathbf{b}) &= \frac{1}{2}\,\mu\left[tr(\bar{\mathbf{b}}) - 3\right] = \frac{1}{2}\,\mu\left[tr(\bar{\mathbf{C}}) - 3\right] \\ \hat{M}(\theta, J^e) &= -3\,\alpha\,\kappa\,\frac{\ln(J)}{J}(\theta - \theta_0) \end{aligned} \tag{96}$$

where $\mu > 0$, $\kappa > 0$, $c > 0$ and α can be interpreted as the shear modulus, the bulk modulus, the heat capacity and the thermal expansion coefficient,respectively. $\bar{\mathbf{C}}$ and $\bar{\mathbf{b}}$ are the volume preserving right Cauchy-Green tensor and the volume preserving

left Cauchy-Green tensor. If $\bar{\mathbf{F}}$ denote the volume preserving part of the deformation gradient, then $\det(\bar{\mathbf{F}}) = \mathbb{1}$. Recalling that $J := \det(\mathbf{F})$ gives the volume change, then

$$\bar{\mathbf{F}} := J^{-\frac{1}{3}}\mathbf{F} \Rightarrow \det(\bar{\mathbf{F}}) = 1 \tag{97}$$

Associated with $\mathbf{F}$ and $\bar{\mathbf{F}}$ we define the volumetric preserving part of the right Cauchy-Green tensor and the volume preserving left Cauchy-Green tensor as

$$\bar{\mathbf{C}} = J^{-\frac{2}{3}}\mathbf{C} = J^{-\frac{2}{3}}\mathbf{F}^T\mathbf{F} \tag{98}$$

and

$$\bar{\mathbf{b}}^e = J^{-\frac{2}{3}}\mathbf{b}^e \quad where \quad \mathbf{b}^e := \mathbf{F}^e\mathbf{F}^{eT} = \mathbf{F}(\mathbf{C}^p)^{-1}\mathbf{F}^T \tag{99}$$

The free energy function $\hat{\psi}(\mathbf{b})$ (95) satisfies two important properties:

- $\hat{\psi}(\mathbf{b})$ is invariant when the current configuration undergoes a rigid body rotation. This is because $\hat{\psi}(\mathbf{b})$ only depends on the stretching part $\mathbf{U} = \sqrt{\mathbf{C}}$ and is independent of the rotation part $\mathbf{R}$ of $\mathbf{F}$, $\mathbf{F} = \mathbf{UR}$ (Objectivity)
- $\hat{\psi}(\mathbf{b})$ on any translated and/or rotated reference configuration is the same at any time t (Isotropy)

From equation (95) and applying, the standard Coleman-Noll procedure leads to a constitutive equation expressed in terms of material variables as follows:

$$\begin{aligned}
\mathbf{S} &= 2\frac{\partial\hat{\psi}}{\partial\mathbf{C}}\mathbf{C} \\
&= 2\,\kappa\frac{\ln(J)}{J}\frac{\partial J}{\partial\mathbf{C}} - 6\,\alpha\,\kappa\,\frac{(1-\ln(J))}{J}(\theta-\theta_0)\frac{\partial J}{\partial\mathbf{C}} + \mu\,\frac{\partial tr(\bar{\mathbf{C}})}{\partial\mathbf{C}} \\
&= \kappa\left[\ln(J) - 3\,\alpha\,\frac{(1-\ln(J))}{J}(\theta-\theta_0)\right]\mathbb{C}^{-1} + 2\,\mu\,J^{-\frac{2}{3}}\left[\mathbb{I} - \frac{1}{3}tr(\mathbf{C})\mathbf{C}^{-1}\right]
\end{aligned} \tag{100}$$

or its terms in spatial variables as follows:

$$\begin{aligned}
\boldsymbol{\sigma} &= \frac{1}{J}\,\mathbf{F}\mathbf{S}\mathbf{F}^T \\
&= \frac{\kappa}{J}\left[\ln(J) - 3\,\alpha\,\frac{(1-\ln(J))}{J}(\theta-\theta_0)\right]\mathbb{1} + 2\,\mu\,J^{-\frac{5}{3}}\,dev(\mathbf{b})
\end{aligned} \tag{101}$$

B.2 Constitutive thermo-hyperelastoplastic model

Consistent with the assumption of isotropy and extending the hyperelastic model to plasticity we characterize the stress response by a stored energy with the form

$$\hat{\psi} = \hat{U}(J^e) + \hat{W}(\bar{\mathbf{b}}^e) + \hat{M}(\theta, J^e) + \hat{T}(\theta) + \hat{K}(\bar{e}^{\,p}, \theta) \tag{102}$$

The elastic part of the free energy is uncoupled into volumetric/deviatoric response described by the functions $\hat{U}(J^e)$ and $\hat{W}(\bar{\mathbf{b}}^e)$, respectively. The function $\hat{M}(\theta, J^e)$ describes the thermo-mechanical coupling due to thermal expansion and provides the potential for the associated elastic structural entropy, while the function $\hat{T}(\theta)$ is the potential for the purely thermal entropy. The function $\hat{K}(\bar{e}^{\,p}, \theta)$ is a nonlinear function of the equivalent plastic strain $\bar{e}^{\,p}$ and temperature θ which describes the isotropic strain hardening via the relation $\beta = -\partial_{\bar{e}^{\,p}} \hat{K}(\bar{e}^{\,p}, \theta)$. To make matters as concrete as possible, we consider the following explicit forms [79, 14].

$$
\begin{aligned}
\hat{U}(J^e) &= \frac{1}{2}\kappa \ln^2(J^e) \\
\hat{W}(\bar{\mathbf{b}}^e) &= \frac{1}{2}\,\mu\left[tr(\bar{\mathbf{b}}^e) - 3\right] = \frac{1}{2}\,\mu\left[tr(\bar{\mathbf{C}}^e) - 3\right] \\
\hat{T}(\theta) &= c\left[(\theta - \theta_0) - \theta \ln\left(\frac{\theta}{\theta_0}\right)\right] \\
\hat{M}(\theta, J^e) &= -3\,\alpha\,\kappa\,\frac{\ln(J^e)}{J^e}(\theta - \theta_0)
\end{aligned}
\tag{103}
$$

where $\mu > 0$, $\kappa > 0$, $c > 0$ and α can be interpreted as the shear modulus, the bulk modulus, the heat capacity and the thermal expansion coefficient,respectively.

Some remarks can be made about the structure of the free energy function (102):

1. the structure of the free energy is usually restricted to temperature independent material properties
2. the thermoelastic free energy is decoupled from the plastic contribution $\partial_{\bar{e}^{\,p}} \hat{K}(\bar{e}^{\,p}, \theta)$ associated with the hardening variable $\bar{e}^{\,p}$ (this assumption is motivated by the experimental observation that the lattice structure remains unaffected by the plastic deformation) [79]
3. The functions $\hat{U}(J^e)$ and $\hat{W}(\bar{b}^e)$ generalize the linear isotropic elastic model
4. The function $\hat{K}(\bar{e}^{\,p}, \theta)$ represents the visible (macroscopic) plastic deformations that are the result of microscopic dislocation(crystallographic defects in the crystal structure) motion and multiplication. Generally, the material exhibits high strength if there are either high levels of dislocations or no dislocations. In addition, the function $\hat{K}(\bar{e}^{\,p}, \theta)$ represents the yield stress decreasing as the grain size is increased [48]. Also, $\hat{K}(\bar{e}^{\,p}, \theta)$ represents the decrease in dislocation density due to the heating of the material above its critical temperature (thermal softening).

There are four main strengthening mechanisms for metals, each one is a method to prevent dislocation motion and propagation, or make it energetically unfavorable for the dislocation to move (work hardening, solid solution strengthening, precipitation hardening and grain boundary strengthening).

In addition, there are other factors that affect the shape and the magnitude of the hardening potential among them [12]: (i) material composition, (ii) previous heat treatment, (iii) the type of crystal structure and (iv) prior history of plastic deformation. Different hardening potentials that represent the work hardening phenomenon have been proposed in the literature, which reflect some of the strain hardening patterns observed in the experiments. Among them the following:

B.2.1 *Voce and Simo* hardening potential

Voce [85] presented and *Simo* [79] applied the following potential describing isotropic hardening:

$$\begin{aligned} \hat{K}(\bar{e}^{\,p},\theta) &= \frac{1}{2}\,h(\theta)(\bar{e}^{\,p})^2 \;-\left[\sigma_0(\theta)-\sigma_\infty(\theta)\right]\;\hat{H}(\bar{e}^{\,p}) \\ \hat{H}(\bar{e}^{\,p}) &= \begin{cases} \bar{e}^{\,p}-\dfrac{1-\exp^{-\delta\bar{e}^{\,p}}}{\delta} & \text{for} \quad \delta\neq 0 \\ 0 & \text{for} \quad \delta = 0 \end{cases} \end{aligned} \tag{104}$$

where δ is the saturation exponent and the functions $h(\theta)$, $\sigma_0(\theta)$ and $\sigma_\infty(\theta)$ describe linear thermal softening.

$$\begin{array}{lcl} \sigma_0(\theta) & = & \sigma_0(\theta_0)\,(1-w_0(\theta-\theta_0)) \\ \sigma_\infty(\theta) & = & \sigma_\infty(\theta_0)\,(1-w_h(\theta-\theta_0)) \\ h(\theta) & = & h(\theta_0)\,(1-w_h(\theta-\theta_0)) \end{array} \tag{105}$$

where $\sigma_0(\theta_0)$ is the initial yield stress, $\sigma_\infty(\theta_0)$ is the final saturation hardening stress, $h(\theta_0)$ is the linear hardening modulus, all obtained at the reference temperature θ_0, while w_0 and w_h are the flow stress softening and hardening softening parameter, respectively.

The above potential allows us to study materials exhibiting a combination of linear and saturation-type hardening.

B.3 Yield condition

Accurate flow stress models are considered extremely necessary to represent work material constitutive behavior under high strain rate deformation conditions. We consider the classical *Mises-Hubber* yield conditions, expressed in terms of the Kirchhoff stress tensor, for the case of rate independent plasticity:

$$\Phi(\tau,\bar{e}^{\,p},\theta) = \|dev(\tau)\| - \sqrt{\frac{2}{3}}\left(\sigma_y - \hat{K}'(\bar{e}^{\,p},\theta)\right) = \|dev(\tau)\| - \sqrt{\frac{2}{3}}\,(\sigma_y+\beta) \leq 0 \tag{106}$$

and for rate dependent plasticity

$$
\begin{gathered}
f(\tau, \bar{e}^{\,p}, \theta) = \|dev(\tau)\| - \sqrt{\frac{2}{3}}\,(\sigma_y + \beta)\left(1 + g(\dot{\bar{e}}^{p})\right) = 0 \\
\text{or} \\
f(\tau, \bar{e}^{\,p}, \theta) = \Phi(\tau, \bar{e}^{\,p}, \theta) - \sqrt{\frac{2}{3}}\,(\sigma_y + \beta)\, g(\dot{\bar{e}}^{p}) = 0 \\
\text{if } \Phi(\tau, \bar{e}^{\,p}, \theta) \; > 0
\end{gathered}
\tag{107}
$$

where σ_y denotes the flow stress, σ_{y_0} denotes the flow stress at $\theta = \theta_0$, $\beta = -K'(\bar{e}^{\,p}, \theta)$ the isotropic nonlinear hardening modulus, β_0 the isotropic hardening at $\theta = \theta_0$, $g(\dot{\bar{e}}^{p})$ the strain rate hardening modulus and $\bar{e}^{\,p}$ the hardening parameter. The expressions $(\sigma_y + \beta)$ y and $g(\dot{\bar{e}}^{p})$ depend on the hardening law used. Numerous empirical and semi-empirical flow stress models have been proposed. Some examples of strain-rate dependent models have been developed by *Johnson and Cook* [45] and *Bäker* [4]. *Simo* [79] proposed the strain dependent model that will be used in this work.

B.3.1 *Simo* flow model

In the *Simo* flow model a particular expression is proposed to define the hardening and thermal softening condition $(\sigma_y + \beta)$:

$$
\begin{gathered}
(\sigma_y + \beta) = \hat{\sigma}_y + \hat{H}(\bar{e}^{\,p}) + (\hat{K}_{inf} - \hat{\sigma}_y)\,(1 - \exp(-\delta \bar{e}^{\,p})) \\
\text{where} \\
\hat{\sigma}_y = \sigma_y\,(1 - w_0(\theta - \theta_0)) \\
\hat{H} = H\,(1 - w_h(\theta - \theta_0)) \\
\hat{K}_{inf} = K_{inf}\,(1 - w_h(\theta - \theta_0))
\end{gathered}
\tag{108}
$$

This model describes the strain hardening and thermal softening for most steels in temperature range between 300K and 400K [79]. Common values of material constants of the *Simo* yield function are shown in Table 4.

Table 4: Simo yield function. Material properties

Yield Stress	σ_y	450	MPa
Flow Stress Softening	w_0	0.002	K^{-1}
Reference Temperature	θ_0	293.15	K
Linear Hardening	H	129.24	MPa
Hardening Softening	w_h	0.002	K^{-1}
Saturation Hardening	K_{inf}	715	MPa
Hardening Exponent	δ	16.93	

B.4 Associative flow rule

The functional form of the corresponding associate flow rule is uniquely determined analysing the evolution equations and the plastic dissipation. For the *Mises-Hubber* yield function (110) and the free energy function (109), *Simo* [79] and *Ibrahimbegovic* [41] show that the flow rule takes the form based on the principle of maximum plastic dissipation.

$$\hat{\psi} = \hat{T}(\theta) + \hat{M}(\theta, J^e) + \hat{U}(J^e) + \hat{W}(\bar{\mathbf{b}}^e) + \hat{K}(\bar{e}^{\,p}, \theta) \tag{109}$$

$$f(\tau, \bar{e}^{\,p}, \theta) = \|dev(\tau)\| - \sqrt{\frac{2}{3}}\,(\sigma_y + \beta)\left(1 + g(\dot{\bar{e}}^{p})\right) = 0 \tag{110}$$

A detailed procedure about how to get the flow rule is shown in the following lines. First defining the plastic mechanical dissipation and then the evolution equations.

B.4.1 Mechanical Dissipation

Due to the restriction to isotropy implied by the thermo-elastic domain, the functional form of the internal energy function $\mathbf{e}$ can be written as

$$\mathbf{e} = \hat{\mathbf{e}}(\bar{\mathbf{b}}^e, \bar{e}^{\,p}, \eta^e) \;\text{ with }\; \eta^e = \eta - \eta^p \tag{111}$$

where η is the entropy of the system, $\bar{e}^{\,p}$ is the equivalent plastic strain and $\bar{\mathbf{b}}^e$ is the elastic left Cauchy-Green tensor. The free energy can be expressed in terms of the internal energy via the Legendre transformation (55) as

$$\hat{\psi}(\bar{\mathbf{b}}^e, \bar{e}^{\,p}, \theta) = \hat{\mathbf{e}}(\bar{\mathbf{b}}^e, \bar{e}^{\,p}, \theta) - \eta^p\,\theta \tag{112}$$

Applying the second Law of Thermodynamics, constitutive equations consistent with the assumed free energy function are derived. This gives the expression of the energy dissipation as

$$\mathcal{D} = \tau \cdot \mathbf{d} + \theta\,\dot{\eta} - \dot{\mathbf{e}} = \tau \cdot \mathbf{d} + \theta\,\dot{\eta} - \dot{\hat{\psi}} - \dot{\eta}^e\,\theta - \eta^e\,\dot{\theta} \tag{113}$$

differentiating the free energy function $\hat{\psi}$ of the equation (109) with respect to time

$$\dot{\hat{\psi}} = \frac{\partial \hat{\psi}}{\partial \bar{\mathbf{b}}^e}\dot{\bar{\mathbf{b}}}^e + \frac{\partial \hat{\psi}}{\partial \bar{e}^{\,p}}\,\dot{\bar{e}}^p + \frac{\partial \hat{\psi}}{\partial \theta}\dot{\theta} \tag{114}$$

and taking the derivative of $\mathbf{b}^e$ with respect to time.

$$\dot{\mathbf{b}}^e = \dot{\mathbf{F}}\mathbf{F}^{-1}\mathbf{F}(\mathbf{C}^p)^{-1}\mathbf{F}^T + \mathbf{F}(\mathbf{C}^p)^{-1}\mathbf{F}^T\mathbf{F}^{-T}\dot{\mathbf{F}}^T + \mathbf{F}(\dot{\mathbf{C}}^p)^{-1}\mathbf{F}^T \tag{115}$$

Using the definition of the spatial velocity gradient $\mathbf{l} = \dot{\mathbf{F}}\mathbf{F}^{-1}$ and the Lie derivative of the elastic left Cauchy Green tensor $\mathcal{L}_v\mathbf{b}^e$ (117), the time derivative of $\mathbf{b}^e$ is written as

$$\dot{\mathbf{b}}^e = \mathbf{l}\mathbf{b}^e + \mathbf{b}^e\mathbf{l}^T + \mathcal{L}_v\mathbf{b}^e \tag{116}$$

Remark. *The Lie derivative for the tensor* $\mathbf{b}^e$ *is defined as*

$$\mathcal{L}_v\mathbf{b}^e = \mathbf{F}\{\frac{\partial}{\partial t}[\mathbf{F}^{-1}\mathbf{b}^e\mathbf{F}^{-T}]\}\mathbf{F}^T = \mathbf{F}\frac{\partial}{\partial t}[(\mathbf{C}^p)^{-1}]\mathbf{F}^T = \mathbf{F}(\dot{\mathbf{C}}^p)^{-1}\mathbf{F}^T \tag{117}$$

The Lie derivative of $\mathbf{b}^e$ *tensor is exactly the push forward of the time derivative of the pull-back of the spatial tensor* $\mathbf{b}^e$*. More information about push-forward and pull-back operations is given in references [8, 7]. Inserting equation (116) into equation (114), the derivative of the free energy function* $\hat{\psi}$ *becomes*

$$\dot{\hat{\psi}} = \frac{\partial \hat{\psi}}{\partial \mathbf{b}^e}\,(2\mathbf{l}\mathbf{b}^e + \mathcal{L}_v\mathbf{b}^e) + \frac{\partial \hat{\psi}}{\partial \bar{e}^{\,p}}\,\dot{\bar{e}}^p + \frac{\partial \hat{\psi}}{\partial \theta}\dot{\theta} \tag{118}$$

By inserting the relation $\mathbf{d} = sym[\mathbf{l}]$ into (118) and using the Lengendre Transformation (112), the dissipation inequality becomes

$$\mathcal{D} = \dot{\eta}^p\,\theta + \left(-\frac{\partial \hat{\psi}}{\partial \theta} - \eta + \eta^p\right)\,\theta + \left(\tau - 2\frac{\partial \hat{\psi}}{\partial \mathbf{b}^e}\mathbf{b}^e\right)\,\mathbf{d} - \frac{\partial \hat{\psi}}{\partial \mathbf{b}^e}\mathcal{L}_v\mathbf{b}^e - \frac{\partial \hat{\psi}}{\partial \bar{e}^{\,p}}\,\dot{\bar{e}}^p \geq 0 \tag{119}$$

By demanding that (119) hold for all admissible processes, the Kirchhoff stress tensor is obtained by the general expression:

$$\begin{aligned} \boldsymbol{\tau} &= 2\frac{\partial \hat{\psi}}{\partial \mathbf{b}^e}\mathbf{b}^e = 2\mathbf{F}^e\frac{\partial W}{\partial \mathbf{C}^e}\mathbf{F}^{eT} \\ &= J^e\left[-3\,\alpha\,\kappa\,\frac{(1-\ln(J^e))}{(J^e)^2}(\theta-\theta_0) - \kappa\,\frac{\ln(J^e)}{J^e}\right]\,\mathbb{1} + \mu\,dev(\bar{\mathbf{b}}^e) \end{aligned} \tag{120}$$

The hydrostatic and deviatoric parts of the Kirchhoff stress tensor are

$$\mathbf{p} := \left[-3\,\alpha\,\kappa\,\frac{(1-\ln(J^e))}{J^e}(\theta-\theta_0) - \kappa\,\ln(J^e)\right]\,\mathbb{1} \tag{121}$$

$$\mathbf{s} := \mu\, dev(\bar{\mathbf{b}}^e) \tag{122}$$

and the entropy constitutive equation

$$\eta = \eta^p - \frac{\partial\hat{\psi}}{\partial\theta} = \eta^p - \partial_\theta\hat{T}(\theta) - \partial_\theta\hat{M}(\theta, J^e) - \partial_\theta\hat{K}(\bar{e}^{\,p},\theta) \tag{123}$$

The dissipation inequality becomes

$$\mathcal{D}_{mech} := \mathcal{D} = \dot{\eta}^p\,\theta - \frac{\partial\hat{\psi}}{\partial\mathbf{b}^e}\mathcal{L}_v\mathbf{b}^e - \frac{\partial\hat{\psi}}{\partial\bar{e}^{\,p}}\,\dot{\bar{e}}^p \geq 0 \tag{124}$$

B.4.2 Evolution equations and maximum plastic dissipation

Now, we need to define the evolution equations for the internal variables in the model in order to complete the constitutive theory of plasticity at finite strains.

Based on the thermo-mechanical principle of maximum dissipation, the problem is to find the values of the stress, the isotropic nonlinear hardening and the temperature (τ,β,θ) such that the dissipation function (124) attains a maximum subject to the constraint $\Phi(\tau,\bar{e}^{\,p},\theta) \leq 0$ (rate-independent plasticity), prescribed the intermediate configuration ($\mathbf{b}^e$ is fixed) and prescribed the rates $(\mathcal{L}_v\mathbf{b}^e, \dot{\bar{e}}^p, \dot{\theta})$. The problem can be reformulated as a constrained minimization of the negative value of the dissipation

$$\begin{aligned}(\tau,\beta,\theta) &= \arg\left[\min_{\Phi(\tau,\bar{e}^{\,p},\theta)\leq 0}(-\mathcal{D})\right]\\ &= \arg\left[\min_{\Phi(\tau,\bar{e}^{\,p},\theta)\leq 0}\left(-\dot{\eta}^p\,\theta + \frac{\partial\hat{\psi}}{\partial\mathbf{b}^e}\mathcal{L}_v\mathbf{b}^e + \frac{\partial\hat{\psi}}{\partial\bar{e}^{\,p}}\,\dot{\bar{e}}^p\right)\right]\end{aligned} \tag{125}$$

But the problem can be expressed as an unconstrained minimization problem by introducing a Lagrangian functional

$$\begin{aligned}\partial_\tau L^p(\tau,\beta,\theta;\lambda) &= -\mathcal{D}(\tau,\beta,\theta) + \lambda\,\Phi(\tau,\bar{e}^{\,p},\theta)\\ &= -\dot{\eta}^p\theta + \frac{1}{2}\tau\cdot\mathcal{L}_v\mathbf{b}^e\mathbf{b}^{e-1} - \beta\dot{\bar{e}}^{\,p} + \lambda\,\Phi(\tau,\bar{e}^{\,p},\theta)\end{aligned} \tag{126}$$

The solution to the problem is given by

$$\partial_\tau L^p(\tau,\beta,\theta;\lambda) = \frac{1}{2}\mathcal{L}_v\mathbf{b}^e\mathbf{b}^{e-1} + \lambda\,\partial_\tau\Phi(\tau,\bar{e}^{\,p},\theta) = 0 \tag{127}$$

$$\partial_\beta L^p(\tau,\beta,\theta;\lambda) = -\dot{\bar{e}}^p + \lambda\,\partial_\beta\Phi(\tau,\bar{e}^{\,p},\theta) = 0 \tag{128}$$

$$\partial_\theta L^p(\tau,\beta,\theta;\lambda) = -\dot{\eta}^p + \lambda\,\partial_\theta\Phi(\tau,\bar{e}^{\,p},\theta) = 0 \tag{129}$$

where the consistency parameter λ is the Lagrange multiplier satisfying the *Kuhn-Tucker* conditions

$$\lambda > 0 \quad \Phi(\tau, \bar{e}^{\,p}, \theta) \leq 0 \quad \lambda\, \Phi(\tau, \bar{e}^{\,p}, \theta) = 0 \tag{130}$$

It is important to remark that the *Kuhn-Tucker* conditions are equivalent to the loading-unloading conditions. In summary, the evolution equations of the internal variables are

$$\begin{aligned} \mathcal{L}_v \mathbf{b}^e &= -2\,\lambda\, \partial_\tau \Phi(\tau, \bar{e}^{\,p}, \theta) \mathbf{b}^e \\ \dot{\bar{e}}^{\,p} &= -\lambda\, \partial_\beta \Phi(\tau, \bar{e}^{\,p}, \theta) \\ \dot{\eta}^p &= \lambda\, \partial_\theta \Phi(\tau, \bar{e}^{\,p}, \theta) \end{aligned} \tag{131}$$

From expressions (115) and (117), the Lie derivative of the elastic left Cauchy-Green tensor can be expressed in material description as

$$\begin{aligned} (\dot{\mathbf{C}}^p)^{-1} &= -2\,\lambda\, \partial_\tau f(dev(\tau), \bar{e}^{\,p}, \theta)\, (\mathbf{C}^p)^{-1} \\ &= -2\,\lambda\, \frac{dev(\tau)}{\|dev(\tau)\|} (\mathbf{C}^p)^{-1} = -2\,\lambda\, \frac{\mathbf{s}}{\|\mathbf{s}\|} (\mathbf{C}^p)^{-1} \\ \dot{\bar{e}}^{\,p} &= \lambda \sqrt{\frac{2}{3}} \\ \dot{\eta}^{\,p} &= \lambda \sqrt{\frac{2}{3}}\, (\partial_\theta \sigma + \partial_\theta \beta) \end{aligned} \tag{132}$$

Using the specific constitutive equations and decomposing $\mathbf{b}^e$ into its spherical and deviatoric parts, the exact flow rule (131) becomes

$$\mathcal{L}_v \mathbf{b}^e = -2\,\lambda\, J^{-\frac{2}{3}}\, \mathbf{n}^2\, \frac{\|\mathbf{s}\|}{\mu} - 2\,\lambda\, J^{-\frac{2}{3}}\, \frac{1}{3}\, tr(\bar{\mathbf{b}}^e)\, \mathbf{n} \tag{133}$$

The first term in (133) can be neglected in most metals, because this term is of the order of the flow stress over the shear modulus, which for metal plasticity, is of the order of 10^{-3} [79]. Using $\bar{\mathbf{F}} = J^{-\frac{1}{3}} \mathbf{F}$ at the modified flow rule

$$\begin{aligned} \mathcal{L}_v \mathbf{b}^e &= -2\,\lambda\, J^{-\frac{2}{3}}\, \frac{1}{3}\, tr(\bar{\mathbf{b}}^e)\, \mathbf{n} \\ \bar{\mathbf{F}} (\mathbf{C}^p)^{-1} \bar{\mathbf{F}}^T &= -2\,\lambda\, \frac{1}{3}\, tr(\bar{\mathbf{b}}^e)\, \mathbf{n} \end{aligned} \tag{134}$$

C Time integration of the constitutive law

The problem of integrating numerically the initial-value ODE equations represented by (132) in conjunction with the condition (130) is the focus of this appendix.

C.1 Implicit Backward-Euler integration scheme

Let $(\mathbf{C}_n^p)^{-1}, \bar{e}^p, \theta_n$ denote the initial state at time t_n, and assume that the deformation gradient and temperature field $\mathbf{F}_{n+1}, \theta_{n+1}$ at time t_{n+1} are prescribed. Let us focus on the time step $t_n \to t_{n+1}$, where $\Delta t = t_{n+1} - t_n$. Using an implicit unconditionally stable scheme on (134) and the scalar equations of (131) gives

$$\begin{aligned} \bar{\mathbf{F}}_{n+1}\left((\mathbf{C}_{n+1}^p)^{-1} - (\mathbf{C}_n^p)^{-1}\right)\bar{\mathbf{F}}_{n+1}^T &= -2\,\lambda_{n+1}\,\Delta t\frac{1}{3}tr(\bar{\mathbf{b}}_{n+1}^e)\mathbf{n}_{n+1} \\ \bar{e}_{n+1}^p - \bar{e}_n^p &= \lambda_{n+1}\,\Delta t\sqrt{\frac{2}{3}} \\ \eta_{n+1}^p - \eta_n^p &= \lambda_{n+1}\,\Delta t\sqrt{\frac{2}{3}}\,(\partial_\theta\sigma_y + \partial_\theta\beta) \end{aligned} \tag{135}$$

The right hand side of equation (135) in terms of spatial variables becomes

$$\bar{\mathbf{b}}_{n+1}^e - \bar{\mathbf{F}}_{n,n+1}\,\bar{\mathbf{b}}_n^e\,\bar{\mathbf{F}}_{n,n+1}^T = -2\,\lambda_{n+1}\,\Delta t\frac{1}{3}tr(\bar{\mathbf{b}}_{n+1}^e)\mathbf{n}_{n+1} \tag{136}$$

along with the following counterpart of the loading-unloading conditions:

$$\lambda\Delta t \geq 0 \quad f_{n+1}(\tau_{n+1}, \bar{e}_{n+1}^p, \theta_{n+1}) \leq 0 \quad \lambda_{n+1}\Delta t\, f_{n+1}(\tau_{n+1}, \bar{e}_{n+1}^p, \theta_{n+1}) = 0 \tag{137}$$

where the yield condition is defined by the *Mises* criterion

$$f_{n+1}(\tau_{n+1}, \bar{e}_{n+1}^p, \theta_{n+1}) = \|\,dev(\tau_{n+1})\| - \sqrt{\frac{2}{3}}\,(\sigma_{y,n+1} + \beta_{n+1}) \tag{138}$$

A closed form solution of these equations is obtained by defining the thermo-elastic state by the relationships

$$\begin{aligned} \bar{\mathbf{b}}_{n+1}^{e,trial} &= \bar{\mathbf{F}}_{n,n+1}\,\mathbf{C}_n^{p\,-1}\,\bar{\mathbf{F}}_{n,n+1}^T = \bar{\mathbf{F}}_{n,n+1}\,\mathbf{b}_n^e\,\bar{\mathbf{F}}_{n,n+1}^T \\ \mathbf{s}_{n+1}^{trial} &= \mu\,dev(\bar{\mathbf{b}}_{n+1}^{e,trial}) \\ f_{n+1}^{trial} &= \left\|\mathbf{s}_{n+1}^{trial}\right\| - \sqrt{\frac{2}{3}}\,(\sigma_{y,n+1} + \beta_{n+1}(\bar{e}_n^p)) \end{aligned} \tag{139}$$

We observe that the trial state is determined solely in terms of the initial conditions $\mathbf{b}_n^e, \bar{e}_n^p, \theta_n$ and the given incremental deformation gradient $\bar{\mathbf{F}}_{n,n+1}$. We remark that this state may not correspond to any actual state, unless the incremental process is elastic. An analysis of equation (139) reveals two alternative situations:

First, we consider the case for which

$$f_{n+1}^{trial} < 0 \tag{140}$$

It follows that the trial state is admissible in the sense that

$$\begin{aligned}
\bar{\mathbf{b}}^{e}_{n+1} &= \bar{\mathbf{b}}^{e,trial}_{n+1} = \bar{\mathbf{F}}_{n,n+1}\,\mathbf{C}^{p\,-1}_{n}\,\bar{\mathbf{F}}^{T}_{n,n+1} = \bar{\mathbf{F}}_{n,n+1}\,\mathbf{b}^{e}_{n}\,\bar{\mathbf{F}}^{T}_{n,n+1} \\
\mathbf{s}_{n+1} &= \mathbf{s}^{trial}_{n+1} \\
\mathbf{s}^{trial}_{n+1} &= \mu\, dev(\bar{\mathbf{b}}^{e,trial}_{n+1}) \\
\bar{e}^{p}_{n+1} &= \bar{e}^{p}_{n}
\end{aligned} \tag{141}$$

and satisfy

1. The stress strain relationship
2. The flow rule and the hardening law with $\Delta\lambda_{n+1} = \lambda_{n+1}\Delta t = 0$
3. The *Kuhn-Tucker* conditions, since

$$f_{n+1}(\tau_{n+1}, \bar{e}^{p}_{n+1}, \theta_{n+1}) = f^{trial}_{n+1} \leq 0 \quad \Delta\lambda_{n+1} = 0 \tag{142}$$

satisfy (137).

Next, we consider the case for which $f^{trial}_{n+1} > 0$. Clearly, the trial state cannot be a solution to the incremental problem since $\bar{\mathbf{b}}^{e,trial}_{n+1}, \bar{e}^{p}_{n}, \theta_n$ violates the constraint condition $f_{n+1}(\tau_{n+1}, \bar{e}^{p}_{n+1}, \theta_{n+1}) \leq 0$. As a result, we require that $\Delta\lambda_{n+1} \geq 0$ so that $\bar{e}^{p}_{n+1} \neq \bar{e}^{p}_{n}$ to obtain $\mathbf{s}_{n+1} \neq \mathbf{s}^{trial}_{n+1}$.

To summarize our results, the conclusion that an incremental process for given incremental deformation gradient is elastic or plastic is drawn solely on the basis of the trial state according to the criterion

$$f^{trial}_{n+1} \begin{cases} \leq 0 & \Rightarrow \quad elastic\,step \quad \Delta\lambda_{n+1} = 0 \\ \geq 0 & \Rightarrow \quad plastic\,step \quad \Delta\lambda_{n+1} > 0 \end{cases}$$

Here we focus on the algorithmic problem for an incremental plastic process characterized by the conditions

$$f^{trial}_{n+1} > 0 \Leftrightarrow f_{n+1}(\tau_{n+1}, \bar{e}^{p}_{n+1}, \theta_{n+1}) = 0 \tag{143}$$

and

$$\Delta\lambda_{n+1} > 0 \tag{144}$$

The objective is to determine the solution $(\bar{\mathbf{b}}^{e}_{n+1}, \bar{e}^{\,p}_{n+1}, \theta_{n+1}, \mathbf{s}_{n+1}, \Delta\lambda_{n+1})$ to the problem (136), (137) and (138). To accomplish this we express the isochoric Kirchhoff stress tensor $\mathbf{s}_{n+1}$ in terms of $\mathbf{s}^{trial}_{n+1}$ and $\Delta\lambda_{n+1}$ as follows

$$\begin{aligned}
\mathbf{s}_{n+1} &= \mu\, dev(\bar{\mathbf{b}}^{e}_{n+1}) \\
&= \mu\, dev(\bar{\mathbf{F}}_{n,n+1}\,\mathbf{b}^{e}_{n}\,\bar{\mathbf{F}}^{T}_{n,n+1}) - 2\,\Delta\lambda_{n+1}\,\mu\,\frac{1}{3}\,tr(\bar{\mathbf{b}}^{e}_{n+1})\mathbf{n}_{n+1} \\
&= \mathbf{s}^{trial}_{n+1} - 2\,\Delta\lambda_{n+1}\,\mu\,\frac{1}{3}\,tr(\bar{\mathbf{b}}^{e}_{n+1})\mathbf{n}_{n+1}
\end{aligned} \tag{145}$$

The update of Kirchhoff stress tensor and the tensor $\mathbf{b}^e_{n+1}$ need the determination of the trace of $\mathbf{b}^e_{n+1}$. By taking the trace of equation (136) and using (139) we conclude that

$$tr(\bar{\mathbf{b}}^e_{n+1}) = tr(\bar{\mathbf{b}}^{e,trial}_{n+1}) \tag{146}$$

Then replacing (146) in (136) we get

$$\bar{\mathbf{b}}^e_{n+1} = \bar{\mathbf{b}}^{e,trial}_{n+1} - 2\,\lambda_{n+1}\,\Delta t\,\frac{1}{3}tr(\bar{\mathbf{b}}^{e,trial}_{n+1})\mathbf{n}_{n+1} \tag{147}$$

and using the hyperelastic relationships yields

$$\mathbf{s}_{n+1} = \mathbf{s}^{trial}_{n+1} - 2\,\Delta\lambda_{n+1}\,\mu\,\frac{1}{3}tr(\bar{\mathbf{b}}^{e,trial}_{n+1})\mathbf{n}_{n+1} \tag{148}$$

From (145) and the definition $\mathbf{s}_{n+1} = \|\mathbf{s}_{n+1}\|\mathbf{n}_{n+1}$, the normal $\mathbf{n}_{n+1}$ is determined in terms of the trial stress $\mathbf{s}^{trial}_{n+1}$

$$\begin{aligned}
\|\mathbf{s}_{n+1}\|\mathbf{n}_{n+1} &= \|\mathbf{s}^{trial}_{n+1}\|\mathbf{n}_{n+1} - 2\,\Delta\lambda_{n+1}\,\mu\,\frac{1}{3}tr(\bar{\mathbf{b}}^{e,trial}_{n+1})\mathbf{n}_{n+1}\\
\|\mathbf{s}^{trial}_{n+1}\|\mathbf{n}^{trial}_{n+1} &= \left[\|\mathbf{s}_{n+1}\| + 2\,\Delta\lambda_{n+1}\,\mu\,\frac{1}{3}tr(\bar{\mathbf{b}}^{e,trial}_{n+1})\right]\mathbf{n}_{n+1}\\
\|\mathbf{s}^{trial}_{n+1}\|\mathbf{n}_{n+1} &= \|\mathbf{s}^{trial}_{n+1}\|\mathbf{n}^{trial}_{n+1}\\
\mathbf{n}_{n+1} &= \mathbf{n}^{trial}_{n+1}
\end{aligned} \tag{149}$$

By taking the dot product of (145) with $\mathbf{n}_{n+1}$ and using (138), we obtain the following scalar nonlinear equations that determines the consistency parameter $\Delta\lambda_{n+1}$:

$$\begin{aligned}
g(\Delta\lambda_{n+1}) &= \|\mathbf{s}_{n+1}\| - 2\,\Delta\lambda_{n+1}\,\mu\,\frac{1}{3}tr(\bar{\mathbf{b}}^{e,trial}_{n+1}) - \sqrt{\frac{2}{3}}\left(\sigma_{y,n+1} + \beta_{n+1}(\bar{e}^p_{n+1})\right)\\
&= f^{trial}_{n+1} - 2\,\Delta\lambda_{n+1}\,\mu\,\frac{1}{3}tr(\bar{\mathbf{b}}^{e,trial}_{n+1}) + \sqrt{\frac{2}{3}}\left(\sigma_{y,n} + \beta_n(\bar{e}^p_n)\right)\\
&- \sqrt{\frac{2}{3}}\left(\sigma_{y,n+1} + \beta_{n+1}(\bar{e}^p_{n+1})\right)\\
&= 0
\end{aligned} \tag{150}$$

Equation (150) is effectively solved by a local Newton iterative procedure since $g(\Delta\lambda_{n+1})$ is a convex function for the isotropic hardening functions used in this work, and then convergence of the Newton-Raphson is guaranteed.

Once $\Delta\lambda_{n+1}$ is determined from (150) the intermediate configuration, the hardening variable and plastic entropy are updated from (135).

C.2 Algorithmic constitutive tensor

In the following lines, we provide an expression for the algorithmic tangent moduli, which is a key aspect in the linearization of the weak form of the momentum equation. The algorithmic constitutive tensor is developed for the implicit integration scheme and for the IMPL-EX scheme.

C.2.1 Algorithmic constitutive tensor: implicit integration scheme

The expression for the tangent moduli for the implicit stress update algorithm will be presented in the following lines

$$\frac{\partial \mathbf{S}_{n+1}}{\partial \mathbf{C}_{n+1}} = \delta_1 \mathbb{C}_{dev}^{trial} \; + \; \delta_2 \mathbf{N}_{n+1} \otimes \mathrm{Dev}(\mathbf{N}_{n+1}^2) \; + \; \delta_3 \mathbf{N}_{n+1} \otimes \mathbf{N}_{n+1} \tag{151}$$

where the coefficients δ_1, δ_2 and δ_3 are defined by the expressions

$$\delta_1 = \left(1 - \frac{2\,\mu\,\Delta\lambda_{n+1}}{\|\mathbf{S}_{n+1}^{trial}\|}\right) \tag{152}$$

$$\delta_2 = 2\left(\bar{\mu}\Delta\lambda_{n+1} - \frac{\bar{\mu}\,\|\mathbf{S}_{n+1}^{trial}\|}{\left(2\,\bar{\mu} + \frac{2}{3}\frac{d[\sigma_y+\beta]}{d\Delta\lambda_{n+1}}\right)}\right) \tag{153}$$

$$\delta_3 = \left(\frac{2\,\bar{\mu}^2\Delta\lambda_{n+1}}{\|\mathbf{S}_{n+1}^{trial}\|} + \frac{\bar{\mu}\,\frac{2}{3}\Delta\lambda_{n+1}\|\mathbf{S}_{n+1}^{trial}\| - 2\,\bar{\mu}^2}{\left(2\,\bar{\mu} + \frac{2}{3}\frac{d[\sigma_y+\beta]}{d\Delta\lambda_{n+1}}\right)} - \frac{2}{3}\Delta\lambda_{n+1}\|\mathbf{S}_{n+1}^{trial}\|\right) \tag{154}$$

And, where trial $\mathbb{C}_{dev}^{trial}$ is given by

$$\begin{aligned}\mathbb{C}_{n+1}^{trial} &= \frac{\partial \mathbf{S}_{n+1}^{trial}}{\partial \mathbf{C}_{n+1}} = \bar{\mu}_{n+1}\left(\frac{1}{3}(\mathbf{C}_{n+1})^{-1}\otimes(\mathbf{C}_{n+1})^{-1} + \mathbf{I}_{n+1}\right) \\ &- \frac{1}{3}\,\mu\,J^{-\frac{2}{3}}\,(\mathbf{C}_n^p)^{-1}\otimes(\mathbf{C}_{n+1})^{-1} + (\mathbf{C}_{n+1})^{-1}\otimes(\mathbf{C}_n^p)^{-1}\end{aligned} \tag{155}$$

where $\mathbf{I}_{n+1}$ the operator has the following component form

$$I_{n+1,ijkl} = -\frac{1}{2}(C_{n+1,ik})^{-1}(C_{n+1,jl})^{-1} + (C_{n+1,il})^{-1}(C_{n+1,jk})^{-1} \tag{156}$$

It is important to remark that, the consistent deviatoric tangent modulus is non-symmetrical.

The last point to complete the derivation of the consistent tangent modulus is to calculate the derivatives of the isotropic hardening function used in this work with

respect to the plastic multiplier. The following equations present the derivatives of the *Voce and Simo* model (108).

$$\begin{aligned}\frac{\partial(\sigma_y+\beta)_{n+1}}{\partial \bar{e}^{\,p}_{n+1}} &= H\,(1-w_0(\theta-\theta_0)) \\ &+ \left(K_{inf}\,(1-w_h(\theta-\theta_0)) - K_0\,(1-w_0(\theta-\theta_0))\right)\delta\exp(-\delta\bar{e}^{\,p}_{n+1})\end{aligned} \tag{157}$$

Since, the stress update formula is cast in terms of spatial quantities; it is convenient to transform the material algorithmic tangent moduli (151) into the spatial configuration via a pull-forward operation as follows

$$\bar{\mathbf{c}}_{\,dev,ijkl} = \frac{\partial \mathbf{s}_{n+1}}{\partial \mathbf{1}_{n+1}} = \mathbf{F}_{n+1,iA}\mathbf{F}_{n+1,kC}\mathbf{F}_{n+1,lD}\mathbf{F}_{n+1,jB}\mathbb{C}_{dev,ABCD} \tag{158}$$

$$\frac{\partial \mathbf{s}_{n+1}}{\partial \mathbf{1}_{n+1}} = \delta_1 \frac{\partial \mathbf{s}^{trial}_{n+1}}{\partial \mathbf{1}_{n+1}} + \delta_2 \mathbf{n}_{n+1}\otimes \mathrm{dev}(\mathbf{n}^2_{n+1}) + \delta_3 \mathbf{n}_{n+1}\otimes\mathbf{n}_{n+1} \tag{159}$$

C.2.2 Algorithmic constitutive tensor: IMPL-EX integration scheme

The derivation of the algorithmic tangent moduli for the IMPL-EX stress update algorithm follows a similar procedure to that used for the implicit scheme.

The nonsymmetrical expression for the consistent deviatoric elastoplastic module for the IMPL-EX stress update scheme is given by

$$\bar{\mathbb{C}} = \frac{\partial \mathbf{S}_{n+1}}{\partial \mathbf{C}_{n+1}} = \bar{\delta}_1 \mathbb{C}^{trial}_{dev} + \bar{\delta}_2 \mathbf{N}_{n+1}\otimes \mathrm{Dev}(\mathbf{N}^2_{n+1}) + \bar{\delta}_3 \mathbf{N}_{n+1}\otimes\mathbf{N}_{n+1} \tag{160}$$

where the coefficients $\bar{\delta}_1, \bar{\delta}_2$ and $\bar{\delta}_3$ are defined by the expressions

$$\bar{\delta}_1 = \left(1 - \frac{2\,\bar{\mu}\,\Delta\bar{\lambda}_{n+1}}{\|\mathbf{S}^{trial}_{n+1}\|}\right) \tag{161}$$

$$\bar{\delta}_2 = 2\,\bar{\mu}\Delta\bar{\lambda}_{n+1} \tag{162}$$

$$\bar{\delta}_3 = \left(\frac{2\,\bar{\mu}^2}{\|\mathbf{S}^{trial}_{n+1}\|} + \frac{2}{3}\|\mathbf{S}^{trial}_{n+1}\|\right)\Delta\bar{\lambda}_{n+1} \tag{163}$$

where $\mathbb{C}^{trial}_{dev}$ is given by (155) and

$$\Delta\bar{\lambda}_{n+1} = \Delta\lambda_{n+1}\frac{\Delta t_{n+1}}{\Delta t_n} \tag{164}$$

As was said above, a comparison of the coefficients of equation (161) and equation (152) shows that the algorithmic tangent modulus is simpler in IMPL-EX scheme

that in implicit scheme. Also, equation (161) shows that the tangent moduli of the IMPL-EX scheme is independent of the isotropic hardening function used, by the above reason the task of implementing a new hardening function inside the IMPL-EX scheme is simpler than in the implicit scheme. Since, the stress update formula is cast in terms of spatial quantities; it is convenient to transform the material algorithmic tangent moduli (160) into the spatial configuration via a pull-forward operation as follows

$$\bar{\boldsymbol{c}}_{\,dev,ijkl} = \frac{\partial \bar{\mathbf{s}}_{n+1}}{\partial \mathbf{1}_{n+1}} = \mathbf{F}_{n+1,iA}\mathbf{F}_{n+1,kC}\mathbf{F}_{n+1,lD}\mathbf{F}_{n+1,jB}\,\bar{\mathbb{C}}_{dev,ABCD} \tag{165}$$

$$\frac{\partial \bar{\mathbf{s}}_{n+1}}{\partial \mathbf{1}_{n+1}} = \bar{\delta}_1 \frac{\partial \mathbf{s}^{trial}_{n+1}}{\partial \mathbf{1}_{n+1}} + \bar{\delta}_2 \mathbf{n}_{n+1} \otimes \mathrm{dev}(\mathbf{n}^2_{n+1}) + \bar{\delta}_3 \mathbf{n}_{n+1} \otimes \mathbf{n}_{n+1} \tag{166}$$

C.3 Linearization of the algorithmic dissipation

In the same way, the solution of the mechanical problem using an implicit integration scheme requires the algorithmic elastoplastic tangent moduli, the solution of the thermal problem requires the linearization of the algorithmic dissipation.

The mechanical dissipation (124) that comes from the free energy (109) depends only on the initial flow stress σ_y. This feature, however, is not consistent with the experimental observation on metals which suggest that part of the work hardening possess a dissipative character. In order to accommodate the experimental observations introduced above into the phenomenological thermoplastic constitutive model, an additional dissipation hypothesis concerning the amount of mechanical dissipation must be introduced. In practice, this is accomplished by assuming that the mechanical dissipation is a fraction of the total plastic power.

$$\mathcal{D}_{mech} = \chi \sqrt{\frac{2}{3}}(\sigma_y + \beta)\dot{\lambda} \tag{167}$$

where $\chi \in [0, 1]$ is a constant dissipation factor chosen in the range of $[0.85, 0.95]$.

C.3.1 Linearization of the algorithmic dissipation: implicit integration scheme

An implicit Backward-Euler time discretization of the plastic dissipation is shown in the next equation

$$\mathcal{D}^{n+1}_{mech} = \chi \sqrt{\frac{2}{3}}(\sigma_y + \beta)_{n+1}\frac{\Delta\lambda_{n+1}}{\Delta t} \tag{168}$$

The derivative of the dissipation with respect to the temperature is given by the following expression

$$\frac{\partial \mathcal{D}_{mech}^{n+1}}{\partial \theta} = a \left[\Delta\lambda_{n+1} - \frac{\sqrt{\frac{2}{3}}(\sigma_y + \beta)_{n+1}}{\left(2\,\bar{\mu} + \frac{2}{3}\,b\right)} \right] \tag{169}$$

where the coefficients a and b are given by the expressions

$$a = \frac{\chi}{\Delta t}\sqrt{\frac{2}{3}}\frac{\partial(\sigma_y + \beta)_{n+1}}{\partial \theta} \tag{170}$$

$$b = \frac{\partial(\sigma_y + \beta)_{n+1}}{\partial \Delta\lambda_{n+1}} \tag{171}$$

The terms a and b depends on the yield functions $(\sigma_y + \beta)_{n+1}$. The term b has been calculated in the previous section. Therefore, it is only necessary to calculate the derivative of the yield functions with respect to the temperature field, as is shown in the following lines.

First, the derivative with respect to temperature of the *Simo and Voce* yield function is

$$\begin{aligned} \frac{\partial(\sigma_y + \beta)_{n+1}}{\partial \theta} &= -\sigma_y + K_0\left(1 - \exp(-\delta \bar{e}^{\,p}_{n+1}) w_0\right) \\ &- H + K_{inf}\left(1 - \exp(-\delta \bar{e}^{\,p}_{n+1}) w_0\right) \end{aligned} \tag{172}$$

C.3.2 Linearization of the algorithmic dissipation: IMPL-EX integration scheme

Starting from the extrapolated value of the plastic multiplier, the plastic dissipation at t_{n+1} could be written as

$$\bar{\mathcal{D}}_{mech}^{n+1} = \chi \sqrt{\frac{2}{3}}(\sigma_y + \beta)_{n+1}\frac{\Delta\bar{\lambda}_{n+1}}{\Delta t} \tag{173}$$

As the extrapolated value of the plastic multiplier is held constant during the time increment, the linearization of the IMPL-EX dissipation is given by

$$\frac{\partial \bar{\mathcal{D}}_{mech}^{n+1}}{\partial \theta} = \chi \sqrt{\frac{2}{3}}\frac{\partial(\sigma_y + \beta)_{n+1}}{\partial \theta}\frac{\Delta\bar{\lambda}_{n+1}}{\Delta t} \tag{174}$$

A comparison of equations (175) and (169) shows how simple it is to linearize the plastic dissipation in case of using IMPL-EX.

The derivative of the yield function with respect to the temperature field for each of the model used in this work have been presented in equation (172).

Using the coefficients introduced in equations (170) and (171), the linearization in case of IMPL-EX is simplified as

$$\frac{\partial \bar{\mathcal{D}}_{mech}^{n+1}}{\partial \theta} = a\,[\Delta \bar{\lambda}_{n+1}] \tag{175}$$

D Time integration of the IBVP

The implicit scheme is unconditionally stable; it means that there is no restriction on the time step used in the numerical simulation. In implicit formulations, mechanical problem can be solved in a static o dynamic way. Furthermore, implicit formulations can be used with standard and mixed (displacement/pressure) finite elements. However, implicit schemes needs the solution of a linear system of equations, a certain number of times, within each time step. Usually, the solution of the linear system represents most of the computing time. Furthermore, in the implementation of a new constitutive equation, the implicit time integration has the requirement an algorithmic constitutive tensor. Moreover, in some cases an implicit scheme does not converge, due to the high nonlinearities involved in the problem.

The explicit formulation solves the mechanical problem in a dynamical way. The solution of each time step in an explicit scheme is simple and computationally efficient, provided the use of a lumped mass matrix in the simulation. Explicit schemes do not need the solution of a linear system; this topic is an advantage if the numerical solution is done using parallel computing. Implementation of a new constitutive equation is an easy task; it allows to implement simple or complex constitutive equations without a big effort. Explicit schemes are conditionally stable, it means that the time step used in the simulations should be less or equal than a given critical time step, the critical time step correspond to the time that take to an wave to travel through the small finite element of the mesh. In case of an elastic material, the critical time step depends on the mesh size, elastic modulus, Poisson ratio, density of the material and γ a constant that depends on the finite element used.

$$\Delta t_c = \gamma \frac{\Delta x}{\sqrt{\dfrac{3\,\kappa(1-\nu)}{\rho(1+\rho)}}} = \gamma \frac{\Delta x}{\sqrt{\dfrac{2\,G(1-\nu)}{\rho(1-2\rho)}}} \tag{176}$$

The restriction imposed on the time step by the explicit schemes, allows concluding that for numerical simulation which involves long period of computing time or low speeds, implicit schemes are more favorable in comparison with explicit schemes.

There is no a reference comparison between explicit and implicit time integration schemes in the literature. There are no clear rules to determine in which condition one scheme is better than the other.

In the literature, implicit schemes have been used in [81, 74, 5, 76] and explicit schemes in [50, 61, 27]. Also, there are some mixed schemes in which the hydrostatic part of the balance of momentum is integrated implicitly and the deviatoric part is integrated explicitly. Some examples of mixed time integration schemes are given in the definition of the The Characteristic Based Split [71] and The Finite Calculus [55].

An implicit coupled algorithm is presented next.

D.1 Implicit coupled algorithm (Monolithic scheme)

For simplicity, a partition of the time domain $I := [0, T]$ into N time steps, of the same length Δt is considered. Let us focus on the time step $t_n \to t_{n+1}$, where $\Delta t = t_{n+1} - t_n$. The application of an implicit backward-Euler time integration scheme to the problem (displacements, pressures and temperatures), (16), (14), (15) yields the algorithm described in Box 7 defined by the initial conditions described in (60).

COUPLED SYSTEM OF EQUATIONS

1. Momentum

$$\mathbf{F}_{\mathbf{u},dyn}(\ddot{\mathbf{u}}_{n+1}) = \mathbf{F}_{\mathbf{u},int}\left(\boldsymbol{\sigma}_{n+1}(\mathbf{u}_{n+1}, \mathbf{p}_{n+1}, \theta_{n+1}); \lambda_{n+1}(\mathbf{u}_{n+1}, \theta_{n+1})\right) - \mathbf{F}_{\mathbf{u},ext}(\mathbf{u}_{n+1})$$

2. Incompressibility

$$\left(\mathbf{M}^{\mathbf{p}} + \mathbf{M}^{stab}\right)\mathbf{p}_{n+1} = \mathbf{F}_{p,vol}(J_{n+1}(\mathbf{u}_{n+1}, \theta_{n+1}))$$

where $\mathbf{M}^{\mathbf{p}}$ and $\mathbf{M}^{stab}$ are the mass-type matrices of the linearized pressure and stabilization forces respectively

3. Energy

$$\mathbf{F}_{\theta,dyn}(\ddot{\theta}) = \mathbf{F}_{\theta,int}\left(q(\theta_{n+1}); \mathcal{D}_{int}(\mathbf{u}_{n+1}, \theta_{n+1}); \lambda_{n+1}(\mathbf{u}_{n+1}, \theta_{n+1})\right) - \mathbf{F}_{\theta,ext}$$

---

4. Update nodal variables

$$\begin{aligned} \mathbf{v}_{n+1} &= \mathbf{v}_n + \dot{\mathbf{v}}_{n+1}\Delta t \\ \mathbf{u}_{n+1} &= \mathbf{u}_n + \mathbf{v}_{n+1}\Delta t \\ \mathbf{p}_{n+1} &= \mathbf{p}_n + \Delta p_{n+1} \\ \theta_{n+1} &= \theta_n + \dot{\theta}_{n+1}\Delta t \end{aligned}$$

The definition of the variables that appear in this box are explained in sections 4 and 6.

Box 7: Implicit coupled solution scheme.

The set of equations presented in Box 7 show a simultaneous solution scheme of

the coupled systems of equations where the temperature varies during the mechanical step and the configuration varies during the thermal step. At first glance, the simultaneous solution is the obvious one, but a depth analysis shows that is a computationally intensive procedure [79]. The monolithic scheme is unconditionally stable due to its fully implicit character. The different time scales associated with the thermal and mechanical fields suggested that an effective numerical integration of the coupled problem should take advantage of these different time scales. One of the effective integration schemes is the so-called staggered algorithms, whereby the problem is partitioned into several smaller sub-problems that are solved sequentially (splitting each time step in several pseudo-time steps). Most of the time, this technique is especially attractive from a computational point of view, since the large and no symmetric system that results from a simultaneous solution scheme is replaced by a much smaller, subsystem.

References

[1] F. Armero and J. C. Simo. A new unconditionally stable fractional step method for non-linear coupled thermomechanical problems. *International Journal for Numerical Methods in Engineering*, vol. 35, pp. 737-766, 1992.

[2] P. J. Arrazola. Modelisation numerique de la coupe: etude de sensibilite des parametres d'entree et identification du frottement entre outil-copeau. *Doctoral Thesis*, L'École Centrale de Nantes, l'Université de Nantes, France, 2003.

[3] F. Auricchio, L. Beirão da Veiga, C. Lovadina, and A. Reali. An analysis of some mixed-enhanced finite element for plane linear elasticity. *Computer Methods in Applied Mechanics and Engineering*, vol. 194, pp. 2947-2968, 2005.

[4] M. Bäker. Finite element simulation of high-speed cutting forces. *Journal of Materials Processing Technology*, vol. 176, pp. 117-126, 2006.

[5] M. Bäker, J. Rösler, and C. Siemers. A finite element model of high speed metal cutting with adiabatic shearing. *Computers and Structures*, vol. 80, pp. 495-513, 2002.

[6] P. B. Bochev, C. R. Dohrmann, and M. D. Gunzburger. Stabilization of Low-Order Mixed Finite Elements for the Stokes Equations. *SIAM Journal on Numerical Analysis*, vol. 44, pp. 82-101, 2008.

[7] T. Belytschko, W. K. Liu and B. Moran. Nonlinear Finite Element for Continua and Structures. *England: John Wiley and Sons*, 2000.

[8] J. Bonet and R.W.N. Nonlinear Continuum Mechanics for Finite Element Analysis. *United Kingdom: Cambridge University Press*, 1997.

[9] J. Bonet and A. J. Burton. A simple average nodal pressure tetrahedral element for incompressible and nearly incompressible dynamic explicit applications. *Communications in Numerical Methods in Engineering*, vol. 14, pp. 437-449, 1998.

[10] J. Bonet, H. Marriott, and O. Hassan. Stability and comparison of different linear tetrahedral formulations for nearly incompressible explicit dynamic applications. *International Journal for Numerical Methods in Engineering*, vol. 50, pp. 119-133, 2001.

[11] J. Bonet, H. Marriott, and O. Hassan. An averaged nodal deformation gradient linear tetrahedral element for large strain explicit dynamic applications. *Communications in Numerical Methods in Engineering*, vol. 17, pp. 551-561, 2001.

[12] W. D. Callister and D. G. Rethwisch. Materials Science and Engineering: An Introduction. *New York: Wiley*, 2007.

[13] G. T. Camacho and M. Ortiz. Computational modelling of impact damage in brittle materials. *International Journal of Solids and Structures*, vol. 33, pp. 2899-2938, 1996.

[14] M. Čanađija and J. Brnić. Associative coupled thermoplasticity at finite strain with temperature-dependent material parameters. *International Journal of Plasticity*, vol. 20, pp. 1851-1874, 2004.

[15] J.M. Carbonell. Modeling of Ground Excavation with the Particle Finite Element Method. *PhD thesis, Universitat Politècnica de Catalunya (UPC)*, Barcelona, 2009.

[16] J.M. Carbonell, E. Oñate and B. Suárez. Modeling of Ground Excavation with the Particle Finite-Element Method. *J. Engineering Mechanics*, ASCE, 136:455-463, 2010.

[17] J.M. Carbonell, E. Oñate and B. Suárez. Modeling tunnelling processes and rock cutting tool wear Particle Finite-Element Method. *Computational Mechanics*, vol. 52, pp. 607-629, 2013.

[18] M. Cervera, M. Chiumenti, Q. Valverde, and C. A. d. Saracibar. Mixed linear/linear simplicial elements for incompressible elasticity and plasticity. *Computer Methods in Applied Mechanics and Engineering*, vol. 192, pp. 5249-5263, 2003.

[19] J. S. Chen, C. M. O. L. Roque, C. Pan, and S. T. Button. Analysis of metal forming process based on meshless method. *Journal of Materials Processing Technology*, vol. 80, pp. 642-646, 1998.

[20] M. Chiumenti, Q. Valverde, C. A. d. Saracibar, and M. Cervera. A stabilized formulation for incompressible elasticity using linear displacement and pressure interpolations. *Computer Methods in Applied Mechanics and Engineering*, vol. 191, pp. 5253-5264, 2002.

[21] M. Chiumenti, Q. Valverde, C. A. d. Saracibara, and M. Cervera. A stabilized formulation for incompressible plasticity using linear triangles and tetrahedra. *International Journal of Plasticity*, vol. 20, pp. 14871504, 2003.

[22] A. J. Chorin. A Numerical Method for Solving Incompressible Viscous Flow Problems. *Journal of Computational Physics*, vol. 135, pp. 118-125, 1997.

[23] E. Cueto and F. Chinesta. Meshless methods for the simulation of material forming. *International Journal of Material Forming*, vol. 8, pp. 25-43, 2013.

[24] B.N. Delaunay. Sur la Sphère Vide, A la memoire de Georges Voronoi. *Otdelenie Matematicheskii i Estestvennyka Nauk*, vol. 7, pp. 793-800, 1934.

[25] P. O. De Micheli and K. Mocellin. Explicit F.E. formulation with modified linear tetrahedral elements applied to high speed forming processes. *International Journal of Material Forming*, vol. 1, pp. 1411-1414, 2008.

[26] P. O. De Micheli and K. Mocellin. A new efficient explicit formulation for linear tetrahedral elements non-sensitive to volumetric locking for infinitesimal elasticity and inelasticity. *International Journal for Numerical Methods in Engineering*, vol. 79, pp. 45-68, 2009.

[27] P. O. De Micheli and K. Mocellin. 2D high speed machining simulations using a new explicit formulation with linear triangular elements. *International Journal of Machining and Machinability of Materials*, vol. 9, pp. 266 - 281, 2011.

[28] C. Detournay and E. Dzik. Nodal Mixed Discretization for tetrahedral elements. *presented at the 4th International FLAC Symposium on Numerical Modeling in Geomechanics*, Minneapolis, Paper 07-02, pp. 1-8 2006.

[29] L. M. J. S. Dinis, R. M. Natal Jorge and J. Belinha. Large deformation applications with the radial natural neighbours interpolators. *Computer Modeling in Engineering and Sciences* (CMES), vol. 44, pp. 1, 2009.

[30] C. R. Dohrmann, M. W. Heinstein, J. Jung, S. W. Key, and W. R. Witkowski. Node-based uniform strain elements for three-node triangular and four-node tetrahedral meshes. *International Journal for Numerical Methods in Engineering*, vol. 47, pp. 1549-1568, 2000.

[31] C. R. Dohrmann and P. B. Bochev. A stabilized finite element method for the Stokes problem based on polynomial pressure projections. *International Journal for Numerical Methods in Fluids*, vol. 46, pp. 183201, 2004.

[32] P. Eberhard and T. Gaugele. Simulation of cutting processes using mesh-free Lagrangian particle methods. *Computational Mechanics*, vol. 51(3), pp. 261-278, 2013.

[33] H. Edelsbrunner and E.P. Mucke. Three dimensional alpha shapes. *ACM Transaction on Graphics*, 13:43-72, 1994.

[34] D. Field. Laplacian smoothing and delaunay triangulations. *Communications in Applied Numerical Methods*, 4:709-712, 1988.

[35] M. S. Gadala, M. R. Movahhedya, and J. Wangb. On the mesh motion for ALE modeling of metal forming processes. *Finite Elements in Analysis and Design*, vol. 38, pp. 435459, 2002.

[36] M. S. Gadala. Recent trends in ALE formulation and its applications in solid mechanics. *Computer Methods in AppliedMechanics and Engineering*, vol. 193, pp. 4247-4275, 2004.

[37] F. Greco, D. Umbrello, S. D. Renzo, L. Filice, I. Alfaro, and E. Cueto. Application of the nodal integrated finite element method to cutting: a preliminary comparison with the "traditional" FEM approach. *Advanced Materials Research*, vol. 223, pp. 172-181, 2011.

[38] F. Greco, L. Filice, C. Peco, and M. Arroyo. A stabilized formulation with maximum entropy meshfree approximants for viscoplastic flow simulation in metal forming. *International Journal of Material Forming*, vol. 8(3), pp. 341-353, 2015.

[39] Y. Guo, M. Ortiz, T. Belytschko, and E. A. Repetto. Triangular composite finite elements. *International Journal for Numerical Methods in Engineering*, vol. 47, pp. 287-316, 2000.

[40] Hang Si. TetGen, a Delaunay-Based Quality Tetrahedral Mesh Generator. *ACM Trans. Math. Softw.*, vol. 41(2), Article 11, pp. 1-36, 2015.

[41] A. Ibrahimbegovic and L. Chorfi. Covariant principal axis formulation of associated coupled thermoplasticity at finite strains and its numerical implementation. *International Journal of Solids and Structures*, vol. 39, pp. 499-528, 2002.

[42] S. R. Idelsohn, E. Oñate, and F. D. Pin. The particle finite element method: a powerful tool to solve incompressible flows with free-surfaces and breaking waves. *International Journal for Numerical Methods in Engineering*, vol. 61, pp. 964-989, 2004.

[43] L. Illoul and P. Lorong On some aspects of the CNEM implementation in 3D in order to simulate high speed machining or shearing. *Computer and Structures*, vol. 89, pp. 940958, 2011.

[44] B. Joe. Construction of Three-dimensional Delaunay Triangulations from local transformations. *Computer Aided Geometric Design*, vol. 8, pp. 123-142, 1991.

[45] G. H. Johnson and W. H. Cook. A constitutive model and data for metals subjected to large strains high strain rates and high temperatures. *Proceedings of the 7th symposium on ballistics*, 1983.

[46] K. Komvopoulos and S. A. Erpenbeck. Finite Element Modeling of Orthogonal Metal Cutting. *Journal of Engineering for Industry, Transactions of the ASME*, vol. 113, pp. 253-267, 1991.

[47] J. Limido, C. Espinosa, M. Salan and J. L. Lacome. SPH method applied to high speed cutting modelling. *International Journal of Mechanical Sciences*, vol. 49, pp. 898908, 2007.

[48] J. Lubliner. Plasticity Theory. *New York: Dover Publications*, 2008.

[49] J. Marti and P. Cundall. Mixed discretization procedure for accurate modelling of plastic collapse. *International Journal for Numerical and Analytical Methods in Geomechanics*, vol. 6, pp. 129-139, 1982.

[50] T. D. Marusich and M. Ortiz. Modelling and simulation of high-speed machining. *International Journal for Numerical Methods in Engineering*, vol. 38, pp. 36753694, 1995.

[51] E. A. d. S. Neto, F. M. A. Pires, and D. R. J. Owen. F-bar-based linear triangles and tetrahedra for finite strain analysis of nearly incompressible solids. Part I: formulation and benchmarking. *International Journal for Numerical Methods in Engineering*, vol. 62, pp. 353383, 2005.

[52] J. Oliver, J. C. Cante, R. Weyler, C. González, and J. Hernández. Particle Finite Element Methods in Solid Mechanics Problems. *Computational Methods in Applied Sciences*, vol. 7, pp. 87-103, 2007.

[53] J. Oliver, A. E. Huespe, and J. C. Cante. An implicit/explicit integration scheme to increase computability of non-linear material and contact/friction problems. *Computer Methods in Applied Mechanics and Engineering*, vol. 197, pp. 1865-1889, 2008.

[54] L. Olovsson, L. Nilsson, and K. Simonsson. An ALE formulation for the solution of two-dimensional metal cutting problems. *Computers and Structures*, vol. 72, pp. 497-507, 1999.

[55] E. Oñate, J. Rojek, R. L. Taylor, and O. C. Zienkiewicz. Finite calculus formulation for incompressible solids using linear triangles and tetrahedra. *International Journal for Numerical Methods in Engineering*, vol. 59, pp. 14731500, 2004.

[56] E. Oñate, S.R. Idelsohn, F. Del Pin, and F. Aubry. The particle finite element method. an overview. *International Journal for Numerical Methods in Engineering*, 1(2):964-989, 2004.

[57] E. Oñate, M. A. Celigueta, and S. R. Idelsohn. Modeling bed erosion in free surface flows by the particle finite element method. *Acta Geotechnica*, vol. 1, pp. 237-252, 2006.

[58] E. Oñate, S. R. Idelsohn, M. A. Celigueta, and R. Rossi. Advances in the particle finite element method for the analysis of fluidmultibody interaction and bed erosion in free surface flows. *Computer Methods in Applied Mechanics and Engineering*, vol. 197, pp. 1777-1800, 2008.

[59] E. Oñate and J.M. Carbonel.l Updated lagrangian mixed finite element formulation for quasi and fully incompressible fluids. *Computational Mechanics*, vol. 54, pp. 1583-1596, 2014.

[60] E. Oñate, A. Franci and J.M. Carbonell. A particle finite element method for analysis of industrial forming processes. *Computational Mechanics*, vol. 54, pp. 85-107, 2014.

[61] D. R. J. Owen and M. Vaz Jr. Computational techniques applied to high-speed machining under adiabatic strain localization conditions. *Computer Methods in Applied Mechanics and Engineering*, vol. 171, pp. 445461, 1999.

[62] D. Perić, C. Hochard, M. Dutko, and D. R. J. Owen. Transfer operators for evolving meshes in small strain elasto-plasticity. *Computer Methods in Applied Mechanics and Engineering*, vol. 137, pp. 331344, 1996.

[63] F. M. A. Pires, E. A. d. S. Neto, and D. R. J. Owen. On the finite element prediction of damage growth and fracture initiation in finitely deforming ductile materials. *Computer Methods in Applied Mechanics and Engineering*, vol. 193, pp. 52235256, 2004.

[64] F. M. Andrade Pires, E. A. de Souza Neto, and J. L. de la Cuesta Padilla. An assessment of the average nodal volume formulation for the analysis of nearly incompressible solids under finite strains. *Communications in Numerical Methods in Engineering*, vol. 20, pp. 569-583, 2004.

[65] M. A. Puso, and J. Solberg. A stabilized nodally integrated tetrahedral. *International Journal for Numerical Methods in Engineering*, vol. 67, pp. 841-867, 2006.

[66] W. Quak, A. H. van den Boogaard, and J. Huétink. Meshless methods and forming processes. *International Journal of Material Forming*, vol. 2, pp. 585-588, 2009.

[67] A. Raczy, M. Elmadagli, W. J. Altenhof, and A. T. Alpas. An eulerian finite-element model for determination of deformation state of a copper subjected to orthogonal cutting. *Metalurgical and Materials Transactions A*, vol. 35, pp. 2393-2400, 2004.

[68] V.T. Rajan. Optimality of the Delaunay Triangulation. *Discrete Comput. Geom.*, vol. 12, pp. 189202, 1994.

[69] J. Rambau. On a generalization of Schönhardt's polyhedron. *Combinatorial and computational geometry, New York: MRSI Publications, Cambridge University Press*, pp. 501516, 2005.

[70] J.M. Rodriguez. Numerical modeling of metal cutting processes using the particle finite element method(PFEM). *PhD thesis, Universitat Politècnica de Catalunya (UPC)*, Barcelona, March 2014.

[71] J. Rojek, E. Oñate and R. L. Taylor. CBS-based stabilization in explicit solid dynamics. *International Journal for Numerical Methods in Engineering*, vol. 66, pp. 1547-1568, 2006.

[72] C. A. d. Saracibar, M. Chiumenti, Q. Valverde, and M. Cervera. On the orthogonal subgrid scale pressure stabilization of finite deformation J2 plasticity. *Computer Methods in Applied Mechanics and Engineering*, vol. 195, pp. 12241251, 2006.

[73] E. Schönhardt . Über die zerlegung von dreieckspolyedern in tetraeder. *Math Annalen*, vol. 98, pp. 309-312, 1928.

[74] G. S. Sekhon and J. L. Chenot. Numerical simulation of continuous chip formation during non-steady orthogonal cutting simulation. *Engineering Computations*, vol. 1, pp. 31-48, 1993.

[75] J.R. Shewchuk. A condition guaranteeing the existence of higher-dimensional constrained Delaunay triangulations. *Proceedings of the fourteenth annual symposium on Computational geometry, ACM, Minneapolis, MN, USA*, pp. 76-85, 1998.

[76] A. J. Shih. Finite element analysis of the rake angle effects in orthogonal metal cutting. *International Journal of Mechanical Sciences*, vol. 38, pp. 1-17, 1995.

[77] J. C. Simo. A framework for finite strain elastoplasticity based on maximum plastic dissipation and the multiplicative decomposition: part I. continuum formulation. *Computer Methods in Applied Mechanics and Engineering*, vol. 666, pp. 199-219, 1988.

[78] J. C. Simo. A framework for finite strain elastoplasticity based on maximum plastic dissipation and the multiplicative decomposition. Part II: Computational aspects. *Computer Methods in Applied Mechanics and Engineering*, vol. 68, pp. 1-31, 1988.

[79] J. C. Simo and C. Miehe. Associative coupled thermoplasticity at finite strains: Formulation, numerical analysis and implementation. *Computer Methods in Applied Mechanics and Engineering*, vol. 98, pp. 41-104, 1992.

[80] J. C. Simo and T. J. R. Hughes. Computational Inelasticity. *New York: Springer-Verlag*,1998.

[81] J. S. Strenkowski and J. T. Carroll. A Finite Element Model of Orthogonal Metal Cutting. *Journal of Engineering for Industry, Transactions of the ASME*, vol. 107, pp. 349-354, 1985.

[82] Y. Tadi Beni and M. R. Movahhedy. Consistent arbitrary Lagrangian Eulerian formulation for large deformation thermo-mechanical analysis. *International Journal of Solids and Structures*, Materials & Design, vol. 31, pp. 3690-3702, 2010.

[83] E. Trent and P. Wright. Metal cutting. *Fourth Edition ed*, 2000.

[84] E. Uhlmann, R. Gerstenberger, and J. Kurnert. Cutting simulation with the meshfree finite pointset method. *Procedia CIRP*, vol. 8, pp. 391-396, 2013.

[85] E.Voce. A practical strain hardening function. *United Kingdom: Metallurgia, The British Journal of Metals*, vol. 51, pp. 219-226, 1955.

[86] H. T. Y. Yang, M. Heinstein, and J. M. Shih. Adaptive 2D finite element simulation of metal forming processes. *International Journal for Numerical Methods in Engineering*, vol. 28, pp. 1409-1428, 1989.

[87] O. C. Zienkiewicz and J. Z. Zhu. The superconvergent patch recovery and a posteriori error estimates. Part 1: The recovery technique. *International Journal for Numerical Methods in Engineering*, vol. 33, pp. 1331-1364, 1992.

[88] O. C. Zienkiewicz and J. Z. Zhu. The superconvergent patch recovery and a posteriori error estimates. Part 2: Error estimates and adaptivity. *International Journal for Numerical Methods in Engineering*, vol. 33, pp. 1365-1382, 1992.